Volume 1 • Issue 1
April 2026

THE INSTITUTE
OF INDIAN
FOUNDRYMEN

journal.indianfoundry.org

Sustainable Manufacturing and Foundry Practices

Volume 1 • Issue 1 • April 2026

Sustainable Manufacturing and Foundry Practices is published biannually in April and October by The Institute of Indian Foundrymen.

Sustainable Manufacturing and Foundry Practices is hosted on our web-based online submission and peer review system. Please read the manuscript submission guidelines on the journal website, and then visit https://peerreview.sagepub.com/iif to login and submit your article online. Manuscripts should be prepared in accordance with the 7th edition of the *Publication Manual of the American Psychological Association*.

Annual Subscription: Individual rate (print only) ₹1,720; institutional rate (print only) ₹2,790. For orders from Pakistan, Bangladesh, Sri Lanka and Maldives, SAARC rates apply: individuals $35; institutional rate $50. Prices include postage. Print subscriptions are available for institutions at a discounted rate. For subscriptions, please write to: customerservicejournals@sagepub.in

Change of Address: Four weeks' advance notice must be given when notifying change of address. Please send the old address label to ensure proper identification. Please specify the name of the journal and send change of address notification to customerservicejournals@sagepub.in

Printed and published by Dr. Goutam Sutradhar on behalf of The Institute of Indian Foundrymen, IIF Center, 335, Rajdanga Main Road, Sector C, Kasba, Kolkata, West Bengal, 700107, India. Printed at Sai Printo Pack Pvt Ltd, A 102/4 Phase II, Okhla Industrial Area, New Delhi, Delhi 110020.

Editor: Dr. Goutam Sutradhar

THE INSTITUTE
OF INDIAN
FOUNDRYMEN

About the Journal

Sustainable Manufacturing and Foundry Practices (SMFP) is an international journal established by *The Institute of Indian Foundrymen (IIF)*. Building on IIF's long institutional 76-year legacy, SMFP provides a respected forum for scholarship and practical insight that advances the metal_casting and manufacturing communities worldwide.

The Institute of Indian Foundrymen, founded in 1950 and headquartered in Kolkata, is the national association for India's metal_casting industry. IIF operates through four regional offices (Kolkata, Delhi, Mumbai, and Chennai), four Centers of Excellence (Chennai, Delhi, Kolkata, and Pune), 24 chapters, and one activity center across India. This nationwide network underpins SMFP's close connection to industry needs and its capacity to translate technical knowledge into operational practice.

SMFP occupies a distinctive position at the interface of metallurgy, mechanical engineering, and industrial sustainability. The journal publishes original research, reviews, industrial case studies, and policy analyses that are relevant to both academic inquiry and industrial application. The journal prioritizes work that guides the adoption of technology, enhances process performance, and fosters sustainable industrial transitions.

SMFP serves a broad readership that includes academic researchers, practicing engineers, industry leaders, policymakers, and technology developers. The journal aims to bring about knowledge exchange and technology transfer by presenting work that is both scientifically robust and practically useful, thereby supporting improvements in productivity, resource efficiency, and environmental performance.

THE INSTITUTE
OF INDIAN
FOUNDRYMEN

Aims and Scope

The *Sustainable Manufacturing and Foundry Practices (SMFP)* is a premier **Open Access** journal, published **bi-annually**, which is an initiative of *The Institute of Indian Foundrymen (IIF)*. The journal aims to provide a comprehensive platform for the publication of a broad range of high-quality research and review papers in those fields of scientific and engineering research appertaining to the development, application, and optimization of **foundry technologies** and **sustainable manufacturing practices**. Papers describing original work in these areas are submitted to rigorous **double-anonymized peer refereeing** prior to acceptance for publication. This strict process ensures objective evaluation based solely on scientific merit and contribution to the field.

While many journals focus separately on materials science or production engineering, *SMFP* fills a critical gap by bridging the divide between fundamental solidification science and applied sustainable manufacturing. We aim to connect the lab to the ladle, offering a unique venue for research that addresses the dual challenges of digital transformation and environmental stewardship.

We encourage high-quality original research and timely review submissions that offer insights into the processing, characterization, modelling, prediction, and optimization of foundry systems. Our goal is to make a significant contribution to the field by publishing work that not only advances theoretical understanding but also demonstrates economic viability and pathways toward net-zero, zero-defect manufacturing.

The scope of the *Sustainable Manufacturing and Foundry Practices* encompasses, but is not restricted to, the following core areas:

- Advanced casting processes and solidification science
- Cyber-physical production systems (CPPS) and IIoT
- Digital Twins and smart process control
- Industrial AI, machine learning, and prognostics
- Decarbonization and energy-efficient melting strategies
- Circular economy, material reclamation, and closed-loop flows
- Life cycle engineering (LCE) and sustainability metrics
- Hybrid and additive manufacturing workflows
- Sustainable binders, coatings, and refractories
- Computational modeling (CFD/FEA) and simulation
- Zero-defect manufacturing and quality engineering

The Journal publishes **Original Research Articles, Comprehensive Review Articles, Industry Case Studies** (emphasizing industrial application and economic viability), T**echnical Communications**, and papers focused on **Policy and Standardization**. The target audience includes global academic researchers, R&D professionals, technical managers, and policy stakeholders in the metal casting and advanced manufacturing sectors, with a commitment to advancing the state of knowledge worldwide.

Editorial Board

Editor-in-Chief

Goutam Sutradhar, *National Institute of Technology Jamshedpur, NIT Jamshedpur, India*

Managing Editor

Abhishek Sen, *The Institute of Indian Foundrymen, Kolkata, India*

Associate Editors

B. Ravi, *NITK Surathkal, India*

Nagahanumaaiah, *CMTI, Bengaluru, India*

Debdas Roy, *Department of Materials and Metallurgical Engineering National Institute of Advanced Manufacturing Technology (Formerly NIFFT) Hatia, Ranchi, India*

Indradev Samajdar, *Metallurgical Engineering and Materials Science, IIT Bombay, India*

Karabi Das Pramanik, *Department of Metallurgical and Materials Engineering, IIT Kharagpur, India*

Sudip Kumar Samanta, *CSIR-CMERI, Durgapur, India*

Nilrudra Mandal, *CSIR-CMERI, Durgapur, India*

Titas Nandi, *Department of Mechanical Engineering, Jadavpur University, West Bengal, Kolkata, India*

S. Senthil Kumaran, *Department of Mechanical Engineering, ANNA University, Chennai, India*

D. Benny Karunakar, *Department of Mechanical and Industrial Engineering, IIT Roorkee, India*

Assistant Editors

Ajay Kumar, *Department of Mechanical Engineering, Indian Institute of Technology (IIT) Tirupati, India*

Himanshu Khandelwal, *Department of Foundry Technology, National Institute of Advanced Manufacturing Technology, Ranchi, India*

Advisory Board

Volume 1 Issue 1 April 2026

Sustainable Manufacturing and Foundry Practices

Contents

Visit https://journal.indianfoundry.org/

Editorial

Sustainable Manufacturing and
Foundry Practices
1(1) 7–8, 2026
© The Author(s) 2026
DOI: 10.1177/IIF.261420913
Journal.indianfoundry.org
THE INSTITUTE
OF INDIAN
FOUNDRYMEN

From the Desk of the Editor in Chief

It gives me an immense pleasure to welcome you to *"Sustainable Manufacturing and Foundry Practices"* (SMFP). This journal has been conceived at a time when manufacturing and foundry industries across the world are rethinking their approaches to grow efficiently with a prime goal towards sustainable development. The increasing demand for sustainable processes, cleaner technologies, and responsible use of resources calls for thoughtful research and meaningful knowledge exchange. This journal seeks to serve as a trusted platform for this purpose.

Manufacturing and foundry practices have always played a vital role in industrial and economic development. Today, their future depends on how effectively sustainability is integrated into design, production, and management. The journal aims to bring together researchers, academicians, and industry professionals who are working towards improving manufacturing systems while reducing environmental impact. By encouraging high quality research and practical insights, we hope to support the transition towards more responsible and resilient industrial practices.

The Indian Institute of Foundrymen (IIF) having a glorious legacy of attachment to the metal casting industry adds significant value to this initiative. The Institute has a long and respected history of supporting foundry education, research, and industry engagement. Publishing services are facilitated by Spectrum Journals (Powered by Sage). It also reflects our commitment to fostering closer interaction between academia and industry.

The journal is designed to connect *"the lab to ladle"* covers a wide range of topics related to sustainable manufacturing and foundry practices. These include energy efficient processes, green foundry technologies, circular economy approaches, advanced materials and composites, waste reduction strategies, and the application of digital manufacturing technologies to improve sustainability in production systems. We aim to publish work that is not only theoretical but also economically viable and practically applicable. We encourage contributions that are original, well structured, and address current challenges faced by the manufacturing and foundry sectors from solidification science to the development of sustainable binders and coatings, integration of Cyber physical systems, Industrial AI /IIOT and human centric innovation.

Maintaining high academic standards is central to the journal's mission. All submissions are carefully reviewed to ensure originality, technical quality, and ethical integrity. The editorial team is committed to a fair and transparent **double anonymised peer review process** that ensures every article – whether original research paper or an industry case studies. SMFP is proud to launch as a premier Open Access journal with Zero Publication Charges for authors.

I warmly invite researchers and practitioners from across the globe to contribute to this journal and to engage with the knowledge it shares. Through collective effort and shared commitment, this journal aims to contribute meaningfully to the advancement of sustainable manufacturing and foundry practices, and to support a more responsible industrial future.

Dr Goutam Sutradhar
Editor in Chief
Sustainable Manufacturing and Foundry Practices
E-mail: editor_in_chief@indianfoundry.org

Article

Feasibility and Sustainable Utilization of Cupola Slag for Eco-Friendly Industrial Waste Management

Sustainable Manufacturing and
Foundry Practices
1(1) 9–27, 2026
© The Author(s) 2026
DOI: 10.1177/IIF.261420257
Journal.indianfoundry.org
THE INSTITUTE OF INDIAN FOUNDRYMEN

Rakesh Sikder[1,2], Debasis Sau[3], Soumyabrata Chakravarty[4], Partha Haldar[5], Saroj Mandal[3], Titas Nandi[1] and Goutam Sutradhar[6]

Abstract

Cast iron remains one of the most widely used alloys in modern industrial applications, with cupola furnaces being the most economical and commonly employed melting units. The melting of pig iron, scrap metal and flux in a cupola furnace generates a significant quantity of oxidized by-product known as cupola slag, which is presently classified as industrial waste and predominantly disposed of in landfills, posing environmental concerns. This study aims to systematically evaluate the potential of cupola slag as a sustainable construction material by comparing its characteristics with established industrial by-products, such as fly ash and ground granulated blast furnace slag. The physical and chemical properties of cupola slag were analysed using standard testing methods, with its chemical composition determined by X-ray fluorescence spectroscopy. The R3 reactivity test classified cupola slag as a pozzolanic, low-reactivity material. Leachability tests confirmed that the slag is non-toxic and complies with regulatory limits for hazardous elements. A life cycle assessment revealed that landfill disposal of cupola slag results in a global warming potential of approximately 32.12 kg CO_2-equivalent per kilogram of slag. Furthermore, a comparative performance

---

[1]Department of Mechanical Engineering, Jadavpur University, Kolkata, India
[2]Department of Mechanical Engineering, Elitte College of Engineering, Kolkata, India
[3]Department of Civil Engineering, Jadavpur University, Kolkata, India
[4]Department of Mechanical Engineering, Brainware University, Kolkata, India
[5]Department of Mechanical Engineering, Government College of Engineering and Ceramic Technology, Kolkata, India
[6]National Institute of Technology, Jamshedpur, India

Corresponding author
Partha Haldar, Department of Mechanical Engineering, Government College of Engineering and Ceramic Technology, Kolkata, West Bengal 700010, India.
E-mail: partha.jumech@gmail.com

evaluation was conducted to assess its suitability as a partial or full replacement for cement and natural aggregates in concrete. The results demonstrate that cupola slag exhibits promising potential as a sustainable supplementary material in cement concrete, offering significant environmental benefits by reducing landfill disposal, conserving natural resources and promoting eco-friendly construction practices.

Keywords

Cupola slag, concrete, physical properties, Mechanical properties, XRF, XRD

Introduction

Rapid industrial expansion to meet the demands of an expanding population is a major contributing factor to the growing amount of industrial waste produced and discarded each year (Cheah et al., 2021; Sikder et al., 2025). In 2020, global casting production was estimated at roughly 105 million metric tons, based on data from the Statista Research Department (n.d.). With 51.95 million metric tonnes, China led the world in production. India came in second with 11.31 million metric tonnes, or roughly 11% of the total. As shown in Figure 1(a), global casting production from 2018 to 2020 reveals yearly variations in overall output among the major producing countries. This exceeded the production of the United States,

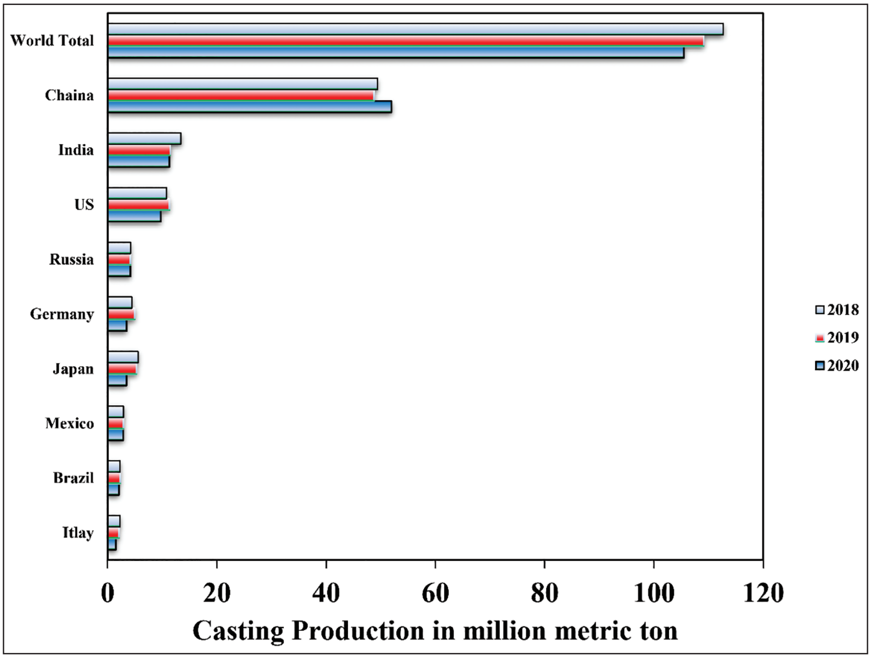

Figure 1(a). Global production of casting, 2018–2020.

Source: Statista Research Department (n.d.).

which occupied the second position in 2019. As a result, the steel and iron industries produce large amounts of sludge and slag on a daily basis, either as waste or by-products, including cupola slag, ground granulated blast furnace slag (GGBS), and fly ash (Gencel et al., 2021). The cupola is employed for melting pig iron and fluxes to produce grey cast iron, with a secondary product known as cupola slag. Cast iron manufacturing results in the generation of roughly 40–80 kg of slag per metric ton (Aderibigbe & Ojobo, 1982; Sikder, Chakravarty, Haldar, Nandi, Mandal, et al., 2023). The chemical makeup of cupola slag is greatly influenced by the melting process in a cupola as well as the composition of the input materials. Scientists have found that cupola slag typically includes substances such as Al_2O_3, MnO, SiO_2, MgO, TiO_2, CaO, Fe_2O_3, Cr_2O_3 and Na_2O (Balaraman & Ligoria, 2015; Chakravarty, Sikder, et al., 2023a; 2023b; 2024). During the cooling process, slag viscosity and crystallization behaviour are directly influenced by its chemical composition. As a result, the porosity, dimensions and characteristics of the solidified slag vary with composition, thereby affecting its suitability for different applications (Baricová, 2018). The melting process in 21,532 of the 47,145 cast iron plants worldwide is carried out in cupola furnaces. With an annual cast iron production of around 11 million tonnes out of a global total of 47.795 million tonnes, India plays a significant role in the industry. Nearly 5,000 cupola furnaces across the country generate 7–8 million tonnes of cast iron per year, leading to the production of approximately 0.4–0.5 million tonnes of cupola slag annually (Chakravarty, Haldar, et al., 2023). Preservation of natural resources and addressing the impact of global warming are paramount concerns in today’s environmental discourse. The disposal of waste in landfills can lead to the pollution of air, water and soil, resulting in adverse effects on the growth of vegetation, plant life and human health. In recent years, the recycling of industrial slag has become a central focus for various academics, driven by the shared goal of safeguarding the global environment (Pribulová et al., 2019). Currently, a growing number of researchers are actively exploring alternative and practical applications for cupola slag within the construction industry. This versatile material has the potential to replace coarse and fine aggregates, as well as cement, in the production of concrete, opening up new avenues for sustainable construction practices. In its composition, concrete typically consists of a blend of cement, fine aggregates and coarse aggregates (Alabi & Afolayan, n.d.). It is important to note that the production of cement results in a significant release of CO_2 and other greenhouse gases, which have adverse environmental implications. For instance, the production of 1 ton of Ordinary Portland Cement (OPC) clinker leads to the emission of 1 ton of CO_2 and other harmful greenhouse gases that pose environmental hazards. In the composition of concrete, natural aggregates typically account for 60%–70% of the total volume of materials. The role of fine aggregate within concrete is of paramount importance, constituting around 30% of the total concrete mix volume (Waseem & Singh, 2016). The workability and cohesiveness of concrete are strongly influenced by the effectiveness of fine aggregates in occupying the voids between larger aggregate particles and the cement paste. Historically, natural river sand has been the principal source of fine aggregates for concrete (Waseem & Singh, 2016). However, in an effort to conserve natural resources and

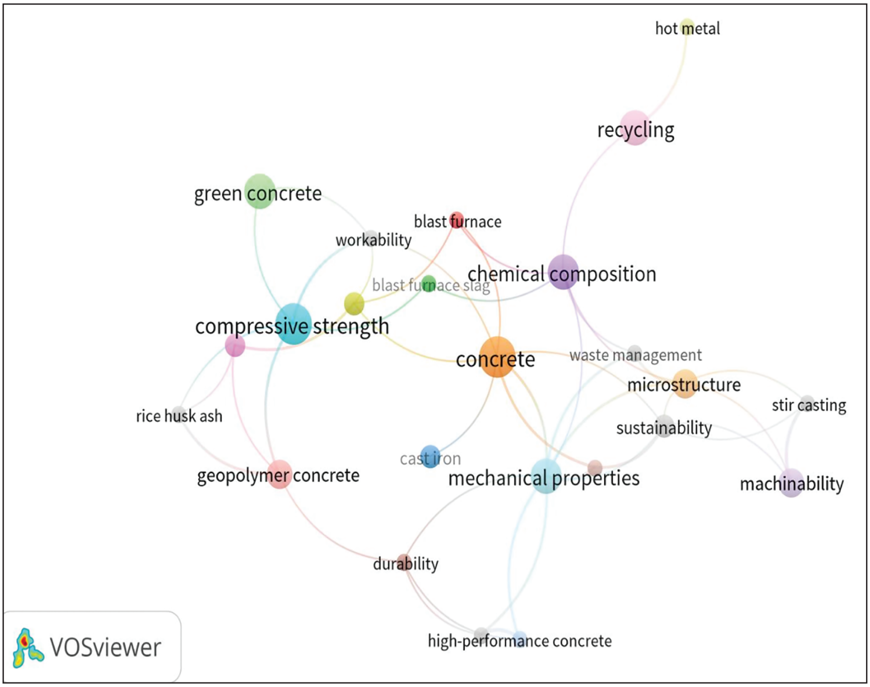

Figure 1(b). Co-occurrence Network of Keywords.

mitigate environmental pollution and waste generation associated with landfills, various types of industrial waste, including blast furnace slag, copper slag and steel slag, have been explored as alternative substitutes for natural river sand in concrete production. The construction sector stands as the foremost consumer of materials on a global scale, with an ever-increasing demand for building materials. Currently, worldwide consumption exceeds an impressive 60 gigatons per year (Thomas et al., 2021). In response to the growing demand for construction materials and the increasing emphasis on environmental sustainability, the effective use of slags in concrete has gained significant importance. Consequently, extensive research has been undertaken to evaluate the potential of slags as viable construction materials. The primary focus of this study is to explore the viability of integrating cupola slag as an alternative to conventional building materials within the construction sector. Figure 1(b) displays the publication years of the literature containing the specified keywords.

This research aims to reduce the environmental impact of industrial waste disposal while conserving natural aggregate and cement resources. It also seeks to advance sustainable construction practices. However, prior studies show minimal research on the use of cupola slag as a replacement for cement, fine aggregates and coarse aggregates, and only a few studies have examined the leachability and life cycle assessment (LCA) of virgin cupola furnace slag. Thus, the viability of using cupola slag in concrete in place of cement, fine aggregate and coarse aggregate is investigated in this work. It also carries out a thorough laboratory analysis to evaluate the leachability characteristics of cupola slag in addition to its physical and chemical attributes. Moreover, an LCA methodology is utilized to assess the ecological consequences of cupola slag disposal in landfills. Through a case study, the study also looks at how partial substitution affects the performance of concrete made with cupola slag, offering useful insights.

Materials and methodology

Cupola slag collected from Binay Udyog Pvt Ltd., Howrah, West Bengal, India, was processed by ball milling to prepare it for application as a substitute for cement as well as natural coarse and fine aggregates. Fresh river sand, with particles passing through a 4.75 mm sieve, has been chosen as the fine aggregate for this study as standard. This selection underscores the relatively small size of the sand particles, which makes them well-suited for use in concrete production. To ensure the fine aggregates conform to the specifications outlined in IS 383: 2016 (Indian Standards Institution, 1970), a sieve analysis has been conducted. Crushed rock serves as the primary natural coarse aggregate in this study as standard, while crushed cupola slag (Figure 2(a)) is utilized as a partial replacement for coarse aggregate. Both of these aggregates have been carefully selected, with their

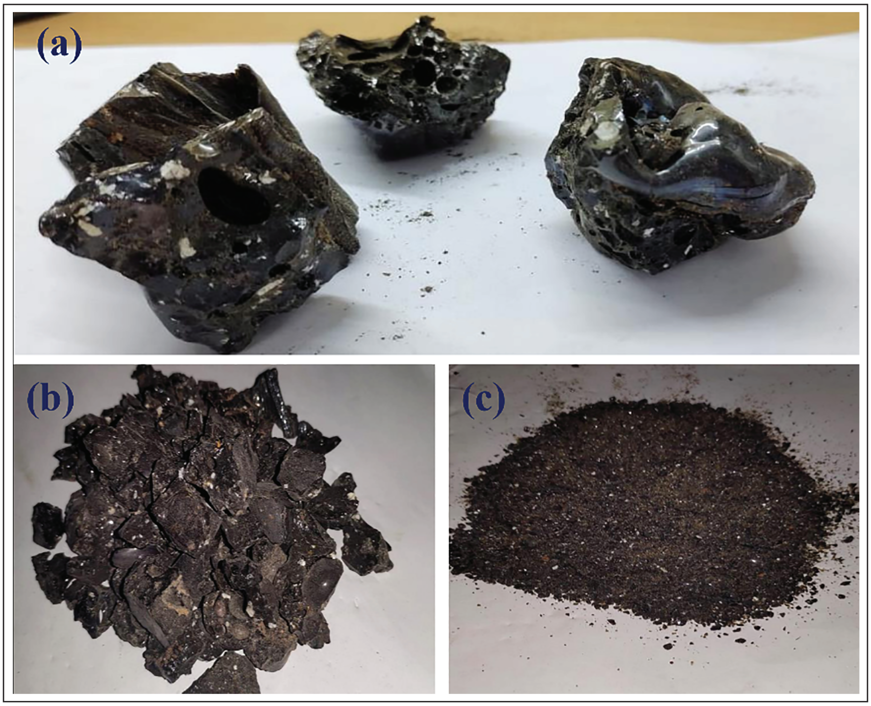

Figure 2. (a) untreated cupola slag, (b) cupola slag prepared as coarse aggregate and (c) cupola slag prepared as fine aggregate.

particle sizes falling within the range of 20 mm and 4.75 mm. The physical properties of aggregate and cement were tested in the lab for suitability analysis.

Compliance of the coarse aggregates with IS 383: 2016 (Indian Standards Institution, 1970) was assessed through sieve analysis, along with an evaluation of the physical properties of cupola slag fine and coarse aggregates. Figures 2(b) and 2(c) are assessed through measurements of specific gravity, bulk density and water absorption. Impact, crushing and abrasion tests were conducted to assess the mechanical properties of cupola slag and natural coarse aggregates, as specified in IS 383: 2016 (Indian Standards Institution, 1970). Using an X-ray diffraction (XRD) instrument made by Rigaku Corporation and an X-ray fluorescence (XRF) analyser (a Rigaku ED-XRF Model-NEX DE Analyser), the chemical composition and mineral phases found in cupola slag were identified. Heavy metal levels in cupola slag were assessed using a modified Toxicity Characteristic Leaching Procedure. For testing, cupola slag was ground into a powder and sieved through a 10-mm mesh screen.

Shaking of each flask was carried out at 60 rpm for 18 hours under ambient temperature conditions (~25°C). The prepared solution contained 5.7 mL of 98% glacial acetic acid, 64.3 mL of 1 N NaOH solution and 100 g of crushed cupola slag. A variety of analytical techniques, including GC-MS for organic compounds and ICP-MS for heavy metals, were used to examine the resultant leachate samples for contaminants or parameters of interest.

The environmental impacts of cupola slag disposal were evaluated using Ecoinvent (2022) data and OpenLCA 2.1, following the ISO 14040 (LCA Consequential, 2015) framework, which includes goal and scope definition, inventory analysis, impact assessment and interpretation. Disposal-related environmental impacts were assessed using XRF-derived material composition as input data, with disposed slag defined as the environmental output and transportation effects excluded. The ReCiPe Midpoint (H) 2016 method was employed, and a case study on partial replacement of natural aggregates in concrete was also examined.

Results and Discussions

Physical Properties

Assessment of cupola slag as a concrete aggregate was carried out by examining its physical characteristics, such as colour, appearance, structure, particle size, water absorption, bulk density and specific gravity. Generally, the slag exhibits a vitrified and dense structure, with colour variations from green to brown (Pribulová et al., 2018). Additionally, the size and colour of cupola slag can differ due to variations in operating procedures and the quality of metal processed in the furnaces. Research studies (Agarwal et al., 1991; Baricová, 2018; Pribulová et al., 2018; Pribulová et al., 2019) have identified two distinct types of cupola slag based on their cooling methods. Cupola slag occurs in two forms: a slowly cooled, grey crystalline slag that is crushed into gravel-sized particles for use as aggregate, and a granulated slag produced by rapid water quenching, which forms a glassy material suitable for cementitious applications. Based on particle size, cupola slag can be classified as cementitious material (≈75 μm), fine aggregate (<4.75 mm) and coarse aggregate (10–20 mm).

Table 1. Physical Characteristics of Cupola Slag as Coarse Aggregate and Natural Coarse Aggregate.

Physical Properties	Cupola Slag Coarse Aggregates	Natural Coarse Aggregates
Zone	1	1
Bulk density (kg/m^3)	1,400	1,600
Water absorption	1.8%	0.6%
Specific gravity	2.81	2.79

Table 2. Physical Characteristics of Cupola Slag as Fine Aggregates and Natural Fine Aggregates.

Physical Properties	Cupola Slag Fine Aggregates	Natural Fine Aggregates
Zone	1	1
Water absorption	1.65%	2.4%
Specific gravity	2.14	2.65

Table 1 shows that cupola slag used as coarse aggregate has lower bulk density and higher water absorption than natural coarse aggregates due to its porous structure, while differences in specific gravity influence concrete density and durability. Overall, the physical properties indicate that cupola slag can partially replace natural coarse aggregates and closely match natural fine aggregates, making it a potential substitute in concrete applications. Table 2 presents the physical properties of natural fine aggregates and cupola slag as fine aggregates. The gradation of aggregates, including the cupola slag, as established by sieve analysis, is shown in Figure 3. Based on particle classification, 5% of the cupola slag particles were gravel-sized, while 95% were sand-sized.

Workability

The flow table test (Figure 4) results indicate that the flowability of cupola slag-based cement ranges from 120% to 160%. The glassy structure and spherical particles of finely ground cupola slag promote improved flow by minimizing internal friction. Consequently, composite materials exhibit enhanced flowability as the proportion of natural aggregates replaced by fine and coarse cupola slag increases. This implies that the cohesiveness of the mixture is impacted by the addition of cupola slag. Furthermore, the cupola slag-based coarse aggregate is well-graded gravel, and the cupola slag-based fine aggregate is well-graded sand, according to sieve analysis (Figure 3).

Mechanical properties

Mechanical tests on fine and coarse aggregates, including crushing, abrasion and impact tests, indicate that due to its porous nature and distinct grading, cupola slag performs comparably to natural fine aggregates and can serve as a suitable

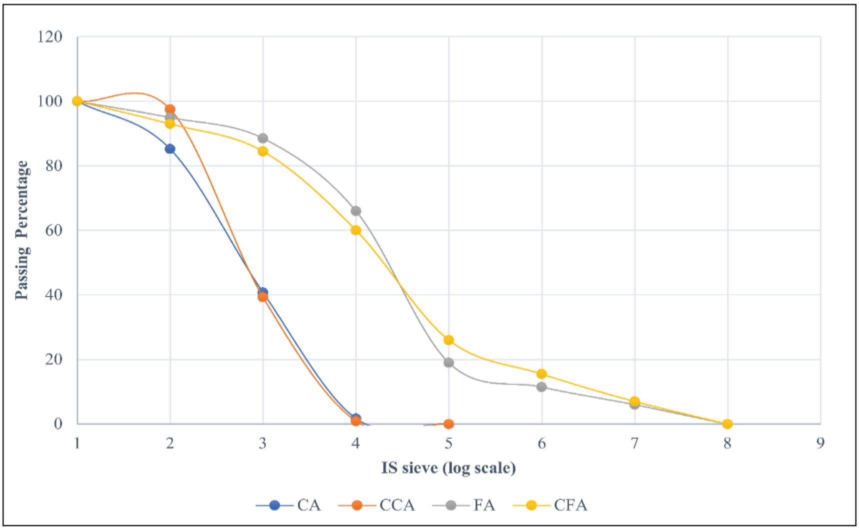

Figure 3. Particle Size Distribution Curve Of Different Natural And Cupola Slag-Based Fine And Coarse Aggregate.

Notes: CA – Coarse aggregate, FA – Fine aggregate, CCA – Cupola slag-based coarse aggregate, CFA – Cupola slag-based fine aggregate.

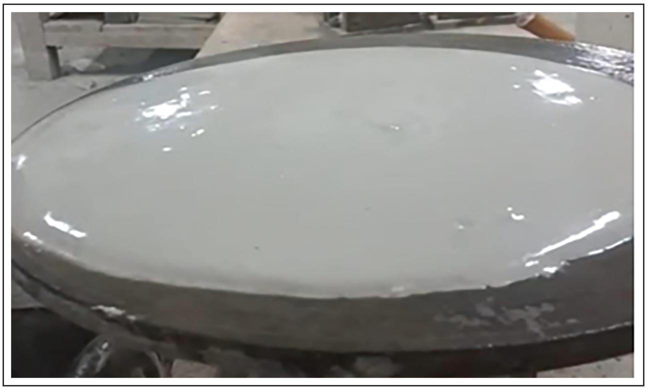

Figure 4. Flow Table Test of Cupola Slag-Based Cement.

substitute in high-quality concrete. However, the significantly lower crushing strength of cupola slag compared to natural coarse aggregates (Figure 5) makes it unsuitable as a replacement for coarse aggregates in high-grade concrete.

Concrete compressive strength increases with lower water–cement ratios and higher replacement levels of cupola slag as fine aggregate, primarily due to improvement of the interfacial transition zone and pore-filling effects that create a denser microstructure. These results indicate that replacing conventional materials with cupola slag up to an optimum percentage does not compromise the strength requirements specified in design standards. Although cupola slag

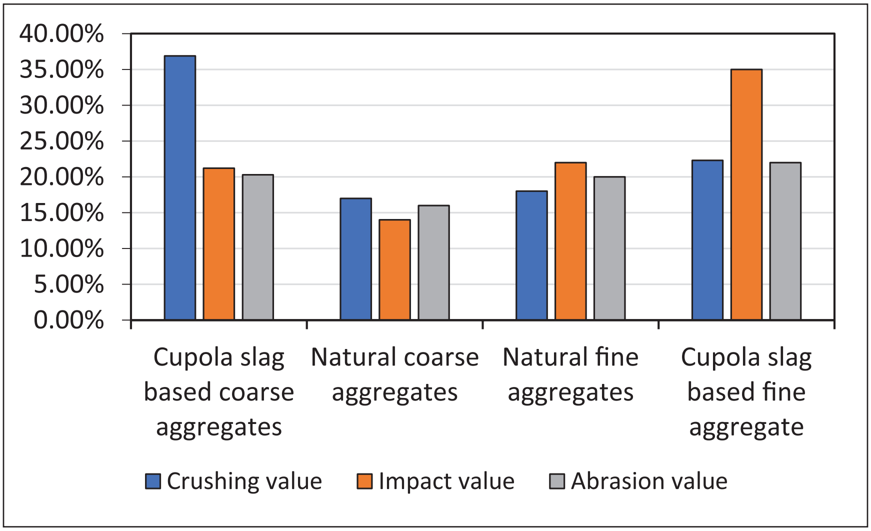

Figure 5. Mechanical Properties of Cupola Slag and Natural Coarse Aggregates.

possesses relatively good mechanical properties, its inherently porous structure increases concrete porosity when used as coarse aggregate, thereby diminishing compressive strength (Sikder et al., 2024; Waseem et al., 2021).

The addition of cupola slag as a partial cement replacement has a substantial effect on concrete compressive strength, with strength enhancement occurring at replacement levels below the optimal 50%. Previous investigations (Aderibigbe & Ojobo, 1982; Alabi & Afolayan, n.d.; Kubiliute et al., 2018; Thomas et al., 2021) have demonstrated improved compressive strength values for concrete containing cupola slag as a cementitious material within the 5%–30% replacement range. Additionally, research (Rodríguez-Mendoza et al., 2012) has examined the cementitious behaviour of cupola slag (ranging from 10% to 80%) in combination with calcium sulphate cement and Portland cement as activation materials. The maximum replacement level attained was 80%, comprising 15% anhydrite calcium sulphate cement and 5% Portland cement. Furthermore, a patented method (Sosa et al., 2021) was developed for producing slag cement using cupola slag. The highest recorded compressive strength of 7,000 psi was achieved with an optimized cupola slag content of 35%, which was characterized by a Blaine's surface area of 6,000–6,500 cm^2/g.

Research by Sosa et al. (2020) on concrete incorporating electric arc furnace slag and cupola slag supports these findings. They observed that cupola slag particles integrate well with the cement paste and natural aggregate forming compounds in the shape of parallel hexagonal plates, which are consistent with hydrated calcium aluminosilicates. These findings are consistent with the report (Sosa et al., 2020) that the addition of cupola slag increased compressive strength. By incorporating cupola slag, the concrete's porosity is reduced, increasing its density and compressive strength.

Hydraulicity

One of the main characteristics of slag that greatly affects its binding behaviour is its hydraulicity or pozzolanicity. The setting characteristics of both cementitious and supplemental cementitious materials are determined by these properties because they undergo chemical reactions when mixed with water and continue to react even after hardening under extended water curing (Aristizábal et al., 2014). Earlier, a study (Pribulová, 2018) illustrated the granulated cupola slag's hydraulic qualities and its possible application as an activator in the manufacturing of cement. The pozzolanic reaction index at 28 days was 25% for raw cupola slag and 30% for calcined cupola slag when mixed with Portland cement, according to Aderibigbe and Ojobo's investigation into calcination to increase its reactivity. Nonetheless, it was discovered that a minimum pozzolanic activity index of 85% was necessary for slags, suggesting that cupola slag is comparatively less reactive. Furthermore, the study verified that cupola slag reacts more slowly than slags from blast furnaces. Thomas et al. (2021) conducted a pozzolanicity test in compliance with EN 196-5, a standard that measures hydroxyl ion and calcium oxide concentrations. With CaO levels of 6.4 and OH^- values of 58, the results showed that cupola slag satisfies the pozzolanicity requirements. To further examine the hydraulic and pozzolanic properties of cupola slag, another researcher (Meshram et al., 2022) carried out an altered R3 test. The calcium hydroxide consumption levels of the two cupola slag samples examined in this study were 42 g/100 g and 43 g/100 g of supplementary cementitious material (SCM), respectively, with corresponding heat release values of 219 J/g SCM and 207 J/g SCM. Cupola slag is categorized as a 'pozzolanic, less reactive' material based on these findings. It does, however, also fall on the line between the 'pozzolanic, less reactive' and 'latent hydraulic, less reactive' categories because of its crystalline nature. Numerous studies show that concrete containing cupola slag achieves greater strength in later curing stages as opposed to early-age curing because of its pozzolanic properties (Raja & Kumar, 2023).

Leachability Test

Leaching is the process by which heavy and toxic materials dissolve and are released when industrial waste and water come into contact. Extreme conditions, such as extremely acidic or alkaline environments, make this process worse. There are serious health and environmental hazards when the resultant leachate contaminates soil and water sources. Cupola furnace slag contains concentrations of several heavy and toxic metals, such as nickel (0.02 mg/L), chromium (0.05 mg/L), mercury (0.001 mg/L), copper (0.02 mg/L), lead (0.01 mg/L), zinc (0.02 mg/L) and cadmium (0.002 mg/L), according to the leachability test results. The contaminants present in the slag and their corresponding concentrations are revealed by these results. Cupola furnace slag is classified as a non-hazardous and non-toxic material because the data show that it contains very low levels of heavy and toxic substances. To create green concrete, cupola furnace slag can be utilized as an aggregate, providing a sustainable building option that is less harmful to the environment (Rodrigues et al., 2017; Thomas et al., 2021).

Table 3. Chemical Components of Cupola Slag, GGBS.

Component (wt. %)	Cupola Slag	GGBS	Fly Aash	OPC
SiO_2	53.1	34.62	50.2	21.6
Al_2O_3	11.1	11.82	22	5.9
Fe_2O_3	16.1	2.73	18.3	3.3
CaO	10.7	37.37	4.2	61.9
MgO	3.33	9.43	9.9	4.3
SO_3	0.9	1.42	0.6	1.23
K_2O	1.05	0.5	2.9	-

Source: Ainie Mat Dom et al. (2022), and for fly ash, Bhatt et al. (2019).

Chemical composition analysis

The chemical composition of concrete materials strongly influences their mechanical performance and durability. Table 3 compares the chemical composition (wt.%) of cupola slag with commonly used construction materials—GGBS, OPC, and fly ash—based on XRF analysis of the cupola slag.

SiO_2 was found to be the predominant constituent of the cupola slag, consistent with the XRD analysis. Cupola slag's composition also contained a number of additional metal oxides, all of which were within permissible bounds. It is worth noting that the chemical composition of the cupola slag, as reported in prior academic studies by Mistry and Varia (2020) and Sikder, Chakravarty, Haldar, Nandi, and Sutradhar (2023) and Sikder (2024), aligns with the XRF results presented here.

LCA Test

As a byproduct of making steel, cupola slag can have several negative effects on the environment when it is released into the environment. Its global warming potential, which was determined to be 31.12 kg CO_2-equivalent per 1 kg of slag disposed of in landfills, was the focus of the LCA analysis. Other impact indicator results were presented in Figure 6. Basically, in Figure 6, terrestrial ecotoxicity is higher, followed by global warming potential, human non-carcinogenic toxicity, fossil fuel formation and human carcinogenic toxicity. However, the environmental impact of concrete and mortar is greatly diminished when cupola slag is used in place of cement, fine aggregate or coarse aggregate.

Through encouraging the use of environmentally friendly materials, this sustainable approach helps lessen the effects of global warming, ecotoxicity and human health and may have advantages for the construction sector.

XRD analysis

XRD analysis of cupola furnace slag (Figure 7) reveals characteristic peaks corresponding to calcium silicate, iron silicate, albite and lanthanum strontium

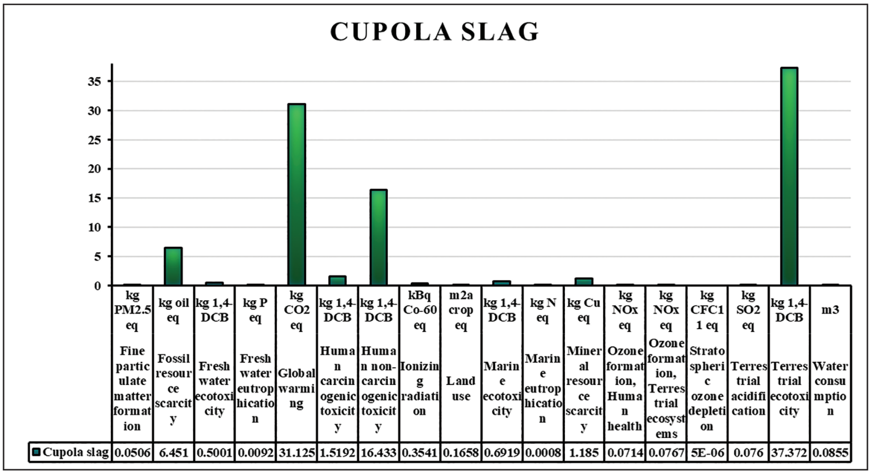

Figure 6. LCIA for Cupola Slag by ReCiPe Midpoint (H) for Base Scenarios.

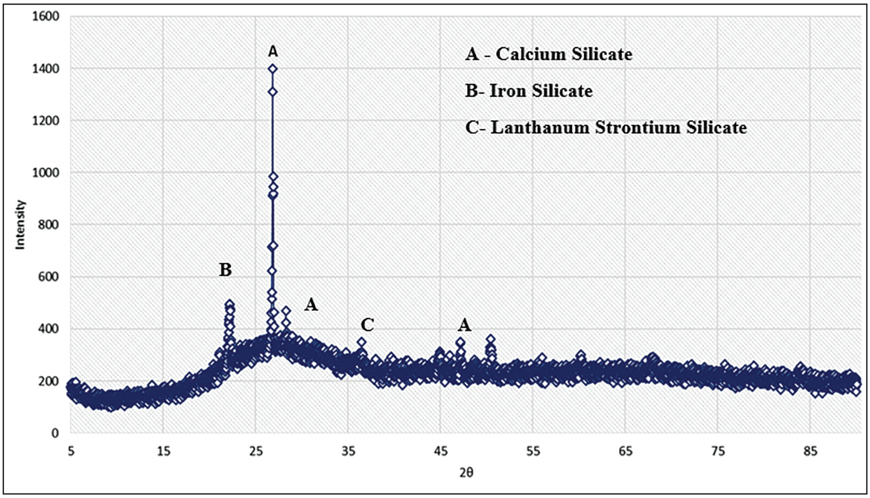

Figure 7. XRD Analysis.

silicate, with triclinic, orthorhombic and hexagonal lattice structures. The presence of these iron- and silica-rich phases indicates the potential formation of strength-enhancing compounds when cupola slag is incorporated into composite materials. In a detailed mineralogical investigation conducted by Pribulová et al. (2019), cupola slag samples obtained from the foundry industry in Ghana were found to exhibit complex crystalline phases. The identified mineral constituents included calcium iron oxide ($CaFe_4O_7$), kanoite [(Mn, Mg) $_2(Si_2O_6)$], kyanite (Al_2SiO_5), maghemite (γ-Fe_2O_3) and quartz (SiO_2). Notably, the analysis did not detect the presence of free elemental iron, magnesium oxide (MgO) or calcium

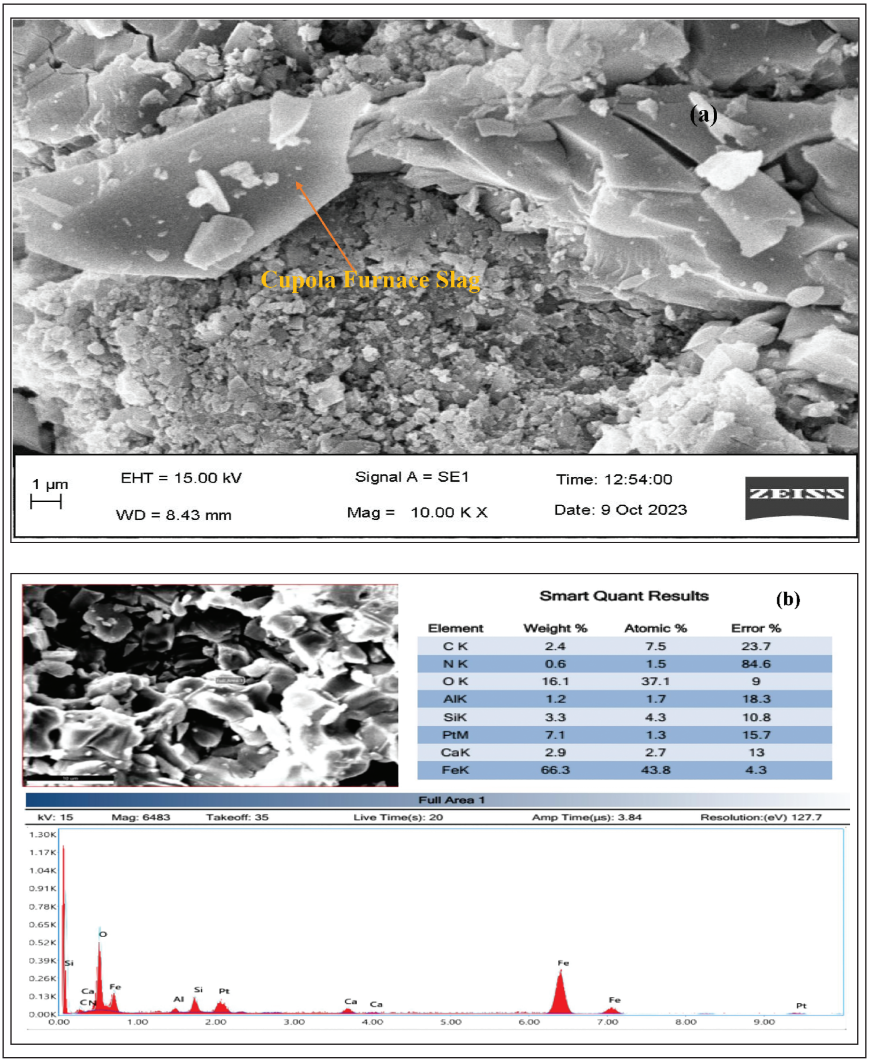

Smart Quant Results

Element	Weight %	Atomic %	Error %
C K	2.4	7.5	23.7
N K	0.6	1.5	84.6
O K	16.1	37.1	9
AlK	1.2	1.7	18.3
SiK	3.3	4.3	10.8
PtM	7.1	1.3	15.7
CaK	2.9	2.7	13
FeK	66.3	43.8	4.3

Figure 8. The result of (a) SEM and (b) EDX Analysis.

oxide (CaO), which are often expected in similar slags. The findings highlight the high variability in the chemical and mineralogical composition of cupola slags across different geographical and industrial sources. Despite these variations, a consistent trend across most studies is the predominance of crystalline phases in cupola slag. This crystalline structure significantly impacts the material's performance in secondary applications. Specifically, the high degree of crystallinity is associated with a reduced pozzolanic reactivity, limiting the slag's effectiveness as a supplementary cementitious material when compared to other slags such as basic oxygen furnace or electric arc furnace slag.

SEM and EDX Analysis

As presented in Figure 8, SEM and EDX were used to analyse the surface morphology and elemental composition of cupola slag. According to SEM, EDX and XRD results, granulated cupola slag has a homogeneous, amorphous structure with uniformly distributed oxides, while air-cooled cupola slag has a primarily crystalline structure dominated by iron oxide grains. Slow cooling and the uneven distribution of iron oxides and other mineral constituents are responsible for cupola slag's crystalline nature. This results in the formation of distinct crystal phases and, as a result, lower pozzolanic reactivity when compared to other steel slags. Baricová et al. (2010) corroborated these findings by providing detailed morphological observations, which matched the patterns identified in other studies.

Case Study

This study assesses mineral wool cupola dust as a partial cement replacement and found that up to 15 wt. % of the milled micro-filler does not compromise 28-day strength. While unwashed dust caused 90-day strength loss due to chloride-induced Friedel's salt, washing significantly reduced chloride content, resulting in improved long-term performance and a more stable cementitious matrix (Kubiliute et al., 2018).

The study showed that although raw cupola slag has a pozzolanic-like chemical composition, its inherent reactivity is low, but calcination at 700°C for 5 hours significantly improves its pozzolanic activity. With only a 13.5% strength reduction at 20% cement replacement, calcined cupola slag emerges as a viable and cost-effective partial substitute in regions where slag is readily available and cement is expensive (Aderibigbe & Ojobo, 1982).

Cupola slag improves the tensile strength, decreases water penetration, increases abrasion resistance at higher slag content, increases compressive strength by up to 30% when it is used as a replacement for fine aggregates at a lower water cement ratio (Waseem et al., 2021).

This study shows that while replacing coarse aggregate with cupola furnace slag (0%–50%) reduces density, increases porosity and lowers mechanical strength, slag-induced mineral formations allow up to 40% replacement to meet target strength, with SEM/EDS confirming weak gel development and overall concrete cost decreasing by 4.678% per m^3 (Sikder et al., 2024).

General Discussion

Reusing cupola slag significantly lowers carbon emissions, industrial waste and dependence on natural resources, while landfill disposal has a global warming potential of approximately 31.12 kg CO_2-equivalent per kilogramme. Therefore, using cupola slag as a partial substitute for cement and natural aggregates in concrete offers significant environmental and sustainability benefits. According to studies, cupola slag can reduce water penetration and improve durability, increase abrasion resistance at replacement levels by up to 40%, improve compressive and split tensile strength by up to 30%, and reduce concrete production costs by about 4.68% per cubic metre while still meeting strength requirements (Sikder et al., 2024). For the construction industry, cupola slag is a practical and sustainable substitute due to its cost savings and environmental benefits. Cupola slag adds new mineral compound phases (calcite, muscovite, albite and quartz) that support the development of strength, according to microstructural analysis. However, because it is crystalline, the aggregate-cement bond is weakened, increasing porosity and marginally decreasing mechanical durability at higher replacement levels. Despite this, cupola slag is a promising material for green building and circular economy projects because optimized substitution levels provide a balance between strength, durability and sustainability. Therefore, using cupola slag in concrete as a partial substitute for cement and natural aggregates not only lessens the environmental impact and carbon emissions but also increases cost effectiveness and encourages the use of sustainable materials in the building industry.

The primary drawbacks of using slag are its inherent chemical composition diversity, which is dependent on furnace charge, operating temperature and foundry processes. This causes inconsistent material performance and makes standardization difficult. Additionally, gaining full environmental certification necessitates more thorough long-term assessments, such as ecotoxicity evaluation, groundwater interaction studies and field-scale monitoring, even when preliminary leachability results may show conformity with primary regulations. Together, these elements restrict the immediate widespread use of slag-based products and emphasize the need for more comprehensive frameworks for certification and evaluation.

Conclusions

Cupola slag's qualities as an additional cementitious material and its potential applications as fine and coarse aggregates have been carefully examined and experimentally examined. Studies have also looked into its LCA, leachability and hydraulic characteristics. The main conclusions drawn from these studies are outlined below:

- An analysis of the physical properties indicates that cupola slag, a dense vitrified by-product available as granulated or slow-cooled forms, exhibits adequate strength, predominantly sand-sized particles (≈95%), slightly lower specific gravity and higher water absorption than natural aggregates, demonstrating its suitability as a sustainable substitute for natural aggregates in concrete.
- Cupola slag shows high flowability (120%–160%) and good grading, making it suitable as a fine aggregate in high-strength concrete, where it improves compressive strength at lower water–cement ratios, but it is not recommended as a coarse aggregate due to its porous nature.
- Partial replacement of cement with cupola slag (up to 50%), particularly at 35%, achieving a compressive strength of 7,000 psi, reduces porosity, increases density and strength and offers significant environmental and

economic benefits by lowering natural aggregate demand and supporting sustainable construction.
- Cupola slag exhibits hydraulic and pozzolanic behaviour but with low early reactivity, achieving only 25%–30% pozzolanic activity at 28 days and reacting more slowly than blast furnace slag. However, it meets basic reactivity criteria and contributes to improved strength at later curing stages.
- Leachability tests show that cupola slag releases only trace amounts of heavy metals, all within permissible limits, classifying it as non-toxic and non-hazardous and supporting its safe use as a sustainable material in green concrete.
- Cupola slag is mostly made up of silicon dioxide (SiO_2), with trace amounts of other metal oxides, such as GGBS, OPC and fly ash.
- Using cupola slag in concrete reduces its carbon footprint compared to landfill disposal, promoting sustainable construction.
- Cupola slag has been found to contain compounds such as calcium silicate and iron silicate that increase material strength, making it a possible addition for concrete.
- Cupola slag has less pozzolanic reactivity than other steel slags because of its crystalline structure, which is dominated by iron oxide.
- Cupola slag into circular economy frameworks and achieving national and international environmental certifications will further enhance its commercial acceptance and promote its widespread adoption in eco-friendly construction materials.
- Reducing slag generation in the cupola melting process can be achieved by using cleaner charge materials, optimizing coke and flux proportions, and maintaining proper furnace temperature and blast control to limit oxidation. Regular maintenance, improved scrap segregation and better process monitoring further help minimize unwanted slag formation and support more efficient, sustainable operations.

Cupola slag is a practical and environmentally friendly substitute for fine aggregate in the manufacturing of concrete. Future research should maximize strength and durability by optimizing the replacement levels of cupola slag. Activation techniques should be investigated to increase its reactivity and evaluate resistance to environmental factors. Examining its application in 3D printing, geopolymers and structural applications may increase its potential. To guarantee both cost-effectiveness and safety, environmental and economic evaluations are crucial. Cupola slag's status as a sustainable building alternative will be established through comparative research with other cementitious materials.

Acknowledgements

The authors acknowledge Mr Rajib Ghosh, Dy Engineer–Technical Service, Ramco Cement Ltd., India, for providing cement required for the research work.

Declaration of Conflicting Interests

The authors declared no potential conflicts of interest with respect to the research, authorship and/or publication of this article.

Funding

The authors disclosed receipt of the following financial support for the research, authorship, and/or publication of this article: This work was supported by the Department of Science & Technology and Biotechnology, Government of West Bengal, under the sanctioned project 'Reuse of Cupola Slag – An Attempt to Sustainable Manufacturing' (Memo No. 114 (Sanc.)/STBT–11012(16)/16/2021–ST SEC dated 27.08.2023), awarded to Jadavpur University.

ORCIDs

Rakesh Sikder https://orcid.org/0000-0001-8246-3719
Debasis Sau https://orcid.org/0000-0002-2508-6184
Soumyabrata Chakravarty https://orcid.org/0000-0002-3579-9161
Partha Haldar https://orcid.org/0000-0002-0659-5100
Titas Nandi https://orcid.org/0000-0002-4438-9973
Goutam Sutradhar https://orcid.org/0000-0002-4642-5341

References

Aderibigbe, D. A., & Ojobo, A. E. (1982). Properties of cupola slag as a pozzolana and its effects on partial replacement of cement in a mortar. *Conservation & Recycling*, *5*(4), 203–208. https://doi.org/10.1016/0361-3658(82)90048-0

Agarwal, G., Hong K. S., Fletcher, M. R., & Speyer, R. F. (1991). Crystallization behavior of cupola slag glass-ceramics. *Journal of Non-Crystalline Solids*, *130*(2), 187–197. https://doi.org/10.1016/0022-3093(91)90454-E

Ainie Mat Dom, A., Jamaluddin, N., Azlina Abdul Hamid, N., & Siok Hoon, C. (2022). A review: GGBS as a cement replacement in concrete. *IOP Conference Series: Earth and Environmental Science*, *1022*(1), 012044. https://doi.org/10.1088/1755-1315/1022/1/012044

Alabi, S. A., & Afolayan, J. O. (n.d.). Investigation on the potentials of cupola furnace slag in concrete. *International Journal of Integrated Engineering*, *5*(2).

Aristizábal, R. E., Pérez, P. A., Katz, S., & Bauer M. E. (2014). Studies of a quenched cupola. *International Journal of Metalcasting*, *8*(3), 13–22. https://doi.org/10.1007/BF03355586

Balaraman, R., & Ligoria, S. A. (2015). Utilization of cupola slag in concrete as fine and coarse aggregate. *International Journal of Civil Engineering and Technology*, *6*(8), 6–14.

Baricová, D. (2018). Recycling possibilities of the slag from cupola furnace. *International Multidisciplinary Scientific GeoConference*, *18*(4.2), 137–144. https://doi.org/10.5593/sgem2018/4.2/S18.018

Baricová, D., Pribulová, A., & Demeter, P. (2010). Comparison of possibilities the blast furnace and cupola slag utilization by concrete production. *Archives of Foundry Engineering*, *10*(2), 15–18.

Bhatt, A., Priyadarshini, S., Mohanakrishnan, A. A., Abri, A., Sattler, M., & Techapaphawit, S. (2019). Physical, chemical, and geotechnical properties of coal fly ash: A global review. *Case Studies in Construction Materials*, *11*, e00263. https://doi.org/10.1016/j.cscm.2019.e00263

Chakravarty, S., Haldar, P., Nandi, T., & Sutradhar, G. (2023). Cupola slag reutilization for sustainable waste management: Review and economic analysis. *International Journal of Environmental Science and Technology*, *20*(1), 1169–1184. https://doi.org/10.1007/s13762-021-03574-x

Chakravarty, S., Sikder, R., Haldar, P., Nandi, T., & Sutradhar, G. (2023a). Experimental investigation on feasibility of industrial waste to resource conversion for cupola slag. *Results in Engineering*, *17*, 100962. https://doi.org/10.1016/j.rineng.2023.100962

Chakravarty, S., Sikder, R., Haldar, P., Nandi, T., & Sutradhar, G. (2023b). Machinability of cupola slag incorporated LM11 matrix composites in turning: Surface roughness and MRR analysis. *Materials Today Communications*, *37*, 107414. https://doi.org/10.1016/j.mtcomm.2023.107414

Chakravarty, S., Sikder, R., Haldar, P., Nandi, T., & Sutradhar, G. (2024). Exploring energy aspects and tool wear on dry turning of cupola slag-reinforced aluminium metal matrix composites. *Journal of the Brazilian Society of Mechanical Sciences and Engineering*, *46*(2), 59. https://doi.org/10.1007/s40430-023-04651-7

Cheah, C. B., Tan, L. E., & Ramli, M. (2021). Recent advances in slag-based binder and chemical activators derived from industrial by-products – A review. *Construction and Building Materials*, *272*, 121657. https://doi.org/10.1016/j.conbuildmat.2020.121657

Gencel, O., Karadag, O., Oren, O. H., & Bilir, T. (2021). Steel slag and its applications in cement and concrete technology: A review. *Construction and Building Materials*, *283*, 122783. https://doi.org/10.1016/j.conbuildmat.2021.122783

Indian Standards Institution. (1970). *IS 383: Specification for coarse and fine aggregates from natural sources for concrete*. New Delhi, India.

Kubiliute, R., Kaminskas, R., & Kazlauskaite, A. (2018). Mineral wool production waste as an additive for Portland cement. *Cement and Concrete Composites*, *88*, 130–138. https://doi.org/10.1016/j.cemconcomp.2018.02.003

LCA Consequential. (2015). *The ISO 14040 standards for consequential LCA*.

Meshram, S. S., Raut, S. P., & Madurwar, M. V. (2022). Use of industrial waste burnt residue to develop sustainable brick. *Materials Today: Proceedings*, *60*, 732–737. https://doi.org/10.1016/j.matpr.2022.02.336

Mistry, V. K., & Varia, D. J. (2020). Green concrete by replacing coarse aggregate with cupola slag for environmental protection. *In Renewable Energy and Climate Change: Proceedings of REC 2019* (pp. 223–237).

Pribulova, A. (2018). Hydraulicity of metallurgical slags. *18th International Multidisciplinary Scientific GeoConference SGEM 2018*, *18*(4.2), 89–96. https://doi.org/10.5593/sgem2018/4.2/S18.012

Pribulová, A., Baricová, D., Futas, P., Pokusova, M., & Eperjesi, S. (2019). Cupola furnace slag: Its origin, properties and utilization. *International Journal of Metalcasting*, *13*, 627–640.

Pribulová, A., Futáš, P., Petrík, J., Pokusová, M., Brzeziński, M., & Jakubski, J. (2018). Comparison of cupola furnace and blast furnace slags with respect to possibilities of their utilization. *Archives of Metallurgy and Materials*, 1865–1873. https://doi.org/10.24425/amm.2018.125117

Raja, R., & Kumar, S. (2023). Cupola slag as a green concrete-making material and its performance characteristics – A review. *Renewable and Sustainable Energy Reviews*, *185*, 113573. https://doi.org/10.1016/j.rser.2023.113573

Rodrigues, P., Silvestre, J., Flores-Colen, I., Viegas, C., de Brito, J., Kurad, R., & Demertzi, M. (2017). Methodology for the assessment of the ecotoxicological potential of construction materials. *Materials*, *10*(6), 649. https://doi.org/10.3390/ma10060649

Rodríguez-Mendoza, Y. E., Fuentes, A. F., & Escalante-García, J. I. (2012). Cementitious blends of Portland cement with calcium sulphate, fly ash and cupola slag. *MRS Proceedings, 1488*, imrc12-1488-07b–013. https://doi.org/10.1557/opl.2012.1541

Sikder, R., Chakravarty, S., Haldar, P., Nandi, T., & Sutradhar, G. (2023). Scope for cupola slag reuse in construction: A sustainable green solution. *International Journal* *of Environmental Science and Technology*, *20*(6), 7019–7028. https://doi.org/10.1007/s13762-022-04257-x

Sikder, R., Chakravarty, S., Haldar, P., Nandi, T., Mandal, S., & Sutradhar, G. (2023). Cupola slag as partial replacement of coarse aggregate in concrete. *Materials Today: Proceedings*. https://doi.org/10.1016/j.matpr.2023.03.190

Sikder, R., Chakravarty, S., Sau, D., Haldar, P., Mandal, S., Nandi, T., & Sutradhar, G. (2024). Study of durability and mechanical properties for utilization of cupola slag as a coarse aggregate in M20 grade green concrete. *Journal of Building Engineering*, *87*, 109101. https://doi.org/10.1016/j.jobe.2024.109101

Sikder, R., Chakravarty, S., Sau, D., Haldar, P., Mandal, S., Nandi, T., & Sutradhar, G. (2025). Utilization of cupola slag as fine aggregates in green concrete. In *International Conference on Mechanical Engineering* (pp. 131–143). Springer Nature. https://doi.org/10.1007/978-981-97-6667-3_11

Sosa, I., Tamayo, P., Sainz-Aja, J. A., Cimentada, A., Polanco, J. A., Setién, J., & Thomas, C. (2021). Viability of cupola slag as an alternative eco-binder and filler in concrete and mortars. *Applied Sciences*, *11*(4), 1957. https://doi.org/10.3390/app11041957

Sosa, I., Thomas, C., Polanco, J. A., Setién, J., & Tamayo, P. (2020). High performance self-compacting concrete with electric arc furnace slag aggregate and cupola slag powder. *Applied Sciences*, *10*(3), 773. https://doi.org/10.3390/app10030773

Statista Research Department. (n.d.). *Casting production worldwide by country 2020*. Statista.

Thomas, C., Sainz-Aja, J., Sosa, I., Setién, J., Polanco, J. A., & Cimentada, A. (2021). Physical-mechanical properties of cupola slag cement paste. *Applied Sciences*, *11*(15), 7029.

Waseem, S. A., & Singh, B. (2016). Shear transfer strength of normal and high-strength recycled aggregate concrete – An experimental investigation. *Construction and Building Materials*, *125*, 29–40. https://doi.org/10.1016/j.conbuildmat.2016.08.022

Waseem, S. A., Thakur, N., Islam, S. U., Kumar, M., & Saini, J. S. (2021). Cupola slag as partial replacement of fine aggregate in concrete – An experimental study. *Journal of Building Engineering*, *44*, 103343. https://doi.org/10.1016/j.jobe.2021.103343

Article

Sustainable Manufacturing and
Foundry Practices
1(1) 28–51, 2026
© The Author(s) 2026
DOI: 10.1177/IIF.261437191
Journal.indianfoundry.org
THE INSTITUTE
OF INDIAN
FOUNDRYMEN

Energy Consumption and Surface Roughness Minimization by Optimization of Cutting Parameters for Al Alloy SiC Composites

Rajesh Kumar Bhushan[1]

Abstract

The present work investigates the influence of variations in cutting speed, feed, depth of cut and nose radius on both machining energy intake and the resulting surface texture throughout turning of AA7075 reinforced with 15 wt% SiC particles, sized 10–20 μm. The response surface methodology (RSM) technique was employed to accomplish the minimum surface roughness and energy utilization. 3D surface curves of RSM showed cutting speed to be the key reason in minimizing surface roughness and energy intake, and subsequently depth of the cut, feed and radius of nose. Multi-response optimization values of cutting factors through turning of AA7075/15 wt% SiC to minimize surface roughness and energy utilization have been found by desirability analysis. The results show that a 16.06% reduction in surface roughness can be achieved by merely increasing electrical energy consumption by 4.88%. Turning to the cutting parameter value obtained by multi-response optimization results in the reduction of energy consumption and surface roughness. Naturally available materials were utilized for fabrication. The novelty of this work is that scarce literature has been reported on the determination of the optimal process parameters for turning AA7075/15 wt% SiC (10–20 μm) composites at which minimum electrical energy will be consumed, and minimum surface roughness will be obtained.

Keywords

Desirability approach, energy consumption, surface roughness, AA7075, multi-objective optimization, Response Surface Methodology

---

[1]National Institute of Technology Manipur, Imphal, Manipur, India

Corresponding author:
Rajesh Kumar Bhushan, National Institute of Technology Manipur, Imphal, Manipur, India.
E-mail: rajeshnit25@gmail.com

Introduction

Manufacturing of good quality at minimum fabrication cost is a need of the industry. Machining environments, for example, nose radius, feed, speed of cutting and depth of cut in turning manoeuvre, must be optimized to minimize the total manufacturing cost of each component. The cost of computer numerically controlled (CNC) machines is higher than that of lathe machines. Hence, CNC machines must be operated efficiently to recover extra costs. Machining at elevated cutting speeds tends to accelerate tool wear and can lead to increased vibration along with higher electrical energy requirements. However, fast speed cutting is preferred because chip removal is fast. Therefore, there was little heat transfer to component. Hence, the possibility of thermal distortion was reduced. The novelty of this work is that exploration is needed to govern the consequences of factors on energy consumption and component surface roughness at high-speed dry turning. However, the challenge is if high speed is used for fast material removal or to minimize surface roughness, machine energy consumption will increase. Hence, some technique is required for optimization. Design of experiments (DOE) is the design of the experiment so that a minimum number of experiments are needed to draw correct conclusions (Montgomery, 1997).

Literature Review

Thomas and Chanderasekaran (1997) utilized a complete factorial strategy to discover the role of machining factors on the resulting surface coarseness during the carbon steel turning. Yang and Tarng (1998) used the Taguchi method to obtain optimal parameters for machining. Choudhury and EI-Baradie (1997) used response surface methodology (RSM) to find surface roughness while machining extra-stiff steel. Thiele and Melkote (1999) utilized a factorial strategy to find the influence of component stiffness and apparatus profile on surface coarseness and machining powers. Antony (2000) carried out multi-response optimization utilizing Taguchi's loss function and principal component analysis. Lee et al. (2000) used a polynomial network to create a machining database. Lin et al. (2001) utilized an addictive network to build a prediction model for surface roughness and cutting forces. Muthukrishnan et al. (2008) on A356/SiC/10p composite conducted turning experiments using polycrystalline diamond (PCD 1500) inserts. Surface coarseness, explicit energy used and apparatus wear were found. Results showed that fast cutting rates result in comparatively easy elimination of stiff SiC particles. El-Gallab and Sklad (1998) examined the consequence of several cutting parameters on surface characteristics and the magnitude of the sub-surface damage caused by machining. PCD conducted cutting experiments. SEM pictures of machined surfaces show the existence of grooves and holes. Surface roughness quantities display that surface coarseness progresses through a rise in the rate of feed and cutting rate, but somewhat worsens with a rise in depth of cut. PCD tools and chemical vapour deposition (CVD) diamond-layered tools were used for turning A356/SiC/20p composite. Cutting forces, flank wear and surface coarseness were measured. Tool life arcs exhibited that feed does contrary to cutting speed. CVD diamond tools showed short tool life. PCD inserts are necessary for turning A356/SiC/20p composite to achieve extended tool life and minimum surface roughness (Davim, 2002). Kılıckap et al. (2005) identified 5% SiC-p Al MMC for the study of tool wear and surface roughness. K10 carbide inserts, both unlayered and TiN-layered, were tested under various machining conditions, including cutting rates of 150, 100 and 50 m/min, rates of feed of 0.3, 0.2 and 0.1 mm/rev, and penetration of cuts of 1.5, 1 and 0.5 mm. Under dry machining conditions, tool wear was predominantly governed by cutting rate, aggregately noticeable as the speed increased. The TiN-coated tool exhibited poorer wear than the uncoated insert. Surface roughness was mainly prejudiced by the speed of cutting and feed speed, where the upper speed of cutting combined with a lower rate of feed resulted in an improved surface finish.

The powder metallurgy route was used to fabricate AA2124/SiC-p composites. Surface coarseness was selected as the dependent variable. PCD tools were used for turning. Response surface-based D-optimal design of 29 trials was considered. An ANN method was used to forecast surface coarseness. Results exhibited that the size of SiC particles affects surface roughness significantly (Basheer et al., 2008). Nose radius reinforces the tool tip by thinning of the chip, where it reaches the tool point, and by scattering the chip over a bigger nose radius. Surface roughness is also reduced since tool inscriptions are not so deep as those made by a sharp tool (Lindberg, 1990). Ozben et al. (2008) prepared MMCs by mixing 15, 10 and 5 wt% of SiC-p in $AlSi_7Mg_2$. The mechanical properties of the composite were evaluated with respect to varying reinforcement ratios. The impact of the rate of cutting, the rate of the feed and the penetration of the cut on tool degradation and surface coarseness was also assessed. A higher proportion of SiC particles resulted in increased tool degradation, and surface coarseness was found to be predominantly influenced by the rate of feed and speed of cutting.

The above literature has shown that little work has been done with the objective of reducing energy usage and improving surface finish while machining AA7075/15 wt% SiC (10–20 μm) composites. This exploration effort is needed to know the outcome of the rate of the feed, speed of cutting, radius of nose, depth of cut on energy consumption and surface coarseness. A face-centred central composite design was utilized to design the testing. Multi-response optimization of turning factors was done by a desirable methodology to reduce the energy used and surface roughness. The novelty of this examination is that, so far, very little exploration has been reported about the finding of optimal process parameters for turning the AA7075/15 wt% SiC (10–20 μm) composites at which minimum electrical energy will be consumed, and surface roughness will also be minimum.

Investigational Work

Fabrication of AA7075/15 wt % SiC (10–20 μm) Composite

Stir casting set-up shown in Figure 1 was used to fabricate the composite.

Figure 1. Stir Casting Set-up.

Element	Wt%	At%
OK	01.66	02.90
MgK	03.19	03.68
AlK	82.82	85.87
SiK	03.85	03.84
FeK	00.74	00.37
CuK	02.22	00.98
ZnK	05.52	02.36
Matrix	Correction	ZAF

EDAX Analysis of AA7075/15 wt% SiC (10–20 μm) Composite

Figure 2 and the corresponding table show that wt% of Al is 82.82%. Wt% of Zn is 5.52%. Si wt% is 3.85%.

Machining

Tool Holders and Inserts

Particulars of inserts and tool holders used for turning on the CNC machine are tabulated in Table 1.

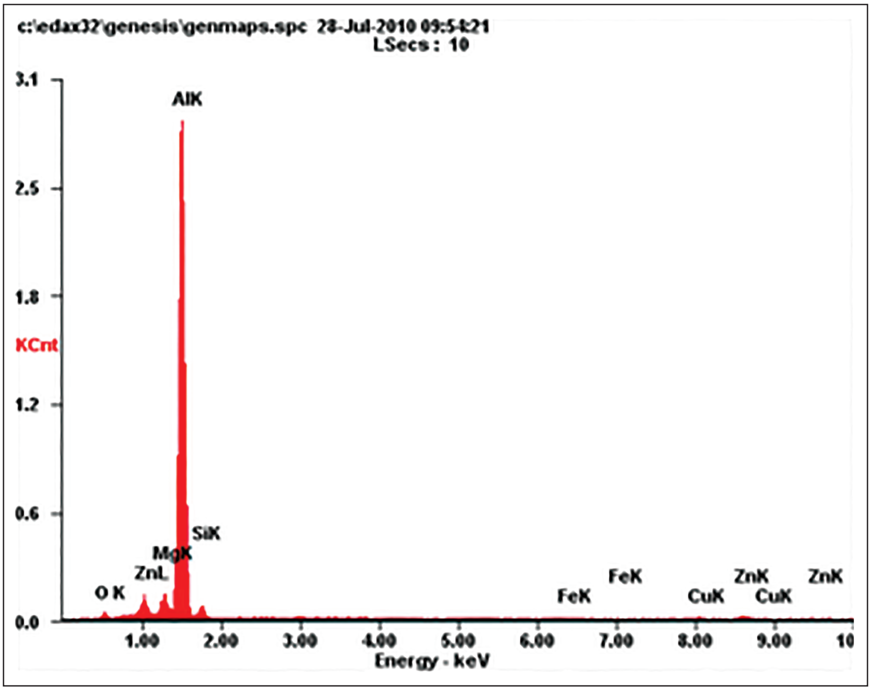

Figure 2. EDAX Profile of AA7075/15 wt% SiC (10–20 μm) Composite.

Table 1. Details of Inserts and Tool Holders.

Tool Holder	Insert	Clearance Angle (degree)	Back Rake Angle (degree)	Nose Radius (*r*) mm	Feed (*f*) mm/rev	Depth of Cut (mm)
PCLNL 2525 M12 KT 809	Carbide insert CNMG (a) 120404EM (b) 120408EM (c) 120412EM grade 6615	0°	7°	0.4 0.8 1.2	f_{min}= 0.15 f_{max} = 0.60	a_{pmin} = 1.0 a_{pmax} = 6.0

Inserts and tool holders shown in Table 1 were used for turning experiments.

AA7075/15 wt% SiC (10–20 μm) composite fabricated by means of stir casting was utilized for this investigation. Machining was done by CNC. The desired choice of the penetration of cut, speed of cutting and rate of feed can be achieved on CNC. Carbide inserts CNMG 120404EM, 120408EM and 120412EM grade 6615 were intended for turning. Choices of factors for experiments were finalized centred on the literature review and pilot experiments. Stages of factors are shown in Table 2. Electricity consumption was determined through a wattmeter, and a surface roughness tester measured surface roughness.

Table 2. Three-level Machining Parameters.

Factors	Parameters	First Level	Second Level	Third Level
1.	Rate of cutting (m/min)	90.0	150.0	210.0
2.	Rate of feed (mm/rev)	0.15	0.2.0	0.25
3.	Penetration of cut (mm)	0.20	0.40	0.60
4.	Radius of nose (mm)	0.40	0.80	1.20

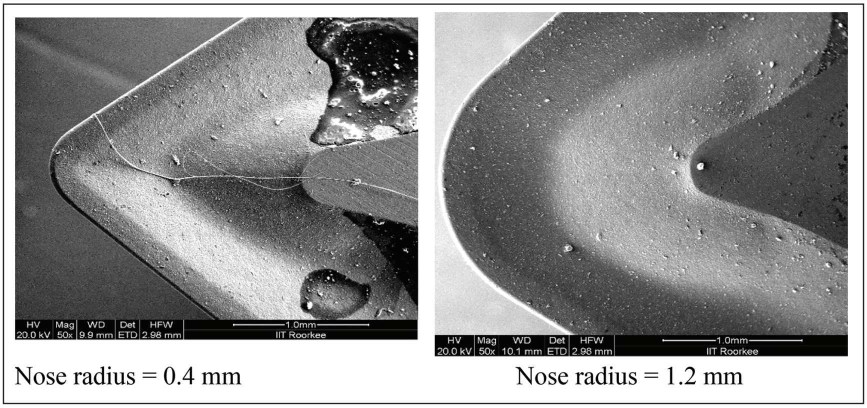

Nose radius = 0.4 mm

Nose radius = 1.2 mm

Figure 3. Tungsten Carbide Inserts Used in Experiments Before Machining.

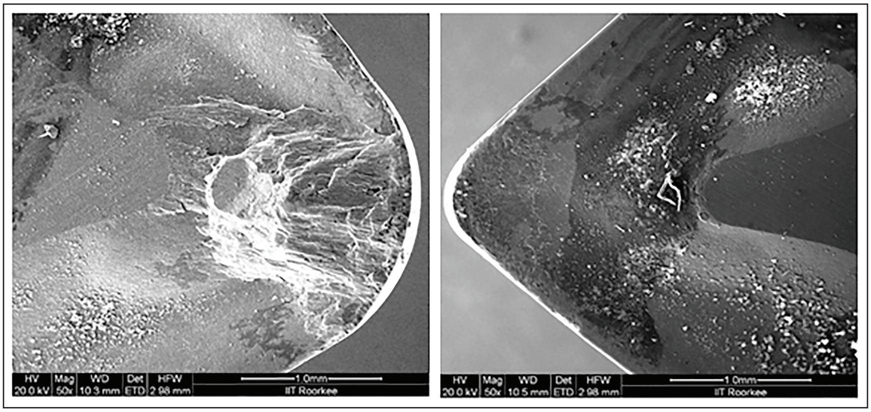

Figure 4. Wear of Tungsten Carbide Inserts Used in Experiments.

Tungsten carbide inserts of nose radius 0.4 and 1.2 mm used in experiments before machining are shown in Figure 3.

Cutting speed = 90 m/min, Feed = 0.25 mm/rev, Cutting speed = 90 m/min, Feed = 0.25 mm/rev, DOC = 0.6 mm, Nose radius = 1.2 mm. DOC = 0.6 mm, Nose radius = 0.4 mm.

Wear of tungsten carbide inserts of nose radius 0.4 and 1.2 mm used in experiments after machining is shown in Figure 4. The CNC turning machine is displayed in Figure 5.

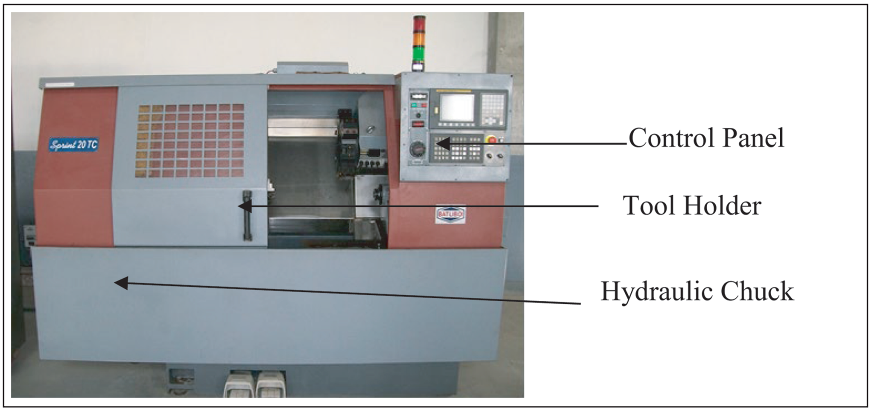

Figure 5. CNC Turning Machine.

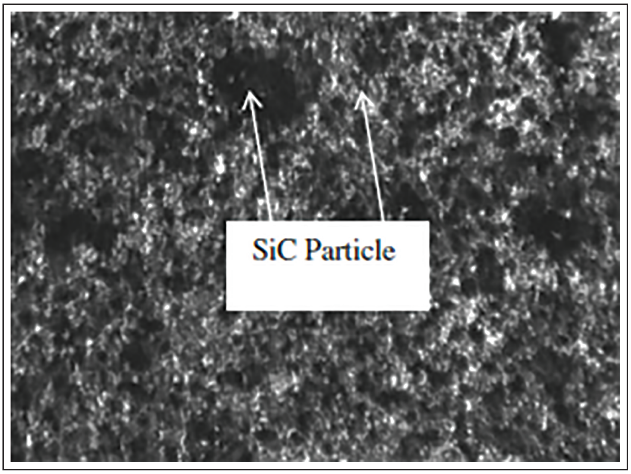

Figure 6. Micrographs of Machined Surface.

Micrographs of the machined surface in Figure 6 show that SiC particles are uniformly distributed. There is no pull-out of SiC particles.

Response Surface Methodology

Box and Wilson (1951) had suggested RSM for optimization of factors. RSM is modelling technique for finding association among numerous parameters and responses (Myers & Montgomery, 1995).

Face-centred Central Composite Design (FCCCD)

FCCCD is used when non-allowable functional circumstances occur at one specified level of design region. FCCCD necessitates only three stages of every trial variable (Montgomery, 2001).

Table 3. FCCCD for Four Variables at Three Levels.

Std	Speed of Cutting, (A); m/min	Rate of Feed, (B); mm/rev	Depth of Cut, (C); mm	Radius of Nose, (D); mm	Surface Roughness (μm)	Energy Consumption (Watt)
1	90	0.15	0.20	0.40	1.651	567
2	210	0.15	0.20	0.40	1.414	745
3	90	0.25	0.20	0.40	1.712	611
4	210	0.25	0.20	0.40	1.465	885
5	90	0.15	0.60	0.40	2.487	745
6	210	0.15	0.60	0.40	2.123	1,002
7	90	0.25	0.60	0.40	2.652	774
8	210	0.25	0.60	0.40	2.397	1,107
9	90	0.15	0.20	1.20	1.371	585
10	210	0.15	0.20	1.20	1.193	785
11	90	0.25	0.20	1.20	1.432	651
12	210	0.25	0.20	1.20	1.226	930
13	90	0.15	0.60	1.20	1.904	771
14	210	0.15	0.60	1.20	1.718	1,091
15	90	0.25	0.60	1.20	2.199	851
16	210	0.25	0.60	1.20	1.902	1,196
17	90	0.20	0.40	0.80	2.113	744
18	210	0.20	0.40	0.80	1.848	983
19	150	0.15	0.40	0.80	1.967	771
20	150	0.25	0.40	0.80	2.046	878
21	150	0.20	0.20	0.80	1.64	704
22	150	0.20	0.60	0.80	2.181	891
23	150	0.20	0.40	0.40	2.264	827
24	150	0.20	0.40	1.20	1.858	867
25	150	0.20	0.40	0.80	2.071	851
26	150	0.20	0.40	0.80	2.052	851
27	150	0.20	0.40	0.80	2.038	824
28	150	0.20	0.40	0.80	2.021	837
29	150	0.20	0.40	0.80	2.012	838
30	150	0.20	0.40	0.80	2.003	824

Table 4. Pooled ANOVA: Surface Roughness.

Sources	Sum of the Squares	*DF*	Mean of Squares	*F* Values	Probability > *F*
Model	3.73	8	0.47	230.91*	< 0.0001 significant
A	0.28	1	0.28	137.56*	< 0.0001
B	0.080	1	0.080	39.85*	< 0.0001
C	2.32	1	2.32	1,148.89*	< 0.0001
D	0.63	1	0.63	311.28*	< 0.00010.0030
A^2	0.023	1	0.023	11.22*	< 0.00010.0007
C^2	0.079	1	0.079	38.96*	< 0.0001
BC	0.032	1	0.032	15.71*	
CD	0.052	1	0.052	26.00*	
Residual	0.042	21	2.01E–003	3.67	0.078 not significant
Lack of fit	0.039	16	2.441E–003		
Pure error	3.315E–003	5	6.63E–004		
Cor. total	3.77	29			

Note: *The result is significant at the 95% confidence limit.

Experimental Design

AA7075/15 wt% SiC composite was machined through tungsten carbide inserts on a CNC turning set-up in accordance with the experimental scheme shown in Table 3.

Results

Variance Study

Analysis of variance was applied to assess the statistical significance of findings. Pooled form of ANOVA for surface coarseness is described in Table 4 and for energy consumption in Table 5.

1. Model *F*-amount of 230.91 shows the model is important. It can be seen that there is merely a 0.01% likelihood that 'Model *F*-Amount' so big may arise owing to noise.
2. The amount of 'Probability > *F*' smaller than 0.05 points that the model parameters are important, where A, B, C, D, A^2, C^2, BC and CD are important model parameters.
3. A lack-of-fit *F*-value of 3.67 suggests a 7.8% likelihood that the observed variation is attributable to noise. Meanwhile, the lack of fit is not noteworthy; the model can be considered adequate.

SD	0.045	R^2	0.988
Mean	1.90	Adjusted R^2.	0.984
C.V.	2.37	Predicted R^2	0.974
PRESS	0.097	Adeq. precision	59.88

Table 5. Pooled ANOVA: Energy Consumption.

Source	Sum of the Squares	*df*	Mean of Squares	*F* Value	Probability > *F*
Model	6.07E + 005	9	6,752.32	278.63*	< 0.0001 significant
A	3.26E + 005	1	3.267E + 005	1,348.16*	< 0.0001
B	3,744.72	1	3,744.72	154.53*	< 0.0001
C	2.14E + 005	1	2.145E + 005	885.20*	< 0.0001
D	1,196.89	1	1,196.89	49.36*	< 0.0001
A^2	3,143.48	1	3,143.48	12.97*	0.0018
C^2	4,412.15	1	4,412.15	18.21*	0.0004
AB	4,761.00	1	4,761.00	19.65*	0.0003
AC	6,561.00	1	6,561.00	27.07*	< 0.0001
CD	1,190.25	1	1,190.25	4.91*	0.0384
Residual	4,846.63	20	242.33	1.88	0.25 not significant
Lack of fit	4,117.13	15	274.48		
Pure error	729.50	5	145.90		
Cor. total	6.125E + 005	29			

* The result is significant at the 95% confidence limit.

4. 'Predicted *R*-squared' of 0.974 is in rational covenant with 'Adj. *R*-squared' of 0.984.

'Adeq. precision' calculates the signal-to-noise ratio. A ratio of more than 4 is desired. The ratio of 59.88 means a sufficient signal.

1. *F*-amount of 278.63 means model is important. It can be seen that merely a 0.01% likelihood that 'Model *F*-amount' so big may arise owing to noise.
2. Amount of 'Probability > *F*' smaller than 0.05 means model parameters are important. Here A, B, C, D, A2, C2, AB, AC and CD are important model terms.
3. 'Lack of fit *F*-amount' of 1.88 means lack of fit is not important relative to pure error. It can be seen that 25.08% likelihood that 'Lack-of-fit *F*-value' is so big, may be due to noise. A non-significant lack of fit confirms that the developed model can adequately represent and predict the experimental results.

SD	15.57	R^2	0.99
Mean	832.87	Adjusted R^2	0.98
C.V.	1.87	Predicted R^2	0.97
PRESS	12,707.62	Adeq. precision	70.15

4. 'Predicted *R*-squared' of 0.97 is in realistic covenant with 'Adjusted *R*-squared' of 0.98. 'Adeq. precision' finds the signal-to-noise ratio. Ratio > 4 is appropriate. The ratio of 70.15 points to a sufficient signal. The model is suitable for guiding navigation within the design space.

Coefficients of the Second-order Regression Equation

Regression coefficient of second order was found by utilizing investigational information (Table 3). The responses were modelled using regression equations as functions of the four process parameters measured in this experimentation. The results are presented below, and inconsequential coefficients have been excluded from the regression equations.

$$\begin{aligned}\text{Surface roughness} = {} & +0.753 + 4.684\text{E}-003 * A - 0.443 * B + 4.497 * C - 0.180 * D \\ & -2.251\text{E}-005 * A^2 - 3.776 * C^2 + 4.45 * B * C - 0.715 * C * D\end{aligned} \tag{1}$$

$$\begin{aligned}\text{Energy consumption} = {} & +400.975 - 2.09710 * A + 49.722 * B + 922.264 * C \\ & +21.319 * D + 8.391\text{E}-003 * A^2 - 894.758 * C^2 + 5.75 * A * B \\ & +1.687 * A * C + 107.812 * C * D\end{aligned} \tag{2}$$

Analysis for Surface Roughness [AA7075/15 wt% SiC (10–20 μm) Composite]

Figure 7 represents the normal probability of residuals. Normal plot vs. residuals exhibits data when 98% of residuals would lie inside 3σ. These experimental data are inside three 3σ. Predicted vs. actual (Figure 8) is quantified to demonstrate how efficiently the line can fit the two. The graph displays how this model foretells the range of data. Figure 8 indicates that experimental data align closely with a straight line.

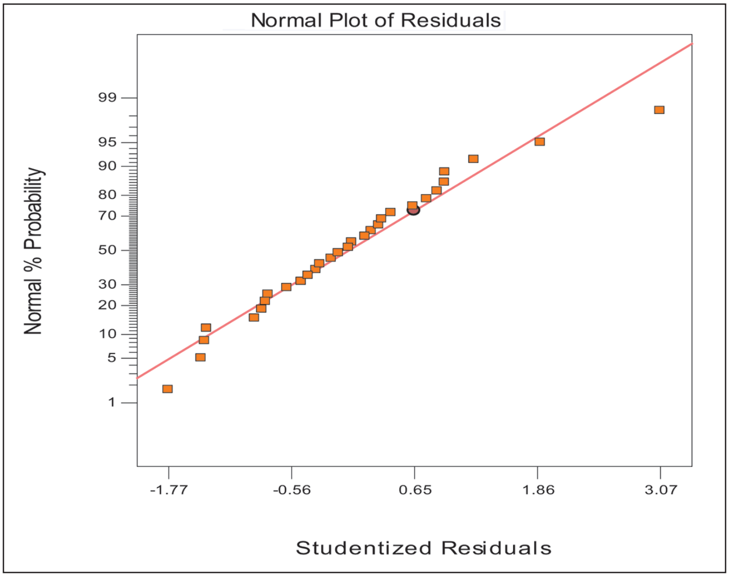

Figure 7. Normal Probability Distribution of Residuals: Surface Roughness.

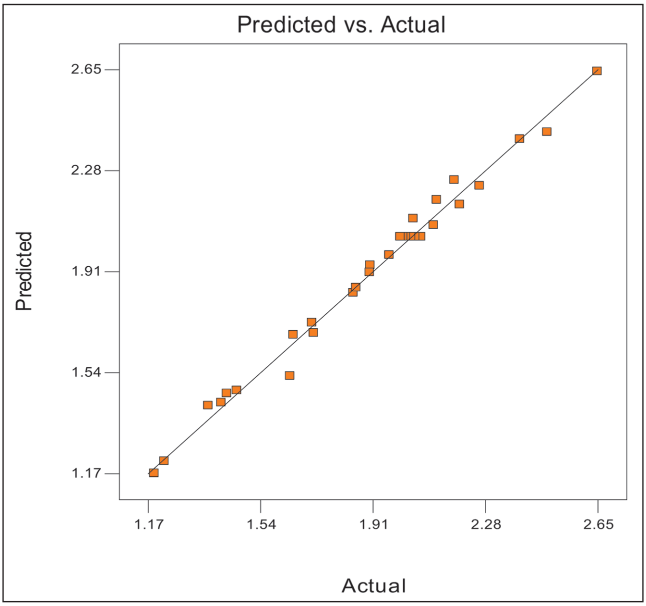

Figure 8. Predicted vs. Actual Surface Roughness.

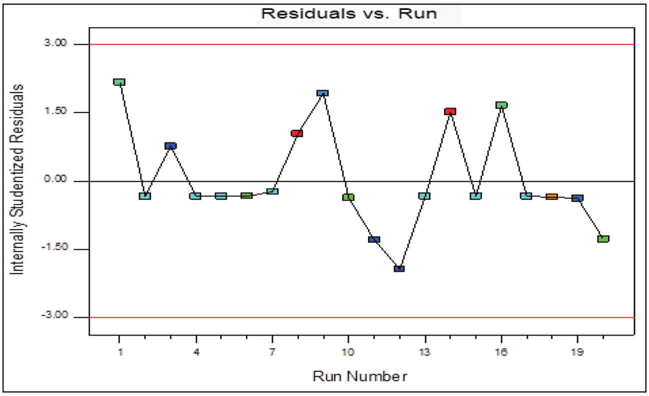

Figure 9. Residual vs. Run Order.

Residual vs. run order is shown in Figure 9. It displays that errors are independent. Results are not influenced by time-related outside factors. There is a random, horizontal band of points around the zero line. No discernible trends or patterns are witnessed.

The Box–Cox transformation is shown in Figure 10. This power transformation shows that variance is stabilized. The data are more normally distributed. Normality is important in this case.

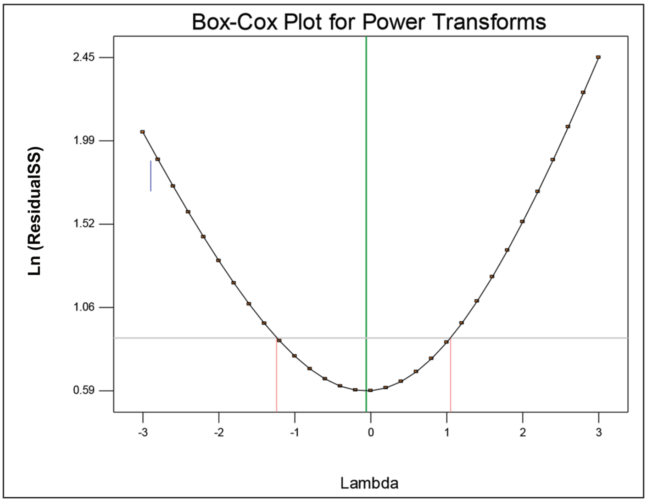

Figure 10. Box–Cox Transformation.

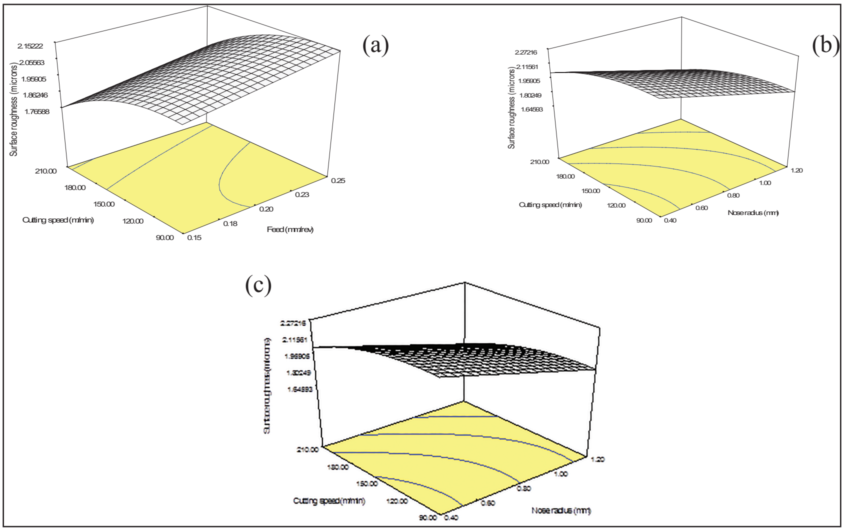

Figure 11. 3D Surface Curves for Surface Roughness (μm). (a) Impact of Cutting Speed and Feed on Surface Finish. (b) Surface Roughness Response to Speed of Cutting and Penetration of Cut. (c) Impact of Speed of Cutting and Radius of Nose on Surface Roughness.

Impact of Parameters on Surface Roughness

Figure 11(a) expresses the surface graph of surface coarseness, namely fluctuating speed of cutting and feed speed. The figure indicates that the escalation in the rate of cutting first upsurges, then lessens surface roughness. Growth in feed augments surface roughness. Figure 11(b) shows the impact of the speed of cutting and the penetration of the cut on surface coarseness. A rise in the penetration of cut enhances surface coarseness. Figure 11(c) represents the consequence of the speed of cutting and nose radius on surface coarseness. It is witnessed that surface coarseness will be lower when the nose radius is larger. Commencing these graphs, it is noticed that lesser surface roughness can be found only at minor values of feed and the penetration of cut, and greater levels of the speed of cutting and radius of nose.

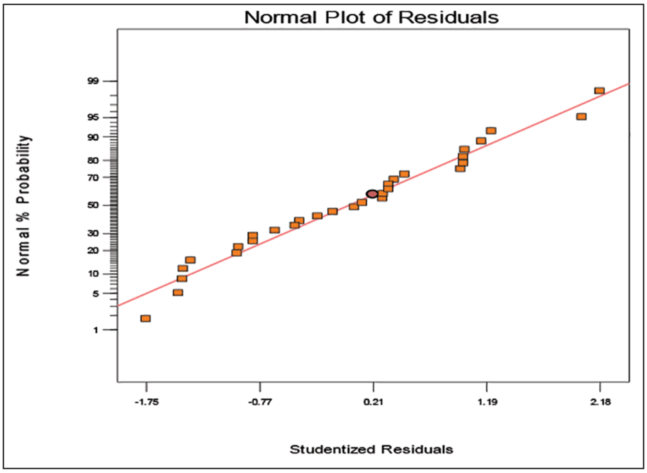

Figure 12. Normal Probability of Residuals: Energy Consumption.

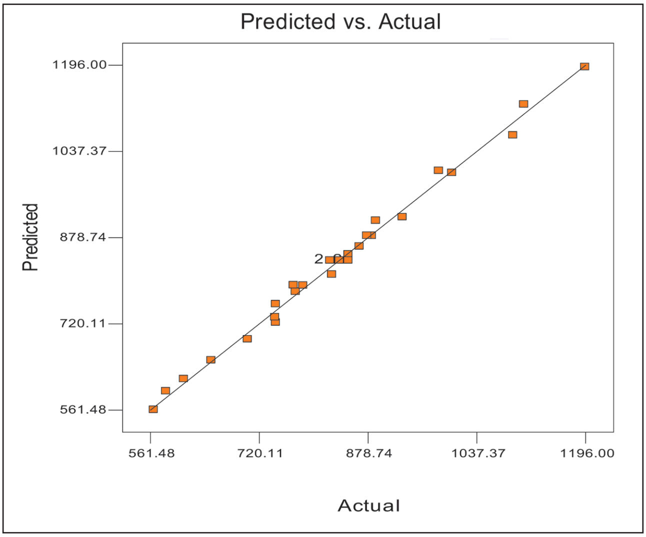

Figure 13. Predicted vs. Actual: Energy Consumption.

Analysis for Energy Consumption

Normal curve vs. residuals expresses residual information where 98% of residuals shall lie within 3 sigma. This investigational information is in 3 sigma (Figure 12). Residual vs. predicted is a quick test to ensure proper randomization is evident. Figure 13 indicates that experiments are properly randomized.

Effect of Factors on Energy Consumption

Figure 14(a) shows the surface curve of energy consumption, namely varying speed of cutting and feed. Electricity consumption improves sharply with the growth in the speed of cutting. Increasing the feed rate has minimal effect on energy consumption.

Figure 14(b) displays the consequences of a change in the speed of cutting and penetration of the cut on energy utilization. A rise in the penetration of cut augments energy utilization. It is witnessed that lesser energy utilization can be attained at a lesser penetration of the cut. Figure 14(c) depicts the influence of the speed of cutting and the radius of the nose on energy feeding. It is witnessed that energy utilization is increased when the nose radius is high.

Optimization of Cutting Parameters Using a Multi-objective Approach

A response optimization study was conducted to attain the least surface roughness and energy consumption by utilizing developed mathematical models. The desirability function method was utilized.

Desirability Function Approach

The value of desirability ranges between $d = 0$ and 1, which means the outcome is not acceptable. 1 means the response is the correctly targeted value (Jinshan et al., 2007). The response is converted into desirability as follows:

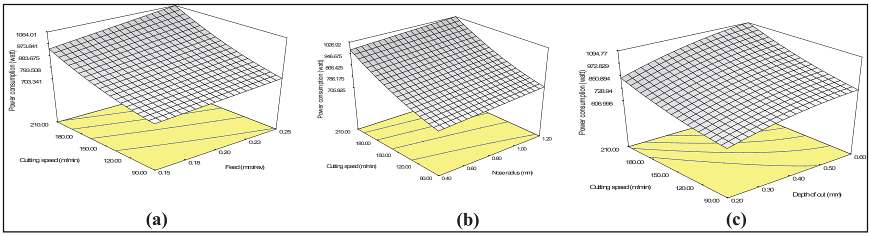

Figure 14. 3D Surface Curve for Energy Consumption (watt). (a) Impact of Speed of Cutting and Rate of Feed on Energy Utilization. (b) Impact of Speed of Cutting and Penetration of Cut on Energy Utilization. (c) Impact of Speed of Cutting and Radius of Nose on Energy Utilization.

$$d = \left|\frac{\bar{y} - L}{U - L}\right|^{\alpha}, \; L \le y^{-} \le U \text{ with } d = 0 \text{ for } y^{-} > U \tag{6}$$

and $d = 1$ for $y^{-} > L$.

α is weight. L and U were finalized as per the mathematical model in RSM.

Design-Expert was utilized for analysis. The desirability method was used for obtaining optimum results utilizing multi-response objectives (Dhupal et al., 2008; Jinshan et al., 2007). Optimization was carried out in two stages: (a) finding desirability for response and (b) maximization of desirability and detecting the optimum value. In the desirability approach, various results were achieved. Solution with maximum desirability is favoured.

Limitations for Optimization of Cutting Parameters

Desirability analysis was conducted to minimize surface coarseness and energy consumption simultaneously while allowing the parameters to vary from low limit to high limit.

Multi-Objective Optimization Results

Surface roughness and energy ingestion were minimized as per constraints in Table 6, through desirability analysis. A total of five solutions were generated. These are arranged in Table 7. Solution 1 at maximum desirability, that is, 0.884, is preferred. Optimum amount of the speed of cutting, rate of feed, penetration of cut and radius of nose to reduce surface coarseness (1.149) and energy ingestion (595.79 watt) are 90.02 m/min, 0.15 mm/rev, 0.20 mm and 1.20 mm.

Figure 15 shows a contour chart at the maximum desirability amount. Figures 16 and 17 show a contour graph of surface roughness and energy consumption. Point prediction for multi-response optimization is shown in Table 8. Results show that variations are within limits.

In Figure 18, the red points on the graphs show optimum values. Red points on curves response also show corresponding values of surface roughness and energy

Table 6. Limitations for Optimization of Values.

Response	Constraint	Lower Limit	Upper Limit	Lower Weight	Upper Weight	Importance
Speed of cutting	Within range	90	210	1	1	3
Rate of feed	Within range	0.15	0.25	1	1	3
Penetration of cut	Within range	0.2	0.6	1	1	3
Radius of nose	Within range	0.4	1.2	1	1	3
Surface roughnes (μm)	Minimum	1.193	2.652	1	1	5
Energy consumption (watts)	Minimum	567	1,196	1	1	3

Table 7. Multi-criteria Optimization Results.

Solution No.	Speed of Cutting (m/min)	Rate of Feed (mm/rev)	Depth of Cut (mm)	Radius of Nose (mm)	Surface Roughness (μm)	Power Consumption (watt)	Desirability	Selection
1	90.02	0.15	0.20	1.20	1.419	595.79	0.884	Selected
2	90.00	0.15	0.20	1.18	1.427	595.82	0.881	
3	90.41	0.17	0.20	1.20	1.428	606.96	0.874	
4	110.76	0.15	0.20	1.20	1.424	612.56	0.873	
5	90.00	0.17	0.20	1.20	1.429	609.18	0.872	

Table 8. Point Prediction: Multi-response Optimization.

Parameter	Prediction	SE Mean	95% CI Low	95% CI High	SE Pred	95% PI Low	95% PI High
Surface roughness	2.037	0.014	2.01	2.07	0.047	1.94	2.14
Power consumption	2.14	4.71	826.40	846.03	16.26	802.29	870.14

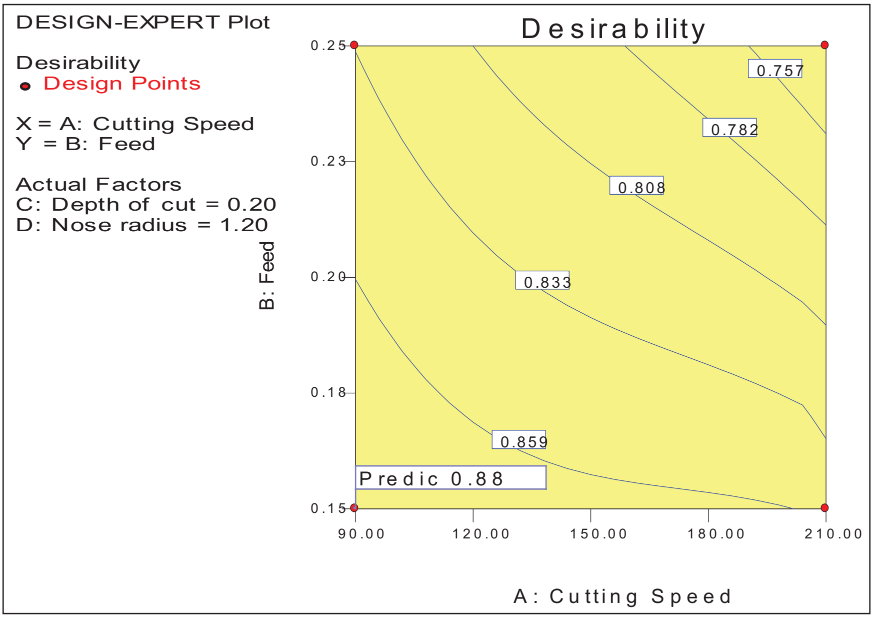

Figure 15. Contour Graph at Maximum Desirability.

consumption. Figure 19 shows individual and combined desirability values. Desirability amount for surface roughness is 0.813, and desirability amount for energy consumption is 0.972. Their combined desirability value is 0.884.

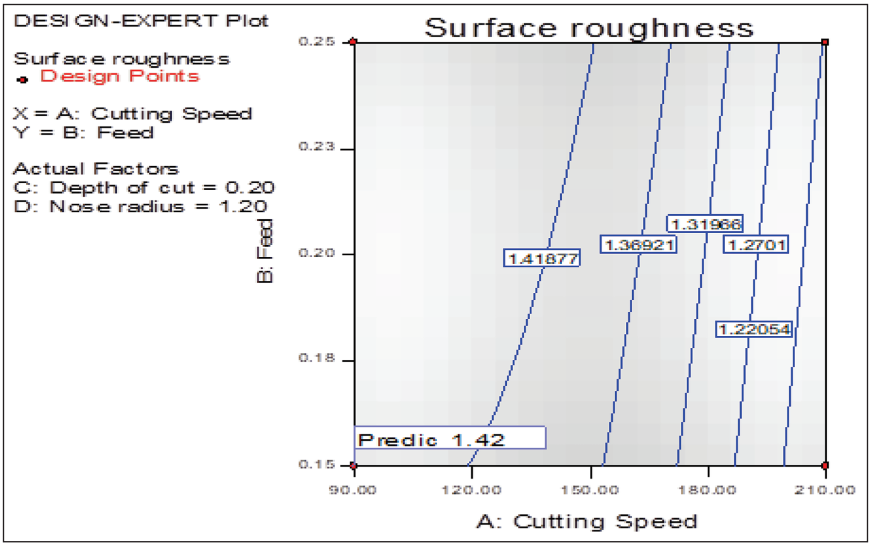

Figure 16. Contour Chart Surface Roughness: Cutting Speed.

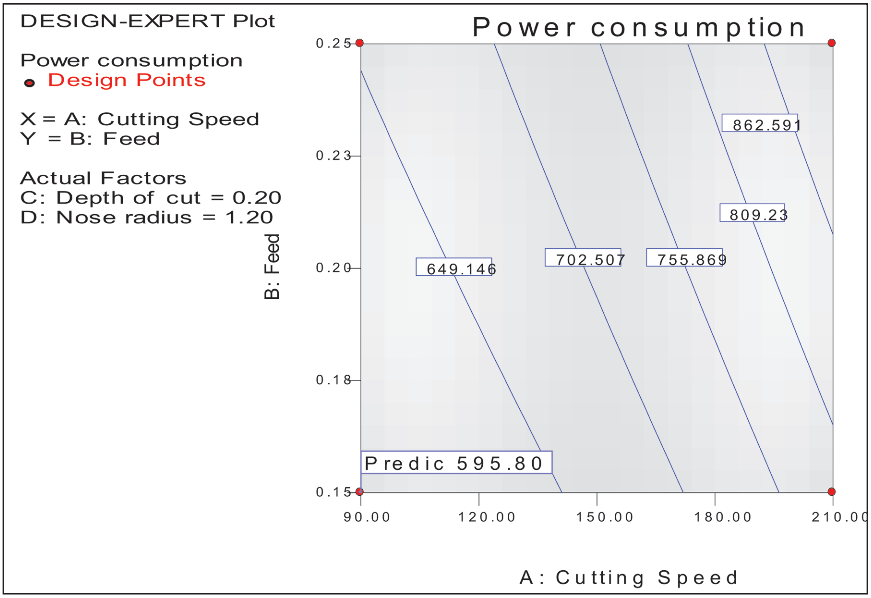

Figure 17. Contour Chart Energy Consumption: Cutting Speed.

End Result

Experimental (minimum), single objective and multi-objective values of surface roughness are 1.193, 1.191 and 1.419 µm, respectively. Experimental (minimum), single-objective optimization and multi-objective optimization values of energy

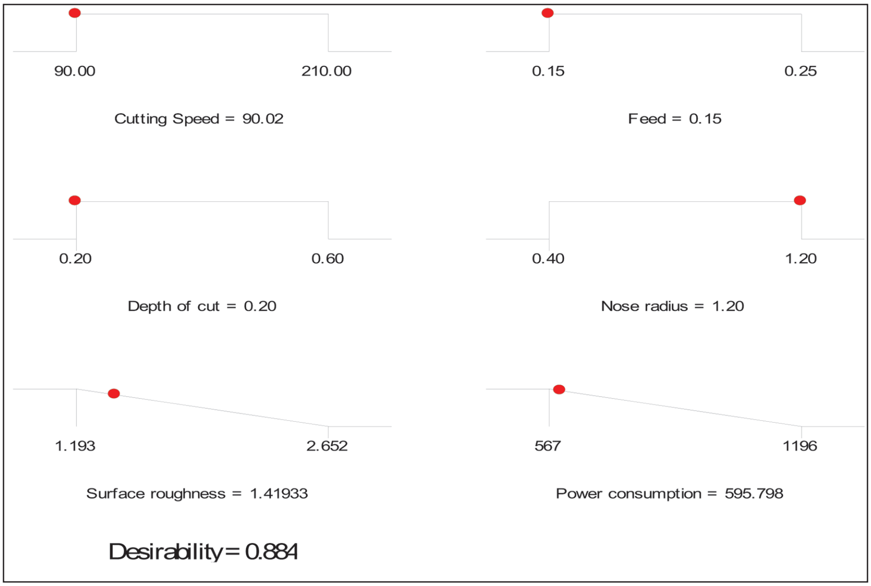

Figure 18. Ramp Function Curve for Combined Desirability.

utilization are 567, 566.71 and 595.79 watts, respectively. This shows that simultaneous optimization (multi-criteria optimization) of surface roughness and energy utilization is at the cost of % rise in surface roughness and % increase in power utilization as related to their single criteria optimization values.

The % change in surface roughness owing to multi-objective optimization

$$= \frac{1.419 - 1.191}{1.419} \times 100 = 16.06\%$$

The % change in energy consumption due to multi-objective optimization

$$= \frac{595.79 - 566.71}{595.79} \times 100 = 4.88\%.$$

Hence, 16.06% reduction in surface roughness can be achieved by merely increase of 4.88% in energy consumption.

No	Cutting Speed (m/min)	Feed (mm/rev)	DOC (mm)	Nose Radius (mm)	Surface Roughness (μm)	Energy Consumption (watts)
AA7075/15 wt% SiC (10–20 μm) composite	97	0.15	0.20	0.40	1.643	570.5

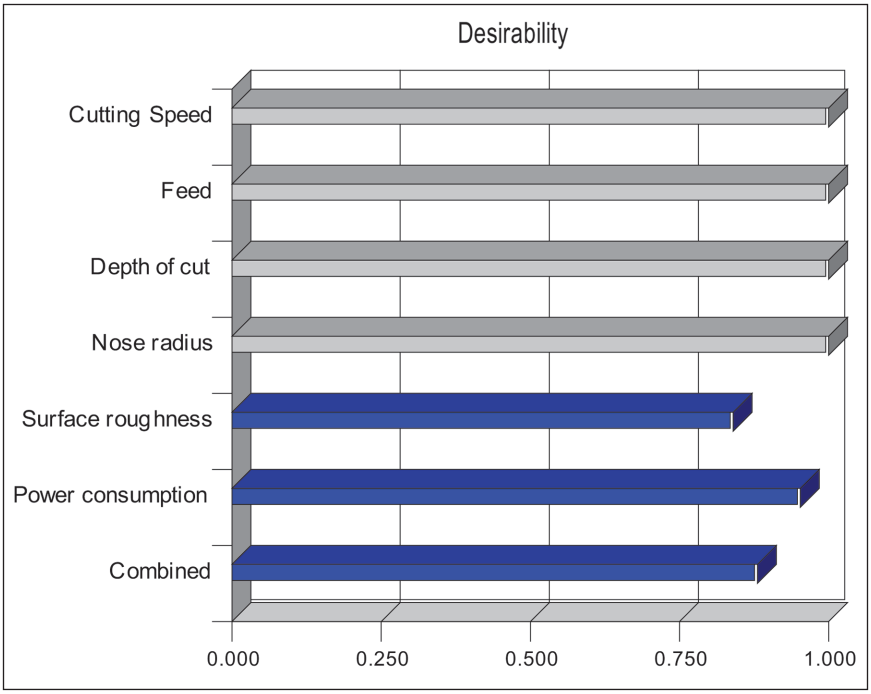

Figure 19. Individual and Combined Desirability Value.

Experimental Validation of Results

Turning experiments were carried out again at the optimal cutting conditions obtained by desirability analysis for AA7075/15 wt% SiC (10–20 µm) composite. The values of response parameters, that is surface roughness and electricity consumption, are close to values obtained by desirability analysis. This validates our work.

Discussions

Surface Roughness

Surface roughness (*R*a) obtained on turned surfaces of composite rods was greater than that of alloys. Throughout turning, pulling of SiC particles results in minor holes on the turned surface. This situation resulted in the rise of the surface roughness of composites. Surface coarseness of composite rods that have a greater reinforcement ratio is more than that of rods that have a comparatively lower reinforcement ratio.

Surface roughness affects the performance of components when they are used in a mechanism. It also evaluates the machining accuracy. The speed of cutting, rate of feed, penetration of cut and nose radius have a major influence on surface roughness. Semi-continuous chips are formed during the turning of AA7075/

SiC-p composites. This is a result of the presence of SiC particles. Discontinuous chips create macro cracks on the open surface of chips. This leads to bend creation. That sequentially removes SiC particulates, which leads to the formation of minor cavities on the surface during turning. This is also one of the reasons for more surface roughness while turning Al/SiC composites.

Outcome of Speed of Cutting

Cutting speed has a major impact on surface roughness. Surface roughness reduces at greater cutting speeds (Figure 11a). The chip fractures freely at a lower cutting speed. This produces a rough surface. This is because of the existence of harder SiC particles. SiC particles do not play a major role in cutting at low speed. Cutting at low speed is due to the cutting tool side. SiC particulates slide on the tool edge and damage the turned surface. As the speed rises, chip fracture reduces and hence roughness declines. The speed of cutting has the maximum intense influence on surface roughness. At large, when higher cutting speeds are utilized, less surface roughness can be attained.

Outcome of Rate of Feed and Penetration of Cut

Increase in feed augments surface roughness (Figure 11b). When the feed is raised, regular loads on the tool are also enhanced. Hence, it will produce heat, which further enhances surface roughness. Rise in the penetration of the cut produces more regular pressure and concentrates on the rake surface. Henceforth, surface coarseness augments with growth in depth of cut (Figure 11c).

Surface coarseness is enhanced at greater feed in all turning circumstances. This was ascribed to the elevated temperature in the cutting zone. Greater feed enhances temperature, and this leads to reduced bonding amongst SiC-p and Al matrix. Al relaxes, and SiC particles are released.

Effect of Nose Radius

Chip thickness changes from zero to extreme while turning by a large nose radius tool, which tends to move a big part of the chips in place of cropping them. This decreases surface roughness (Figure 11c). A bigger nose radius minimizes the saw tooth's impact of feed marks and considerably lessens surface roughness. An additional nose radius is nevertheless detrimental since it creates vibration and chatter.

Energy Consumption

Influence of Speed of Cutting and Feed Rate

Figure 14(a) shows the surface curve of energy consumption with changing speed and feed. Energy consumption increases sharply with a rise in speed. As speed rises, the material removal rate also enhances compelling machine to draw extra energy. Wear of the tool also results in extra energy consumption, as the turning process is not smooth.

Normally, as speed rises, the heat created at the interface of the tool and component increases. Hence, the major part of the heat generated enters the component. Increased heat generation results in softening of the Al matrix. In AA7075/15 wt% SiC (10–20 μm) composite turning, the major part of electricity is spent in eradicating hard reinforcement particles from the gluey matrix. Numerous investigations (Lin et al., 1995; Tomac & Tonnessen, 1992) have shown that normally reinforcements are moved out from the matrix instead of being cropped. Thus, higher speed results in relaxation of the matrix. This reduces specific energy. Therefore, MMC turning should be conducted at greater speeds. Speed will be limited by tool wear, as raising speed after a value will result in rapid tool wear and become economically nonviable (Andrews et al,. 2000; Muthukrishnan et al., 2008). The rise in feed has a slight impact on the energy utilization.

Influence of Depth of Cut

Figure 14(b) displays the impact of the speed of cutting and the penetration of the cut on energy utilization. Rise in depth of cut improves energy consumption in turning of AA7075/15 wt% SiC (10–20 μm). It is observed that less consumption can be attained at a minor depth of cut (Kumar, 2013).

Effect of Nose Radius

Figure 14(c) depicts the effect of cutting speed and radius of nose on energy consumption. It is observed that energy consumption is additional at a large nose radius. Alike results were attained by Kumar (2013).

Conclusions

The following conclusions can be drawn:

1. 3D surface curves of surface roughness discovered that depth of cut is the most noteworthy parameter, followed by feed, cutting speed and nose radius.
2. 3D surface curves of energy consumption show that cutting speed is utmost noteworthy parameter subsequently by depth of cut, rate of feed and radius of nose.
3. Ramp function graphs show the correct value of factors for the required level of response.
4. Optimization by desirability approach indicated that the lowest surface roughness (1.191 μm) would be obtained at a cutting speed of 209.47 m/min, feed of 0.15 mm/rev, depth of cut of 0.20 mm and nose radius of 1.18 mm.
5. Optimization by desirability approach indicated that the lowest energy consumption (566.71 watts) would be obtained at a cutting speed of 93.25 m/min, feed of 0.15 mm/rev penetration of cut of 0.20 mm and nose radius of 0.41 mm.
6. Multi-objective optimization values of factors for minimum surface roughness (1.419 μm) and energy consumption (595.79 watts) are cutting speed of 90.02 m/min, feed of 0.15 mm/rev depth of cut of 0.20 mm and nose radius of 1.20 mm.

7. 16.06% reduction in surface roughness could be obtained by merely increase of 4.88% in energy consumption.

Relate the Optimization Results to Practical Machining Strategies

When the turning of composite will be carried out at process parameters obtained from multi-response optimization, there will be a reduction in the surface roughness of the machined surface, with a marginal increase in electrical energy consumption. These values of process parameters may be used for the turning of composites.

Limitations

It will be difficult to machine the composites, with more than 15 wt% of SiC particles and particle size more than 20 μm.

Directions for future research

Limited research has been conducted on the machining behaviour of metal–matrix composites. A number of problems during the machining of MMC still need a solution. Some of them are:

i. Identification of a specific tool for a particular MMC.
ii. Balance in the values of conflicting responses during the machining of MMCs.

Declaration of Conflicting Interests

The author declared no potential conflicts of interest with respect to the research, authorship and/or publication of this article.

Funding

The author received no financial support for the research, authorship and/or publication of this article.

References

Andrews J. E., C., Feng, H.-y., & Lau, W. M. (2000). Machining of an aluminium–SiC composite using diamond inserts. *Journal of Materials Processing Technology*, *102*, 25–29.

Antony, J. (2000). Multi-response optimization in industrial experiments using Taguchi's quality loss function and principal component analysis. *Quality and Reliability Engineering International*, *16*, 3–8.

Basheer, A. C., Dabade, U. A., Joshi, S. S., Bhanuprasad, V. V., & Gadre, V. M. (2008). Modeling of surface roughness in precision machining of metal matrix composites using ANN. *Journal of Materials Processing Technology*, *19–7*, 439–444.

Box, G. E. P., & Wilson, K. B. (1951). On the experimental attainment of optimum conditions. *Journal of Royal Statistical Society*, *13*, 1–45.

Choudhury, I. A., & EI-Baradie, M. A. (1997). Surface roughness prediction in the turning of high-strength steel by factorial design of experiments. *Journal of Materials Processing Technology*, *67*, 55–61.

Davim, J. P. (2002). Diamond tool performance in machining metal–matrix composites. *Journal of Materials Processing Technology*, *128*, 100–105.

Dhupal, D., Doloi, R., & Bhattacharyya, B. (2008). Parametric analysis and optimization of Nd:YAG laser micro-grooving of aluminium titanate (Al_2TiO_5) ceramics. *International Journal of Advanced Manufacturing Technology*, *36*(9–10), 883–893.

El-Gallab, M., & Sklad, M. (1998). Machining of Al:SiC particulate metal matrix composites Part II: Workpiece surface integrity. *Journal of Materials Processing Technology*, *83* 277–285.

Jinshan, L., Cuiqing, Y. M., Yan, L., Wei, Z., & Ping, X. (2007). Medium optimization by combination of response surface methodology and desirability function: An application in glutamine production. *International Journal of Advanced Manufacturing Technology*, *74*, 563–571.

Kılıckap, E., Cakır, O., Aksoy, M., & Inan, A. (2005). Study of tool wear and surface roughness in machining of homogenised SiC-p reinforced aluminium metal matrix composite. *Journal of Materials Processing Technology*, *164–165*, 862–867.

Kumar, B. R. (2013). Optimization of cutting parameters for minimizing power consumption and maximizing tool life during machining of Al alloy SiC particle composites. *Journal of Cleaner Production*, *39*, 242–254.

Lee, B. Y., Tarng, Y. S., & Lii, H. R. (2000). An investigation of modeling of the machining database in turning operations. *Journal of Materials Processing Technology*, *105*, 1–6.

Lin, J. T., Bhattacharyya, D., & Lane, C. (1995). Machinability of a silicon carbide reinforced aluminium metal matrix composite. *Wear*, *181–183*, 883–888.

Lin, W. S., Lee, B. Y., & Wu, C. L. (2001). Modeling the surface roughness and cutting force for turning. *Journal of Materials Processing Technology*, *108*, 286–293.

Lindberg R. A. (1990). *Processes and materials of manufacture* (4th ed.). Prentice-Hall.

Montgomery D. C. (1997). *Design and analysis of experiments* (4th ed.). Wi1ey.

Montgomery D. C. (2001). *Design and analysis of experiment* (5th ed.). Wiley.

Muthukrishnan, N., Murugan, M., & Prahlada Rao, K. (2008). Machinability issues in turning of Al-SiC (10p) metal matrix composites. *The International Journal of Advanced Manufacturing Technology*, *39*, 211–218.

Myers, R. H., & Montgomery, D. C. (1995). *Response surface methodology: Process and product optimization using design experiments*. John Wiley & Sons.

Ozben, T., Kilickap, E., & Cakır, O. (2008). Investigation of mechanical and machinability properties of SiC particle reinforced Al-MMC. *Journal of Materials Processing Technology*, *198*, 220–225.

Thiele, J. D., & Melkote, S. N. (1999). Effect of cutting-edge geometry and workpiece hardness on surface generation in the finish hard turning of AlSI 52100 steel. *Journal of Materials Processing Technology*, *94*, 216–226.

Thomas, H., & Chanderasekaran, H. (1997). Influence of cutting medium on tool wear during turning. Report IM-3118, Swedish Institute for Metal Research.

Tomac, N., & Tonnessen, K. (1992). Machinability of particulate aluminium matrix composites. *CIRP Annals*, *41*, 55–58.

Yang, W. H., & Tarng, Y. S. (1998). Design optimization of cutting parameters for turning operations based on Taguchi method. *Journal of Materials Processing Technology*, *84*, 112–129.

Article

Influence of Precipitation on the Mechanical Properties and Age-hardening Response of Mg–10Sn

Sustainable Manufacturing and
Foundry Practices
1(1) 52–63, 2026
© The Author(s) 2026
DOI: 10.1177/IIF.261437165
Journal.indianfoundry.org
THE INSTITUTE OF INDIAN FOUNDRYMEN

Tapabrata Maity[1], Sonika Chahar[1], Palash Poddar[2], Konda Gokuldoss Prashanth[3] and Debdas Roy[1]

Abstract

Comprehensive attention has been focused globally on producing lightweight Mg-based alloys for automotive applications, which can perform well at operating temperatures (200–300°C). This study examines the age-hardening behavior of Mg–10Sn alloys for enhanced performance. Room-temperature tensile investigations show that artificially aging for 100 h at 200°C maximizes both tensile strength and ductility. Thermal aging at 200°C for 100 h significantly increases work hardening capabilities, evidenced by a high strain-hardening rate ($\theta = 2.10$) and a hardening exponent (n) of 0.4167. This elevates the necking stress to 122 MPa and boosts load-bearing capacity (H_C) from $H_C = 0.63$ to 0.75 in Mg–10Sn alloy. The observed trend in strain-hardening behavior suggests a two-stage work-hardening response, driven by the precipitation of Mg_2Sn intermetallic at α-Mg grain boundaries, which significantly enhances the strength.

Keywords

Mg–10Sn alloy, age hardening, mechanical properties, tensile behavior

---

[1] Materials and Metallurgical Engineering Department, National Institute of Advanced Manufacturing Technology (formerly NIFFT), Hatia, Ranchi, Jharkhand, India
[2] National Metallurgical Laboratory, Jamshedpur, Jharkhand, India
[3] Department of Mechanical and Industrial Engineering, Tallinn University of Technology, Tallinn, Estonia

Corresponding author:
Debdas Roy, Materials and Metallurgical Engineering Department, National Institute of Advanced Manufacturing Technology (Formerly NIFFT), Hatia, Ranchi 834003, Jharkhand, India.
E-mail: droy2k6@gmail.com

Introduction

Magnesium alloys provide a good balance of exceptional damping capacity, superior heat dissipation, high specific strength, superior castability, and machinability for lightweight structural materials (Ghosh & Naryanan, 2008). Recently, in the automobile and aerospace sectors, the demand for lightweight material has inevitably increased to reduce gas emissions and save fuel consumption. Promisingly, Mg-alloys, particularly die-cast Mg–Zn and Mg–Al, offer superior strength-to-weight ratios than aluminum (Pollock, 2010; Wang, M. Y. et al., 2012). Further, with the need for weight reduction, Mg-alloys are increasingly used in the automobile sector for components like steering columns, steering wheels, gearboxes and seat frames (Kimura et al., 2009).

Medium-strength Mg–Sn and Mg–Sn–Al alloys are prime auto body-sheets candidates, offering superior formability, high specific strength, and resistance to corrosion (Nakata & Kamado, 2023; Wan et al., 2021). While at low temperatures, Mg-alloys show poor formability due to their hexagonal crystal structure (hcp), fewer slip systems, and a pronounced basal texture (Elsayed et al., 2013). Alloying tunes the structural properties, but high concentrations limit room-temperature ductility (Peng et al., 2023).

AZ91 and AM Mg-alloys are preferred for automobile structural components due to superior castability and strength (Koren et al., 2002; You et al., 2017). However, high-temperature instability limits their use in high-temperature applications; likewise, the low melting point (437°C) of the Mg17Al12 phase compromises creep resistance (Srinivasan et al., 2010). Mg–Sn system remains a promising heat-resistant alloy under thermal load (Gibson et al., 2010). High tin (Sn) solubility (~14.7%) facilitates significant precipitation hardening via Mg_2Sn precipitation, and its high melting point (770°C) provides superior thermal stability than Mg-RE systems. However, Sn imposes poor ductility. Brittle Mg_2Sn phases along the grain boundaries deteriorate ductility, limiting their usage in automotive sectors (Mendis et al., 2006). Moreover, as tin is a non-toxic and necessary element, the Mg–Sn system holds enormous promise in biomedical implants.

Enhancing age-hardening ability is popular in metallic materials to improve mechanical performance in metallic alloys. Artificial aging is traditionally used to tailor the age-hardening behavior of various Mg-alloys, which include Mg–Sn (Mendis et al., 2006), Al-Mg–Zn (Deng et al., 2023), Mg-RE (Li et al., 2019), Mg-Si (Yamamoto et al., 2020), and Al–Mg–Si (Zhu et al., 2019). This study investigates the age-hardening response of Mg–10Sn alloys at operating temperatures of 200-300ºC and its impact on mechanical properties. This temperature range is relevant, as it matches the standard warm forming condition often employed for Mg-based sheets.

Experimental

An Mg–10Sn (wt%) alloy was fabricated via casting. Initially, a portion of the total Mg was charged and melted in a crucible inside a furnace, and then adequate Sn was added. To avoid excessive oxidation during melting, the stepwise-charging practice of Mg ingots was adopted. The oxide layer on the top was skimmed out completely and regularly. Following flux application and addition of Sn, the mixture was held for 30 min at 750°C to ensure complete dissolution. Subsequently, the melt was cast into ingots in a preheated crucible (250°C) inside a furnace in an argon atmosphere. Then cast samples were subjected to T4 treatment, which involved heating to 300°C for 8 h. followed by water quenching to room temperature. The process (T4) was conducted in a mild steel box covered with sand to avoid oxidation. Finally, the samples were artificial aged (T6) in a muffle furnace in an oil bath at 200°C for 100 and 500 h, respectively. At regular intervals, samples were removed from the furnace and quenched in water at room temperature. The resulting conditions were denoted as 100 h/200°C and 500 h/200°C Mg–10Sn alloys, respectively.

Tensile property was evaluated using specimens with dimensions of 30 × 6 × 6 mm^3 using Instron 8501 universal testing machine at a crosshead velocity and strain rates of 0.03 mm/s and 10^{-3}/s, respectively. Tensile samples were prepared using wire electrical discharge machining. To mitigate data fluctuations caused by shrinkage porosity, all samples were extracted from the center of the ingots. Structure and microstructure of the cast and aged specimens were identified using a Rigaku SmartLab, Japan X-ray diffractometer (40 kV/40 mA) with Cu–Kα radiation and JEOL-JSM840A scanning electron microscope (SEM) fitted with an energy-dispersive spectroscope (Oxford Instruments, Abingdon, UK). The microstructure after tensile deformation was investigated by SEM. Vickers hardness was measured using a Leica-VMHT, Germany, tester with 25 gf load and 10 s dwell time.

Results and Discussion

Phase Structure Identification

Figure 1 shows the XRD spectrum of the as-cast and 100 h/200°C and 500 h/200°C Mg–10Sn specimens. It reveals peaks from *hcp* α-Mg as the primary solid solution and intermetallic β-Mg_2Sn phases only. The calculated average crystallite size (D) and lattice parameter (α) of the phases are shown in Table 1. It shows prolonged aging increases the crystallite size in both α-Mg and β-Mg_2Sn precipitates significantly, while their lattice parameters remain unaltered. Furthermore, mass fraction calculations indicate the occurrence of precipitation reaction in the sample aged at 200°C for 100 h, which shows reaching a peak volume of β-Mg_2Sn precipitates up to $V_f^{\beta}{}_{100}$ = 19%. While aging continues to 500 h, the mass fraction of these precipitates declined to $V_f^{\beta}{}_{500}$ = 11%.

Effect of Aging on the Microstructural Formation

Figure 2 displays the optical micrograph of the alloy in as-cast, 100 h/200°C, and 500 h/200°C conditions. The microstructure of the cast alloy shows a dendritic morphology, characterized by a brighter matrix and a darker eutectic phase localized in the interdendritic regions. However, samples aged at 200°C for 200 and 500 h exhibited significant coarsening of dendrites, which increased with holding time. High-resolution SEM images in Figure 3(a–c) show a microstructure composed of a bright, primary α-Mg matrix and a dark, semi-coherent network of

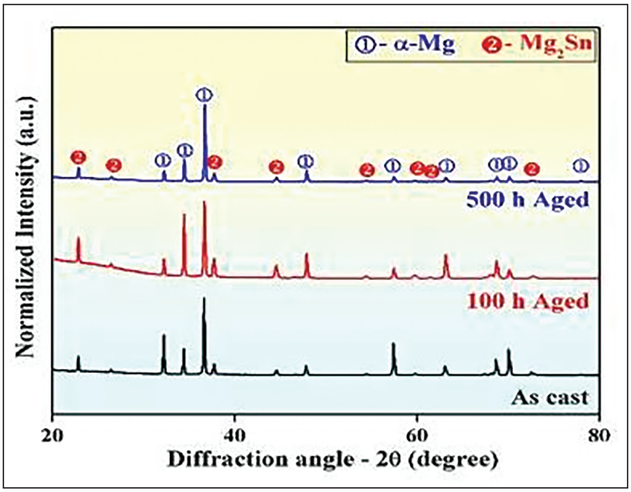

Figure 1. X-ray Diffraction Analysis of the As-cast, 100 h/200°C, and 500 h/200°C Samples Revealed a Phase Composition Consisting of Primary hcp α-Mg Solid Solution and Intermetallic β-Mg_2Sn.

Table 1. X-ray Diffraction Profile Analysis Data Showing the Lattice Parameter and Crystallite Size for the As-cast, 100 h/200°C, and 500 h/200°C Mg–10Sn specimens.

Sample Description	Lattice Parameter – α (Å)		Crystallite Size – *D* (Å)	
	α-Mg	β-Mg_2Sn	α-Mg	β-Mg_2Sn
As-cast	3.212 ± 0.002	6.754 ± 0.004	278 ± 24	384 ± 16
100 h/200°C	3.210 ± 0.002	6.756 ± 0.001	647 ± 62	556 ± 12
500 h/200°C	3.200 ± 0.002	6.761 ± 0.003	1,224 ± 49	1,019 ± 41

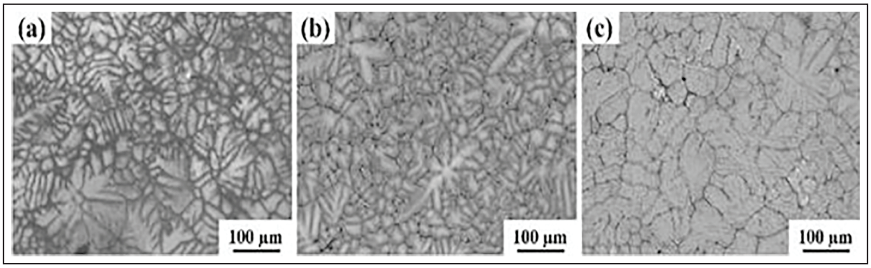

Figure 2. The Optical Micrography Images Show the Microstructure of the Mg10Sn Alloys in the Following Conditions: (a) as-cast, (b) 100 h/200°C, and (c) 500 h/200°C, respectively.

α-Mg+β-Mg_2Sn eutectic mixture located along the grain boundaries (Zhang et al., 2017). Additionally, traces of lath-shaped β-Mg_2Sn precipitates are present within the α-Mg grains. Figures 3b and c show that the amount of lath-shaped β-Mg_2Sn precipitates increases with aging time (Table 2). Hence, as high-temperature (300°C) T4 treatment facilitates Sn diffusion into the matrix to form a solid

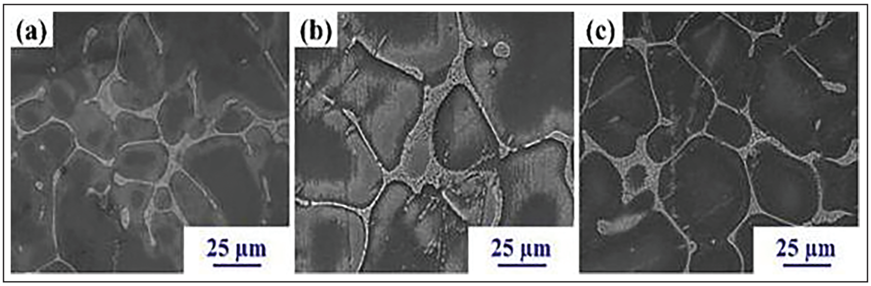

Figure 3. SEM Images Revealing the Microstructure of (a) as-cast specimen consists of primarily the α–Mg matrix (dark areas), and Sn-rich eutectic (α-Mg+β-Mg_2Sn) segregated along the Mg grain boundaries forming a semicontinuous network. However, traces of β-Mg_2Sn can be found within the matrix of α-Mg grains in a lath-shaped structure in the thermally treated (b) 100 h/200°C and (c) 500 h/200°C Mg–10Sn specimens.

Table 2. X-ray Diffraction Profile Analysis Data Furnishing the Volume Fraction of α-Mg and β-Mg_2Sn Phases Present in the As-cast, 100 h/200°C, and 500 h/200°C Mg–10Sn Specimens.

	Lattice Parameter – α (Å)	
Sample Description	α-Mg (V_f^{α})	β-Mg_2Sn (V_f^{β})
As-cast	91 ± 4	9 ± 4
100 h/200°C	81 ± 1	19 ± 1
500 h/200°C	89 ± 1	11 ± 1

solution, quenching suppresses Sn diffusion, resulting in a lath-shaped β-Mg_2Sn precipitate. Conversely, holding at a lower temperature (200°C) for 100 and 500 h (in aged 100 h/200°C and 500 h/200°C specimens) causes slow Sn diffusion, leading to an increased concentration/formation of the eutectic structure (${V_f}^{\beta}{}_{100} =$ 19% and ${V_f}^{\beta}{}_{500} =$ 11%). Further aging up to 500 h, Sn partitions into the eutectic α-Mg+β-Mg_2Sn, leading to a continuous network morphology accompanied by the coarsening of the eutectic phases.

Influence of Precipitation on the Mechanical Property

The room-temperature engineering tensile stress–strain curves are shown in Figure 4a and are documented in Table 3. The as-cast specimen showed a yield strength of $\sigma_y \sim 76$ MPa, a tensile strength $\sigma_U \sim 137$ MPa, and a fracture strain of $\varepsilon_f \sim 4\%$. While aging at 200°C left σ_y nearly unchanged ($\sigma_y \sim 75$ MPa) for 100 h before it declines to $\sigma_y \sim 68$ MPa after 500 h. Nevertheless, σ_U peaks at approximately $\sigma_U \sim 145$ MPa after 100 h of aging before it subsequently declines to $\sigma_U \sim 126$ MPa after 500 h aging. Prolonged aging reduced ductility from $\varepsilon_f \sim$ 4.25% (100 h) to $\varepsilon_f \sim 3$ % (500 h). Furthermore, the 500 h/200°C specimen exhibited more pronounced serrations in tensile curves, suggesting unstable plastic flow.

Fracture Analysis

Figure 4 (b–d) shows fracture surface morphology of the as-cast, 100h/200°C, and 500h/200°C specimens, respectively. In the cast specimen (Figure 4b), the region around marked *A* shows smooth brittle facets, *B* shows small dimples (plastically deformed area), *C* shows cavities formed by the extraction of grains, *D* shows flutes, and *F* shows small dimples. Flutes are striations or river patterns which are a common fractographic feature in *hcp* materials (Merson et al., 2020). Fluted fracture surfaces typically result from nucleation of tubular voids at the intersection of basal slip and prismatic/pyramidal slip bands. Flat facets and flute patterns indicate a cleavage mode of fracture in the as-cast specimens, while localized small dimples suggest the prior plastic deformation before failure, leading to quasi-cleavage fracture in the cast Mg–10Sn alloy (Jiang et al., 2023; Merson et al., 2020). While the fracture surface of the 100 h/200°C specimen in Figure 4(c) shows the presence of quasi-cleavage, the presence of deeper dimples suggests extensive plastic deformation (Kondori etal., 2014; Shabani et al., 2019). Fracture surface of the 500 h/200°C specimen (Figure 4d) shows flutes or a river pattern, marking the evidence of PLC event recorded during tensile deformation. Further, fluted surfaces around *A–B* show a small amount of plastic deformation around *C*, indicating a quasi-cleavage mode of fracture. Additionally, cracks around the GBs show specimens' poor ductility and brittleness.

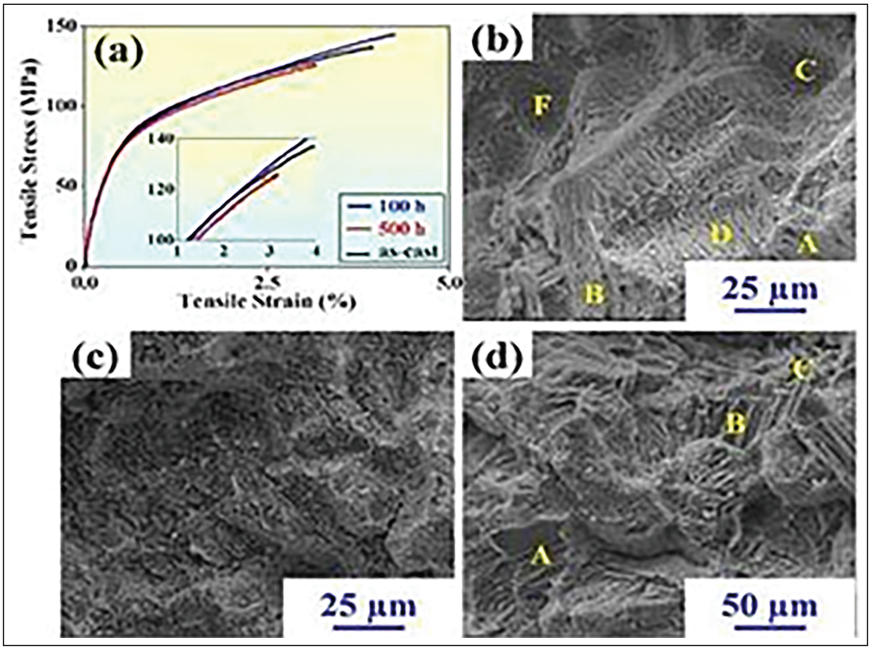

Figure 4. (a) Tensile engineering stress–strain curves for the as-cast, 100 h/200°C, and 500 h/200°C specimens at room temperature. (b)–(d) show their corresponding fracture surface morphology of the cast, 100 h/200°C, and 500 h/200°C alloys, respectively.

Age-hardening Response as a Function of Aging Time

Table 3 shows Young's modulus (*E*) of the specimens gradually increasing with the aging duration from up to 24 GPa, while hardness values remain unaltered. Figure 5 shows the effect of AA on hardness and mechanical properties as a function of aging duration.

Work-hardening Capacity (σc)

The work-hardening capacity ($\sigma_C = \sigma_S / \sigma_y - 1$) was assessed to evaluate the deformation behavior of the cast and aged specimens. As shown in Table 3, the aged alloys exhibited superior load-bearing ability with σ_C values reaching $\sigma_C \sim$ 0.75 compared to $\sigma_C \sim 0.63$ for the as-cast state (Afrin et al., 2007; Luo et al., 2006). Thus, β-Mg_2Sn precipitate phases are vital to the load-bearing ability of the Mg–10Sn alloy.

Strain-hardening Rate (θ)

Figure 6 shows the representative strain-hardening rate ($\theta = d\sigma_T / d\varepsilon_T$, where σ_T and ε_T are true stress and true strain, respectively) vs. true strain curves (Shi et al., 2023). Throughout the plastic deformation regime, the 100 h/200°C specimen shows a higher strain-hardening rate (θ = 2.10) than both the as-cast

Table 3. The Room-Temperature Mechanical Properties Data Observed for the Mg–10Sn As-cast, 100 h/200°C and 500 h/200°C Aged Samples, Respectively.

Alloy Designation	σ_Y (MPa)	σ_{UTS} (MPa)	ε_f (%)	Hardness (HV)	*E* (GPa)	σ_c	θ
As-cast	76.0	137.0	4.0	41.0	19.0	0.63	2.02
100 h/200°C	75.0	145.0	4.3	41.2	20.0	0.75	2.10
500 h/200°C	68.0	126.0	3.0	41.7	24.0	0.75	1.73

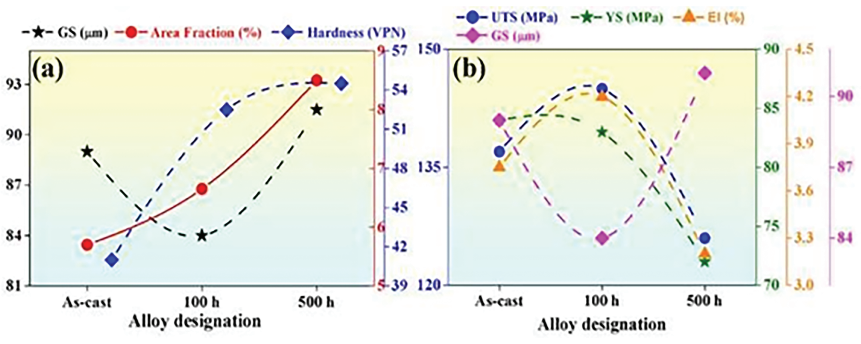

Figure 5. The Plot Shows the Hardness and Mechanical Properties of the Mg–10Sn alloy in the As-cast, 100 h/200°C, and 500/200°C Alloys as a Function of Aging Duration.

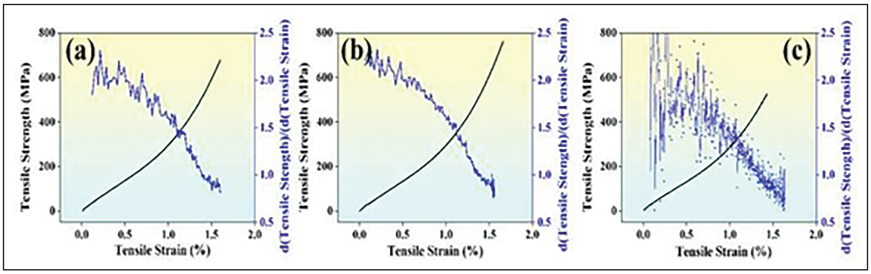

Figure 6. Representative Strain-Hardening Rate – True Strain Curves from the Engineering Tensile Data of the As-cast, 100 h/200°C, and 500 h/200°C Specimens, Respectively.

(θ = 2.02) and 500 h/200°C (θ = 1.73) samples. Further, the onset of necking (plastic instability) occurred at the highest strain ($\varepsilon_T = 0.45$) in the 100 h/200°C specimen (σ_T = 122 MPa), reflecting superior ductility compared to 500 h/200°C (ε_T = 0.39, σ_T = 58 MPa) and as-cast specimen (ε_T = 0.38, σ_T = 103 MPa). Apart from that, the gradual decline of θ up to plastic instability (Figure 6) suggests that age-hardened Mg–10Sn alloys undergo steady-state work hardening.

Strain-hardening Exponent (n)

Hollomon expressions were utilized to determine the strain-hardening exponent (n) (Shabani et al., 2019):

$$\sigma = K\varepsilon^{n}, \tag{1}$$

$$n = d\left(ln\sigma\right) / d\left(ln\varepsilon\right), \tag{2}$$

where σ, ε, and K correspond to stress, strain, and constant, respectively, listed in Table 4. Figure 7 shows that the 100 h/200°C specimen exhibited the maximum strain-hardening exponent (n = 0.4167), which signifies superior formability compared to the as-cast (n = 0.4065) and the 500 h/200°C (n = 0.3947) specimens. Further, the dual-slope behavior suggests a transition from a high-rate non-homogeneous deformation (n_1) to a lower/moderate homogeneous deformation (n_2) regime. These values match high-formability standards (0.2–0.5) and are comparable to Mg–Yb (n = 0.45) (Zhang et al., 2021) and Mg–3Al–3Sn (n = 0.45) (Wang, H. Y. et al., 2012) and surpass several high-strength steels (Chen et al., 2005; Xu et al., 2012).

Discussion

In the initial regime, the 100 h/200°C specimen (where n_1 = 0.6232) relies on precipitate to bear the primary load during deformation. Interestingly, the 500 h/200°C specimen reached a maximum n_1 = 0.6433, which correlates with its

Table 4. The Strain Hardening Exponents (*n*) Calculated from the Room-temperature Mechanical Test Observed for the Mg–10Sn As-cast, 100 h/200°C and 500 h/200°C Samples, Respectively.

Alloy Designation	η	R^2	η_I	R^2	η_2	R^2
As-cast	0.4065	0.9321	0.6191	0.9832	0.2660	0.9994
100 h/200°C	0.4167	0.9497	0.6232	0.9864	0.3039	0.9984
500 h/200°C	0.3947	0.9549	0.6433	0.9921	0.2999	0.9938

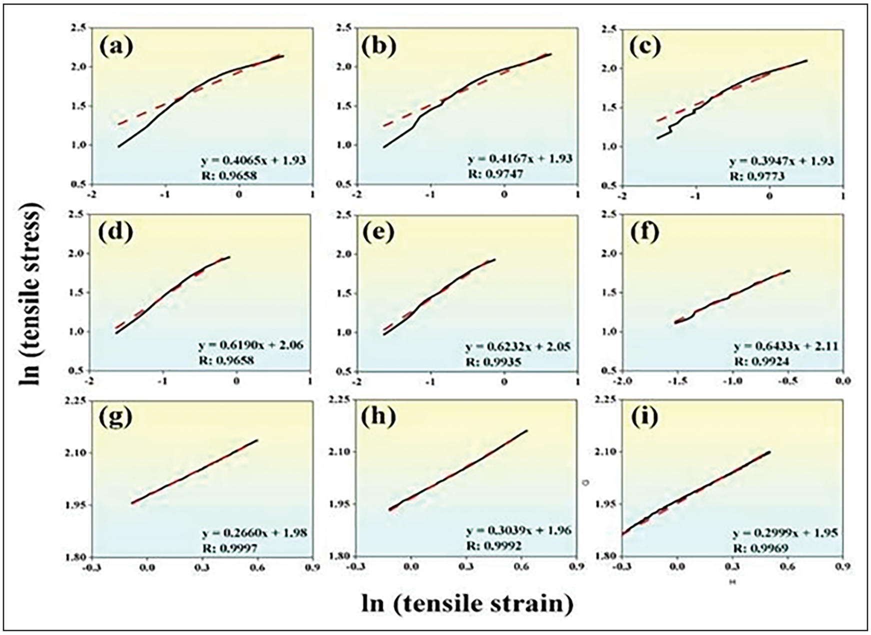

Figure 7. Data Postulating the Constructive Parameters of the Hollomon Expression Revealing the Two Regimes During Strain Hardening Where the 100 h/200°C Alloy Has the Highest Strength with True SHE 0.3039 Than the As-cast and 500 h/200°C Sample.

elevated Young's modulus of 24 GPa. During the second regime ($n_2 = 0.3039$), the 100 h/200°C specimen transitions to more homogeneous deformation facilitated by the particle–matrix interactions. The 100 h/200°C specimen achieves a superior average SHE, $n = 0.4167$, because its microstructure contains a maximum volume fraction of β-Mg_2Sn (19%) precipitates. During the second hardening stage ($n_2 = 0.3039$), this microstructure delays localized deformation, effectively extending uniform strain and enhancing ductility. These observations are consistent with fractographic evidence showing superior plastic flow in the 100 h/200°C specimens.

Mechanistically, the high-volume fraction of β-Mg_2Sn ($V_f^{\beta} = 19\%$) phase precipitates act as the primary load-bearing phase within the α-Mg matrix. In Mg–10Sn alloy, it is evident that precipitation on α-Mg grain matrix significantly enhances the age-hardening response compared to basal precipitation (Nie, 2003). In the 100 h/200°C specimen, these precipitations are more prevalent than in the 500 h/200°C specimens. Consequently, as strain increases, dislocation–dislocation interactions on the slip planes are intensified by the precipitation's barriers. The limited ability of dislocations to bypass these particles results in a high hardening rate (θ = 2.10), ultimately yielding a superior combination of ductility $\varepsilon_f = 4.3\%$, strength $\sigma_S = 145$ MPa, and load-bearing capacity, $\sigma_C = 0.75$.

Conclusions

Based on the findings, we conclude:

1. 1. Artificial aging (AA) at 200°C for 100 h effectively facilitates the precipitation of β-Mg_2Sn strengthening phases with a peak volume fraction of 19%. In contrast, exceeding the aging duration to 500 h results in over-aging, characterized by coarser β-Mg_2Sn precipitates and a coarser eutectic structure compared to the 100 h condition.
2. 2. The specimens aged at 200°C for 100 h achieve an optimal balance of mechanical properties and superior strain-hardening rate ($\theta = 2.10$). This performance is significantly attributed to β-Mg_2Sn reinforcement (V_f = 19%), which functions as the primary load-bearing constituent.
3. 3. Fractographic analysis confirms a transition toward a more ductile quasi-cleavage mode in the 100-h aged specimen, supported by the deeper dimples, stable plastic flow and superior formability ($n = 0.4167$).

Declaration of Conflicting Interests

The authors declared no potential conflicts of interest with respect to the research, authorship, and/or publication of this article.

Funding

The authors received no financial support for the research, authorship, and/or publication of this article.

References

Afrin, N., Chen, D. L., Cao, X., & Jahazi, M. (2007). Strain hardening behavior of a friction stir welded magnesium alloy. *Scripta Materialia*, *57*(11), 1004–1007.

Chen, X. H., Lu, J., Lu, L., & Lu, K. (2005). Tensile properties of a nanocrystalline 316L austenitic stainless steel. *Scripta Materialia*, *52*(10), 1039–1044.

Deng, Y., Sun, W., Yang, Y., Zhan, H., Yan, K., & Zeng, G. (2023). Effects of Mg2Sn precipitation on the age-hardening and deformation behaviour of a Mg–Sn–Al–Zn alloy. *Materials Science and Engineering: A*, *867*, 144714.

Elsayed, F. R., Sasaki, T. T., Mendis, C. L., Ohkubo, T., & Hono, K. (2013). Compositional optimization of Mg–Sn–Al alloys for higher age hardening response. *Materials Science and Engineering: A*, *566*, 22–29.

Gibson, M. A., Fang, X., Bettles, C. J., & Hutchinson, C. R. (2010). The effect of precipitate state on the creep resistance of Mg–Sn alloys. *Scripta Materialia*, *63*(8), 899–902.

Ghosh, R., & Naryanan, G. (2008). Control of three phase, four wire PWPM rectifier. *IIEE Transactions on Power Electronics*, *24*(6), 1444–1452.

Jiang, J., Tong, L., Xu, Z., Bi, G., Cao, C., Li, Y., Chen, T., Fu, W., & Fang, D. (2023). Improvement in the age-hardening response of Mg–7Sn alloy by compressive stress-assisted aging. *Journal of Materials Research and Technology*, *23*, 2601–2611.

Kimura, R., Hatayama, H., Shinozaki, K., Murashima, I., Asada, J., & Yoshida, M. (2009). Effect of grain refiner and grain size on the susceptibility of Al–Mg die casting alloy to cracking during solidification. *Journal of Materials Processing Technology*, *209*(1), 210–219.

Kondori, B., & Benzerga, A. A. (2014). Effect of stress triaxiality on the flow and fracture of Mg alloy AZ31. *Metallurgical and Materials Transactions A*, *45*(8), 3292–3307.

Koren, Z., Rosenson, H., Gutman, E. M., Unigovski, Y. B., & Eliezer, A. (2002). Development of semisolid casting for AZ91 and AM50 magnesium alloys. *Journal of Light Metals*, *2*(2), 81–87.

Li, G., Zhang, J., Wu, R., Liu, S., Song, B., Jiao, Y., Yang, Q., & Hou, L. (2019). Improving age hardening response and mechanical properties of a new Mg–RE alloy via simple pre-cold rolling. *Journal of Alloys and Compounds*, *777*, 1375–1385.

Luo, J., Mei, Z., Tian, W., & Wang, Z. (2006). Diminishing of work hardening in electroformed polycrystalline copper with nano-sized and uf-sized twins. *Materials Science and Engineering: A*, *441*(1–2), 282–290.

Mendis, C. L., Bettle, C. J., Gibson, M. A., & Hutchinson, C. R. (2006). An enhanced age hardening response in Mg–Sn based alloys containing Zn. *Materials Science and Engineering: A*, *435–436*, 163–171.

Merson, E., Poluyanov, V., Myagkikh, P., Merson, D., & Vinogradov, A. (2020). Fractographic features of technically pure magnesium, AZ31 and ZK60 alloys subjected to stress corrosion cracking. *Materials Science and Engineering: A*, *772*, 138744.

Nakata, T., & Kamado, S. (2023). Towards tailoring basal texture of rolled Mg alloy sheet by recrystallization for high room-temperature formability: A review. *Journal of Magnesium and Alloys*, *11*(11), 3992–4010.

Nie, J. F. (2003). Effects of precipitate shape and orientation on dispersion strengthening in magnesium alloys. *Scripta Materialia*, *48*(8), 1009–1015.

Peng, P., Yu, D., Guo, X., Zhang, P., Chai, S., Dai, Q., & Lu, J. (2023). Significant improvement in formability and ductility of AZ31 Mg alloy by differential temperature rolling. *Journal of Materials Research and Technology*, *26*, 1293–1305.

Pollock, T. M. (2010). Weight loss with magnesium alloys. *Science*, *328*(5981), 986–987.

Shabani, A., Toroghinejad, M. R., Shafyei, A., & Logé, R. E. (2019). Evaluation of the mechanical properties of the heat treated FeCrCuMnNi high entropy alloy. *Materials Chemistry and Physics*, *221*, 68–77.

Shi, Q., Wang, C. J., Deng, K. K., Fan, Y. D., Nie, K. B., & Liang, W. (2023). Work hardening and softening behaviours of Mg-Zn-Gd-Ca alloy regulated by bimodal microstructure. *Journal of Alloys and Compounds*, *938*, 168606.

Srinivasan, A., Swaminathan, J., Gunjan, M. K., Pillai, U. T. S., & Pai, B. C. (2010). Effect of intermetallic phases on the creep behavior of AZ91 magnesium alloy. *Materials Science and Engineering: A*, *527*(6), 1395–1403.

Wan, Y. J., Zeng, Y., Zeng, Q., Song, B., Huang, X. F., Qian, X. Y., & Jiang, B. (2021). Simultaneously improved strength and toughness of a Mg–Sn alloy through abundant prismatic lath-shaped precipitates. *Materials Science and Engineering: A*, *811*, 141087.

Wang, H. Y., Nan, X. L., Zhang, N., Wang, C., Wang, J. G., & Jiang, Q. C. (2012). Strong strain hardening ability in an as-cast Mg–3Al–3Sn alloy. *Materials Chemistry and Physics*, *132*(2–3), 248–252.

Wang, M. Y., Xu, Y. J., Jing, T., Peng, G. Y., Fu, Y. N., & Chawla, N. (2012). Growth orientations and morphologies of α-Mg dendrites in Mg–Zn alloys. *Scripta Materialia*, *67*(7–8), 629–632.

Xu, T., Feng, Y., Jin, Z., Song, S., & Wang, D. (2012). Determination of the maximum strain-hardening exponent. *Materials Science and Engineering: A*, *550*, 80–86.

Yamamoto, K., Takahashi, M., Kamikubo, Y., Sugiura, Y., Iwasawa, S., Nakata, T., & Kamado, S. (2020). Effect of Mg content on age-hardening response, tensile properties, and microstructures of a T5-treated thixo-cast hypoeutectic Al–Si alloy. *Materials Science and Engineering: A*, *798*, 140089.

You, S., Huang, Y., Kainer, K. U., & Hort, N. (2017). Recent research and developments on wrought magnesium alloys. *Journal of Magnesium and Alloys*, *5*(3), 239–253.

Zhang, D., Zhang, D., Zhang, Y., Chen, S., Xu, T., & Meng, J. (2021). Analysis of strain hardening behavior in a ductile Mg–Yb based alloy. *Materials Science and Engineering: A*, *819*, 141462.

Zhang, Y., Liu, J. P., Chen, S. Y., Xie, X., Liaw, P. K., Dahmen, K. A., Qiao, J. W., & Wang, Y. L. (2017). Serration and noise behaviours in materials. *Progress in Materials Science*, *90*, 358–360.

Zhu, X., Yang, H., Dong, X., & Ji, S. (2019). The effects of varying Mg and Si levels on the microstructural inhomogeneity and eutectic Mg2Si morphology in die-cast Al–Mg–Si alloys. *Journal of Materials Science*, *54*(7), 5773–5787.

Article

Chemistry-driven Predictive Modelling of Mechanical Performance in 42CrMo4 (AISI 4140) Steel with Machine Learning

Sustainable Manufacturing and
Foundry Practices
1(1) 64–79, 2026
© The Author(s) 2026
DOI: 10.1177/IIF.261438647
Journal.indianfoundry.org
THE INSTITUTE
OF INDIAN
FOUNDRYMEN

Subhasis Das Gupta[1], Abhinav Anand[2] and Ram Krishna[1]

Abstract

The 42CrMo4 low-alloy steel shafts, gears, and other high-strength parts used in the automotive industry offer a strong balance of toughness, strength, and surface quality. Traditionally, alloy development has relied on empirical knowledge and repeated experimental trials to adjust chemical composition and achieve targeted mechanical properties. In this study, we developed a machine learning model to predict the mechanical properties of 42CrMo4 steel from its chemical composition. Our dataset comprised 1,000 heat measurements listed as weight percentages, along with tensile strength, yield strength, proof stress at 0.2%, and surface roughness (R_a) from machining. After removing anomalous data with extreme or inconsistent compositional values, nine key alloying elements, Ti, Ni, Cr, Mo, Cu, Mn, P, Si, and C, were selected as input parameters for the machine learning model. Different machine learning models were trained separately for each identified property, ensuring tailored predictions. We tune their hyperparameters using a five-fold cross-validation grid search, helping us find the best settings. The Gradient Boosting Regressor algorithm performs well, showcasing its effectiveness and reliability, with R^2 values ranging from 0.64 to 0.73 across the four targets, indicating reliable predictions. Additionally, error metrics such as root

---

[1] Department of Metallurgical and Materials Engineering, National Institute of Technology Jamshedpur, Jharkhand, India.

[2] Department of Electronics, Electronics and Computer Science Engineering, KIIT Bhubaneswar, Odisha, India

Corresponding author:
Ram Krishna, Department of Metallurgical and Materials Engineering, National Institute of Technology Jamshedpur, Jamshedpur, Jharkhand 831014, India.
E-mails: krishnamme@gmail.com; krishna.met@nitjsr.ac.in; sdg.habra@gmail.com

mean squared error and mean absolute error indicate that proposed predictions remain within practical engineering limits, providing confidence in their accuracy. To improve the model, we employed important grouped features and correlation heatmaps for our analyses. These show that Ti, Ni, Cr, and Mo contribute most to strength properties, while Mn, P, and Si have a greater impact on R_a. Further, the results are comparable to the metallurgical information on solid-solution strengthening, carbide formation, and surface finish sensitivity. The suggested framework demonstrates that composition-based machine learning models can support alloy design, reduce experimental trials, and provide a digital tool for predicting the mechanical properties of 42CrMo4 steel.

Keywords

42CrMo4 steel, low-alloy steel, machine learning algorithms, Gradient Boosting Regressor, mechanical properties

Introduction

Low-alloy, quenched-and-tempered steels such as 42CrMo4 are commonly used in the automotive, energy, and general engineering sectors. Widely used components include shafts, axles, gears, and heavy-duty fasteners, for which steel designers demand high strength, good fatigue resistance, and toughness (Bilbao et al., 2023; Dong et al., 2020; Duda et al., 2021). The final mechanical properties of 42CrMo4 steel are governed by the combined effects of chemical composition, heat-treatment conditions, and prior thermomechanical history (Mudda et al., 2025). In practice, alloy steel design frequently depends on operators' experience, empirical formulae, and trial-and-error adjustments to elemental compositions, followed by mechanical processing. These techniques demand significant time and resources and present challenges in achieving the appropriate equilibrium of properties.

42CrMo4 steel is a medium-carbon chromium-molybdenum alloy steel in which elements such as chromium, molybdenum, and nickel contribute to improved hardenability, strength, and toughness. These characteristics make the alloy suitable for demanding engineering applications, particularly in automotive and heavy mechanical components. Adding microalloying elements, such as titanium or niobium, refines the grain size, while residual elements, including copper, phosphorus, and sulphur, affect surface quality and ease of machining. Even minor adjustments to the composition alter the material's transformation behaviour, the way carbides form, and the overall microstructure; ultimately, they influence strength, ductility, and surface finish after machining (Gladman, 1997; Honeycombe & Bhadeshia, 2006; Totten, 2006; Trent & Wright, 2000). A clear understanding of these interactions is essential for the systematic design and optimisation of alloy steels.

The complex relationships among composition, processing, and properties make it challenging to develop a standard model for these steels (Yang et al., 2022). Therefore, advanced emerging techniques like machine learning show great promise. This approach improves understanding of the relationships between alloy composition, processing conditions, and resulting properties. This helps develop new materials faster and achieve specific properties more easily, making the process more efficient and successful (Colla et al., 2023). Several machine learning algorithms have been applied in materials engineering to analyse complex materials and datasets. These techniques include powerful tools such as support vector machines, random forests, and artificial neural networks. They are highly reliable at predicting key material properties, such as hardness, toughness, and tensile strength (Yarasu & Podgornik, 2025).

Data-driven approaches use historical input datasets to create models. These methods help identify relationships between compositional inputs and the resulting mechanical properties. Although this process can sometimes be challenging with traditional methods, the effort is justified by the benefits of the employed methodologies. These approaches are more efficient for designing and developing alloys and optimising their targeted properties (Lee et al., 2021). Data-driven machine learning approaches have emerged as effective tools for analysing complex relationships in steel alloy and other material systems. They provide information on the complex, non-linear relationships between composition and material properties, enabling a reduction in the number of experiments (Guo et al., 2020).

In metallic alloys, machine learning can be a valuable tool for predicting mechanical properties, process zones, and microstructural features as functions of chemical and material-processing parameters. Models based on compositional-material property predictions offer robust insights. Furthermore, it helps reduce costs by optimising the use of expensive alloying elements while achieving target properties. Machine learning models have demonstrated strong capability in predicting the mechanical properties of steel alloys using compositional descriptors (Cheng et al., 2024; Wang et al., 2019). They simplify achieving required properties by speeding up the alloy design process.

Although many studies have applied machine learning to steels, most focus on predicting bulk mechanical properties such as strength or hardness (Ahmed et al., 2025; Huang et al., 2024). Machining-related responses, particularly surface roughness (R_a), are rarely included in these predictive models (D'Urso et al., 2023; Huang et al., 2024; Kaur et al., 2025; Ling et al., 2017; Wang et al., 2024; Zhang et al., 2020). However, machining behaviour is a critical factor in manufacturing performance and product quality. The present study addresses this research gap by developing a composition-based machine learning framework for 42CrMo4 (AISI 4140) steel that predicts both strength-related properties and R_a after machining. A Gradient Boosting Regressor (GBR) model was employed to evaluate these parameters.

Materials and Methods

Material History and Chemical Composition

42CrMo4 (AISI 4140) is a quenched-and-tempered low-alloy steel highly prized for its capacity to meet necessary application property requirements. It belongs to the chromium-molybdenum steel group and features a medium-carbon level, with hardness and toughness improved by heat treatment. It is often used in shafts, gears, connecting rods, axles, and bolts, where dependable mechanical performance is crucial (Mazini et al., 2022). The chemical composition is a critical factor controlling the mechanical performance and long-term reliability of the component (Xiong et al., 2020). Elements such as carbon, chromium, molybdenum, and nickel influence hardenability, martensite formation, and tempering characteristics. Manganese, silicon, phosphorus, and sulphur play important roles in determining secondary qualities, such as how easily it machines and its surface finish.

The mechanical properties of this steel depend on its chemical composition. Elements such as carbon, chromium, molybdenum, and nickel influence hardenability, martensite formation, and tempering characteristics. Manganese, silicon, phosphorus, and sulphur play important roles in determining the secondary qualities of steel, such as how easily it machines and its surface finish. At their respective levels can significantly impact strength and smoothness, especially in mechanised settings where many heats are melted and cast to meet customers' requirements. The present study examined the chemical composition of 42CrMo4 (AISI 4140) steel after casting, based on data from 1,000 samples. The compositions of all these samples are listed as weight percent. Additionally, each sample was tested for mechanical properties following the standard Universal Testing Method (UTM). The data replaced the model's thorough review for errors, and entries with absent or uneven values in accuracy. Following this process, nine elements were selected for their known influence on strength, toughness, and surface finish. Carbon, chromium, molybdenum, and nickel are the main alloying elements and strongly influence hardenability and strength. Titanium, copper, phosphorus, silicon, and manganese are present in minor amounts but still exert an effect on grain size, chemical segregation, and machining response. These nine elements collectively provide a clear and appropriate representation in controlling the mechanical properties of 42CrMo4 steel. Table 1 presents the nine chemical elements used for inputs. All values are given in weight percent (%) and correspond to the typical composition range of 42CrMo4 (AISI 4140) steel.

Mechanical Property Measurements

The mechanical properties used in this study were taken from standard tests performed on 42CrMo4 (AISI 4140) steel samples. A few mechanical properties were selected as they represent the most critical performance requirements for this grade: ultimate tensile strength (UTS), yield strength (YS), 0.2% proof stress, and R_a. The principles justify the material's ability to carry a load and resist permanent deformation, and they depend on the microstructure formed during heat treatment.

R_a provides important insights into machining performance and the surface quality of the components we prepare. To understand the tensile properties, we analysed stress–strain curves obtained with a universal testing machine. We carefully measured R_a using a calibrated contact-type profilometer to ensure accuracy. The test matched each mechanical property to its corresponding chemical composition, helping to build a reliable supervised dataset. Table 2 highlights the four fundamental

Table 1. 42CrMo4 (AISI 4140) Steel Shows Chemical Compositions (wt%) and Their Range Used for ML Modelling.

Element	Symbol	Typical Range (wt%)	Role in Steel
Carbon	C	0.38–0.45	Strengthening element, increases hardness and hardenability
Silicon	Si	0.10–0.40	Supports deoxidation, influences ferrite carbide structure
Phosphorus	P	≤0.025	Residual element affects segregation and machinability
Manganese	Mn	0.60–0.90	Improves hardenability and toughness
Copper	Cu	≤0.30	Residual and minor effect on surface quality
Chromium	Cr	0.90–1.20	Enhances hardenability, forms strengthening carbides
Nickel	Ni	≤0.40	Improves hardiness and impact strength
Molybdenum	Mo	0.15–0.30	Improves tempering resistance and strength retention
Titanium	Ti	≤0.050	Forms fine precipitates; helps grain refinement

Source: Honeycombe & Bhadeshia (2006); Totten (2006).

Table 2. The Mechanical Properties and Their Value Range of 42CrMo4 (AISI 4140) Steel,

Mechanical Property	Symbol	Range (Typical)	Unit
Ultimate tensile strength	UTS	900–1,100	MPa
Yield strength	YS	700–900	MPa
0.2% proof stress	0.2% PS	650–850	MPa
Surface roughness	Ra	4.5–8.0	μm

Source: Mazini et al. (2022); Mudda et al. (2025); Bibao et al. (2023).

mechanical properties used as outputs in our models. The ranges listed below reflect typical values for quenched-and-tempered 42CrMo4 (AISI 4140) steel.

Data Cleaning and Preparation

The data was carefully gathered to ensure everything was clear and consistent for the model. First, we reviewed the missing values in the chemical composition and mechanical property columns. Any samples lacking complete information were politely removed, and interpolation was used only when necessary. During data preprocessing, outliers were identified as records with extreme compositional values that deviated significantly from the dataset's typical range. We looked at outliers- values outside 1.5 times the interquartile range- and removed those resulting from testing issues. These anomalous entries may arise from measurement inconsistencies or data reporting errors and can negatively influence machine learning model training. Such records were removed prior to feature selection and model development to improve dataset consistency.

After cleaning, we standardised the feature labels, merged duplicates, and displayed all compositions as weight percentages for a stronger, additional uniform view. The heatmap was created to visualise relationships between mechanical properties and chemical elements, providing insight.

Reasoning Behind the Selection of the Nine Chemical Features

The nine chemical elements used in this study were carefully selected because they hold a key role in affecting the behaviour of 42CrMo4 steel. Carbon is the primary element that enhances strength and promotes martensite formation during hardening. Chromium encourages hardenability and forms carbides. Molybdenum helps prevent softening and increases toughness. Nickel enhances toughness and enables greater hardening. Titanium forms fine particles, resulting in a finer grain size. Manganese also improves hardenability and surface characteristics. Silicon is vital for balancing ferrite and carbides and for improving the surface finish. Phosphorus, even in small amounts, affects machinability and roughness. Copper provides a small amount of strengthening and affects the steel's surface.

Dataset Summary

After cleaning and checking the data, a final dataset comprising 1,000 entries was prepared for modelling. It contains data on both its chemical composition and corresponding mechanical properties. The dataset includes nine chemical elements as inputs for capturing the strengthening mechanisms and surface-related effects in 42CrMo4 steel. And four mechanical properties as output variables, UTS, YS, 0.2% proof stress, and R_a. Since each sample possesses corresponding composition and property data. The dataset is appropriate for supervised machine learning. This cleaned and organised data was used in the modelling work described in the next section.

Machine Learning Regression Models

In this research, we designed a machine learning framework to generate reliable demonstrations that work effectively to predict the mechanical properties of 42CrMo4 steel from its chemical composition. The model uses nine compositional variables as input features and predicts four mechanical properties as output variables. This way, forecasting capabilities for each property are improved with confidence. The modelling process was simple and followed supervised-learning practices, making the methodology inclusive and manageable (Wei et al., 2021). In this study, four independent regression models were developed, each targeting a single output variable such as UTS, YS, 0.2% proof stress, and R_a. A multi-output regression framework was not adopted because these properties arise from different metallurgical compositional mechanisms and may respond differently to compositional variations. Training individual models enables the algorithm to better capture property-specific relationships between alloying elements and mechanical responses.

We chose the GBR algorithm as our main model because it performs well on small and medium-sized datasets. It is also highly effective at capturing complex associations among various elements and their mechanical properties, so we can trust its reliability. GBR constructs an ensemble of decision trees, where each tree iteratively reduces the prediction error of the previous model. This makes the method suitable for material datasets containing complex and non-linear relationships (Zhang et al., 2022).

Model validation was performed using a combination of train-test splitting of the dataset and five-fold cross-validation. To train and test, the dataset was split into training and test sets. This approach helps ensure a smoother and more manageable process. Around 80% of the data was utilised for training and model development, including hyperparameter optimisation, while the remaining 20% was reserved to assess the model's performance on new, unseen samples. To ensure our assessment is reliable and reasonable, we used five-fold cross-validation. This means we split the training set into five parts, trained the model on four parts, and tested it on the fifth. We repeated this process five times, each with a different part, and averaged the results to gain a clearer understanding of the model in action. This method helps prevent overfitting and provides a more reliable estimation of predictive accuracy and a sense of how well the model truly performs (Mohanty et al., 2022).

The model's hyperparameters were carefully fine-tuned through a comprehensive grid search, exploring combinations of settings such as the number of trees, learning rate, and maximum depth to identify the optimal configuration. The combination that achieved the highest cross-validation score was chosen for the final model. Once the best settings were identified, the models were retrained on the entire dataset for training (Pathan et al., 2019). Table 3 illustrates the hyperparameter search ranges and selected values for the GBR models.

The performance of each model was evaluated using standard regression metrics, including the coefficient of determination (R^2), mean absolute error (MAE), and root mean squared error (RMSE). This provides an easy way to see how accurately the predicted values match the actual data. Overall, the models performed quite well across four properties, particularly excelling at predicting 0.2% proof stress and tensile strength. While R_a was also predicted with good accuracy, it showed slightly less accuracy. This makes sense because roughness depends more on machining and processing conditions than simply composition (Ammar, 2021; Sivakumar et al., 2022).

After the training, we used several plots and straightforward tools to better understand how our model behaves. The feature-importance charts highlighted which features had the biggest impact on the predictions. Actual versus predicted plots show how closely the measured values align with the projections, helping

Table 3. Hyperparameter Search Ranges and Selected Values for the Gradient Boosting Regressor Models.

Hyperparameter	Range Tested in Grid Search	Final Selected Value	Description
N estimators	100–1000	500	Number of boosting trees used in the ensemble
Learning rate	0.01–0.2	0.05	Step size controlling the contribution of each tree
Maximum depth	2–6	3	Maximum depth of individual regression trees
Minimum samples split	2–10	4	Minimum samples required to split an internal node
Minimum samples leaf	1–5	2	Minimum samples required at a leaf node
Subsample	0.7–1.0	0.8	Fraction of training samples used for each tree
Maximum features	Options: Auto, sqrt, log2	sqrt	Number of features/options considered when looking for the best split and reducing overfitting

Source: Pathan et al. (2019); Mohanty et al. (2022).

assess the level of agreement. This analysis was conducted to explore how different elemental compositions affect the model's output (Javed et al., 2024).

Results and Discussion

The machine learning models were trained on treated data, with nine chemical elements as inputs and four mechanical properties as outputs. We developed individual models for each property: UTS, YS, 0.2% proof stress, and R_a. To evaluate the effectiveness of each model, we used R^2, MAE, and RMSE. These measures provided a clear idea of how closely the predictions matched the experimental values (Tiwari et al., 2025). Table 4 presents the performance metrics (R^2, MAE, RMSE) derived from the machine learning algorithm utilised for predicting mechanical properties.

The models validated excellent performance for the strength-related properties. The 0.2% proof stress prediction had the highest accuracy among the four outputs. This result is expected because proof stress depends directly on the combined effects of carbon, chromium, molybdenum, and nickel, all of which are in the dataset. UTS and YS also showed good prediction accuracy, with most values falling close to the measured results. The prediction accuracy for R_a was slightly lower than that of the strength-related properties. This behaviour is expected because R_a is influenced not only by the alloy composition but also by machining parameters such as cutting speed, feed rate, tool geometry, lubrication, and tool wear. In the present study, machining conditions were kept constant for all samples during testing. Therefore, the machine learning model primarily captures the influence of chemical composition on surface finish. Nevertheless, the absence of machining parameters in the dataset represents an inherent limitation of composition-based modelling for predicting machining responses. Even with these limitations, the model still captured meaningful trends. Elements such as phosphorus, manganese, and silicon exerted a noticeable influence on roughness values, consistent with common metallurgical knowledge of segregation and surface behaviour (Muhammad et al., 2022).

Figure 1 presents helpful graphs highlighting key features of materials. These visuals clarify which factors matter most. The four plots beautifully illustrate the influence of chemical composition on the mechanical properties of 42CrMo4 steel. The model carefully evaluates the influence of elements associated with each property. For a 0.2% proof stress, Ni, Ti, and Si stand out as the most influential. Nickel enhances the strength and toughness of the steel, making it more durable. Titanium strengthens the steel by forming fine precipitates. When considering YS, Mn, C, and Ni are the key players. Carbon primarily boosts strength, with manganese helping to improve hardenability. Nickel also contributes by helping the material maintain its strength as it begins to yield. For UTS, Ti, Mo, and Cu are the most important. Titanium and molybdenum help prevent softening during heat treatment, while copper provides a slight strengthening effect (Li et al., 2022).

Various factors affect how steel responds under high loads. For R_a, manganese (Mn), nickel (Ni), and phosphorus (P) are particularly important. Manganese

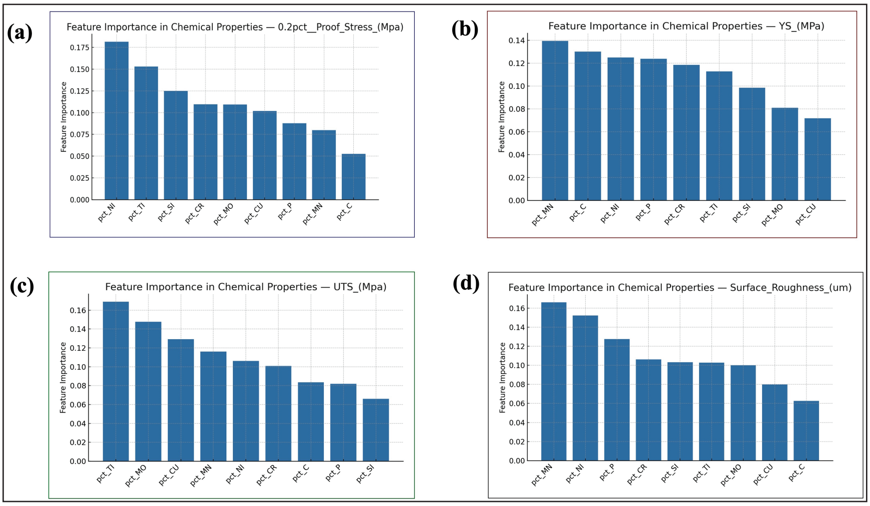

Figure 1. Feature-importance Plots for the Prediction of (a) 0.2% Proof Stress, (b) Yield Strength, (c) Ultimate Tensile Strength, and (d) Surface Roughness of 42CrMo4 Steel. Each of the Nine Elements Impacts Machinability and Strength in Distinct Ways, as Shown by Their Rankings.

affects how the material segregates and the carbide patterns it forms, while phosphorus influences chip formation and the ease with which the material can be machined. Nickel helps stabilise the microstructure, enhancing the material's overall reliability. This is how steel behaves when cut or shaped.

Table 4. Model Performance for Predicting Mechanical Properties of 42CrMo4 Steel Using Chemical Composition.

Property	R^2 (Mean ± Std)	MAE	RMSE	Remarks
UTS (MPa)	0.69 ± 0.04	8.3 MPa	11.5 MPa	Strong correlation and reliability
YS (MPa)	0.67 ± 0.05	7.8 MPa	10.9 MPa	Stable performance
0.2% proof stress (MPa)	0.73 ± 0.03	6.9 MPa	9.7 MPa	Highest model accuracy
Surface roughness (μm)	0.64 ± 0.06	0.28 μm	0.36 μm	Moderate fit, process-dependent

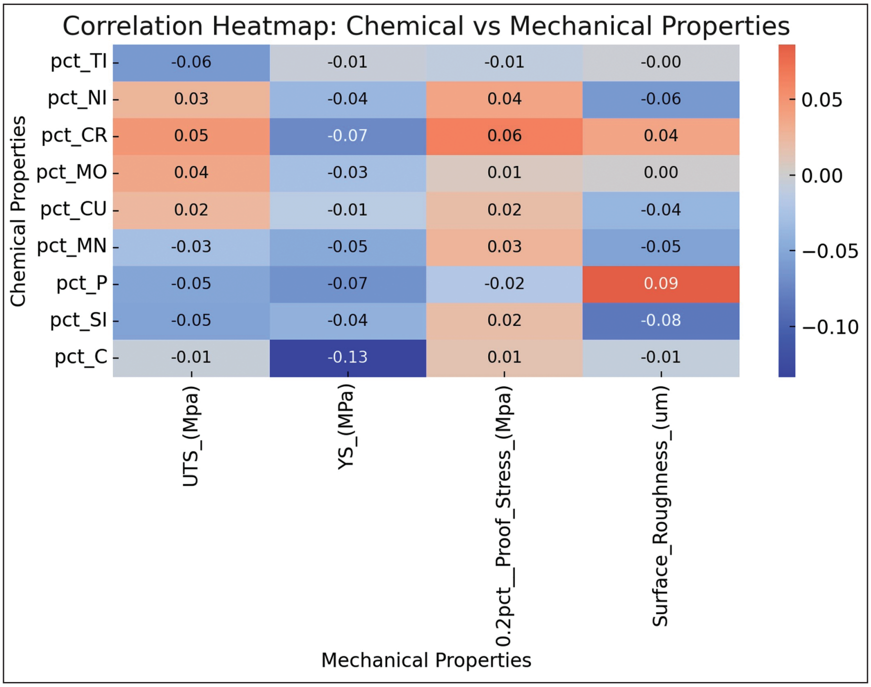

Figure 2. Correlation Heatmap Showing the Linear Relationships Between the Nine Chemical Elements and the Four Mechanical Properties of 42CrMo4 Steel. Most Values Are Low, Indicating Weak Direct Correlations, Which Is Expected for a Multi-element Alloy System. Small Positive and Negative Trends Are Visible for Certain Elements, Such as C, P, and Cr, but None Dominate the Overall Behaviour.

Elements such as chromium and molybdenum, along with carbon, are essential for predicting strength because they control hardenability, martensite formation, and resistance to tempering. Nickel also boosts toughness and supports the steel's strength. Relating to R_a, phosphorus and manganese affect how the material microsegregates and how carbides are distributed, both of which influence cutting performance (Wei et al., 2021).

Figure 2 shows a heatmap of the relationships between composition and the four mechanical properties of 42CrMo4 steel. Most correlations are quite low, which makes sense because these properties are shaped by many different aspects, not just their composition. Carbon shows a slight negative correlation with YS. Phosphorus shows a slight positive association with R_a, consistent with its known effect on machinability. Chromium shows a weak positive trend with proof stress and R_a. The remaining elements do not affect all properties. The heatmap provides a quick overview of these small trends, and a strong linear relationship exists before modelling (Leni et al., 2023).

Figure 3 compares the bar charts showing the effects of chemical elements on all four mechanical properties of 42CrMo4 steel. The bars show the influence each component has on the prediction models. The plot makes it clear that no individual element dominates all properties. Titanium, nickel, and chromium show strong contributions within most strength properties. Molybdenum and copper also play steady roles, mainly in UTS and proof stress. Manganese, phosphorus, and silicon have a larger effect on R_a than on strength. Carbon has a modest influence, but its impact differs within properties. They reflect the behaviour expected of alloyed steels, in

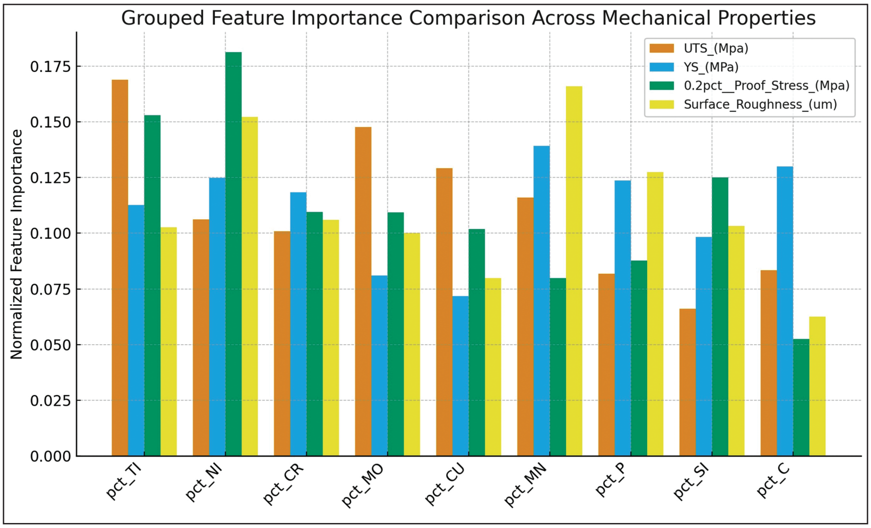

Figure 3. Grouped Feature-importance Comparison for the Prediction of Ultimate Tensile Strength, Yield Strength, 0.2% Proof Stress, and Surface Roughness of 42CrMo4 Steel. The Plot Shows the Contributions of Different Elements to the Four Properties, Highlighting Those That Influence Strength (Ti, Ni, Cr, Mo) and Those That Have a More Substantial Effect on Machinability (Mn, P, Si).

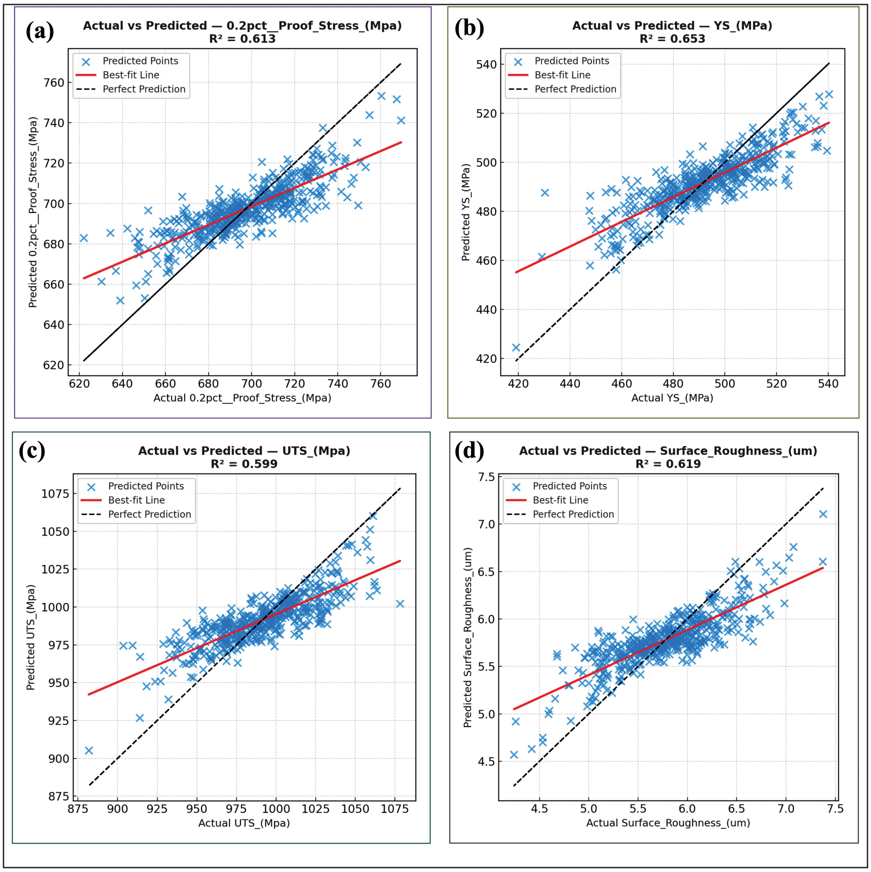

Figure 4. The Plots for (a) 0.2% Proof Stress, (b) Yield Strength, (c) Ultimate Tensile Strength, and (d) Surface Roughness of 42CrMo4 Steel Show the Links Between Actual and Predicted. Each Plot Includes Model Predictions, a Best-fit Line, and a Perfect-prediction Reference Line. The Trends Show Good Agreement for Proof Stress and Yield Strength, with Moderate Fits for UTS and Surface Roughness.

which strengthening and machinability result from several elements acting together rather than from a single element (Romanov & Hawk, 2019).

Figure 4 compares the model-predicted values with the measured values for each mechanical property of 42CrMo4 steel. Each plot includes the predicted points, a best-fit regression line, and a perfect-prediction line. The model's performance will improve as the measured points approach the perfect-prediction line. In (a), 0.2% proof stress, most points fall close to the perfect-prediction line. The R^2 value is the highest among the four properties, indicating that the model predicts this property more effectively than the others. In (b), the YS range is wider and exhibits an upward trend. Numerous points are close to the ideal prediction line. This demonstrates consistently steady model behaviour. In (c), UTS, the scatter is larger. The model still follows the main trend, but the predictions show more variation. UTS is affected by several factors other than chemistry, which explains the weaker fit. In (d) R_a, the points show a noticeable upward trend, but there is greater scatter, especially at higher roughness values. R_a is influenced by the alloy composition and machining parameters, so a moderate fit is usually expected (Peng et al., 2020). Overall, all four plots show the material's behavioural properties.

Proof stress and YS are predicted with high accuracy, whereas UTS and R_a have moderate accuracy. They highlight the intrinsic properties of the material and its chemical composition, which makes these results quite promising (Tan et al., 2023).

Overall, these findings suggest that analysing the composition of 42CrMo4 steel alone can give us trustworthy insights into its strength properties. We can also model R_a quite effectively, and by including machining parameters, we can achieve even better results. This shows that the machine learning approach is not just accurate; it also aligns with metallurgical principles. It is a really helpful tool that can support composition control, process planning, and early property predictions for different applications. It advances assurance in the processes and makes everything more dependable.

Conclusions

This study demonstrates that the mechanical properties of 42CrMo4 (AISI 4140) steel can be accurately predicted solely based on composition. The data, containing 1,000 heats and nine essential alloying and residual elements, enabled the Gradient Boosting algorithm to establish reliable correlations between composition and strength-related characteristics. The models showed strong correlations for 0.2% proof stress, YS, and tensile strength, with proof stress achieving the highest accuracy. R_a predictions were moderate, which is understandable because machining conditions—though influential—were not included in the dataset. It should be noted that R_a is also affected by machining parameters, including cutting speed, feed rate, and tool condition. Since these parameters were not included in the present dataset, the model predicts roughness mainly from compositional effects. Future work should integrate machining parameters and microstructural descriptors to further improve the predictive capability of the model.

The features and their correlation patterns aligned well with metallurgical principles. Elements such as Ti, Ni, Cr, and Mo significantly impacted strength, whereas Mn, P, and Si mainly affected R_a. These findings reflect known phenomena like strengthening and segregation behaviours in low-alloy steels. The comparison of actual versus predicted values further validated that the model captured the main behavioural trends, especially for strength properties.

Overall, this work demonstrates the machine learning's supportive role in alloy composition management, heat-treatment scheduling, and initial property forecasting in steel manufacturing. Such methods can notably reduce the number of mechanical tests required and accelerate feedback during alloy development. Future enhancements include processing parameters, microstructural details, and machining conditions to improve R_a predictions and to generate a complete digital platform for steel design and production.

Authors' Contributions

All authors contributed to this work.

Data Availability

The data that support the findings of this study are available from the corresponding author upon reasonable request.

Declaration of Conflicting Interests

The authors declared no potential conflicts of interest with respect to the research, authorship and/or publication of this article.

Funding

The authors disclosed receipt of the following financial support for the research, authorship and/or publication of this article: Financial assistance from the Anusandhan National Research Foundation (ANRF) under the Partnerships for Accelerated Innovation and Research (PAIR) programme, in collaboration with IIT (ISM) Dhanbad, for the project 'Development of Innovative and Cutting-Edge Indigenous Technologies for Critical Minerals Exploration and Smart/Sustainable Mining' (Sanction Order No. ANRF/PAIR/2025/000027/PAIR-B) is gratefully acknowledged.

References

Ahmed, R., Kumar, V., Faisal, N. H., Al-Marri, M. J., & Davies, S. (2025). Influence of alloy composition on the tribomechanical properties of 50% blend of CoCrWMoCFeNiSiMn (Stellite 1) and CoCrMoCFeNiSiMn (Stellite 21) alloys. *Journal of Materials Engineering and Performance*. https://doi.org/10.1007/s11665-025-11034-7

Ammar, M. H. A. (2021). *Advanced digital twins for condition monitoring, diagnosis, and predictive remaining life using artificial intelligence (Doctoral dissertation, Brunel University London).* Brunel University Research Archive. https://bura.brunel.ac.uk/bitstream/2438/28074/1/FulltextThesis.pdf

Bilbao, O., Loizaga, I., Alonso, J., Girot, F., & Torregaray, A. (2023). 42CrMo4 steel flow behavior characterization for high temperature closed dies hot forging in automotive components applications. *Heliyon*, *9*(11), e22256. https://doi.org/10.1016/j.heliyon.2023.e22256

Cheng, H., He, Z., Ge, M., Che, L., Zheng, K., Si, T., & Zhao, F. (2024). Composition design and optimization of Fe–C–Mn–Al steel based on machine learning. *Physical Chemistry Chemical Physics*, *26*(10), 8219. https://doi.org/10.1039/d3cp05453e

Colla, V., Vannucci, M., Matino, I., & Valentini, R. (2023). A deep learning-based approach to the estimation of Jominy profile of medium-carbon quench hardenable steels. *Steel Research International*, *95*(2). https://doi.org/10.1002/srin.202300374

Dong, J., Pei, W., Ji, H., Long, H., Fu, X., & Duan, H. (2020). Fatigue crack propagation experiment and numerical simulation of 42CrMo steel. *Proceedings of the Institution of Mechanical Engineers*, *Part C: Journal of Mechanical Engineering Science*, *234*(14), 2852. https://doi.org/10.1177/0954406220910458

D'Urso, D., Chiacchio, F., Cavalieri, S., Gambadoro, S., & Khodayee, S. M. (2023). Predictive maintenance of standalone steel industrial components powered by a dynamic reliability digital twin model with artificial intelligence. *Reliability Engineering & System Safety*, *243*, 109859. https://doi.org/10.1016/j.ress.2023.109859

Duda, M., Rozumek, D., Lesiuk, G., Smolnicki, M., Babiarczuk, B., & Warycha, J. (2021). Fatigue crack growth under mixed-mode I + II and I + III in heat treated 42CrMo4 steel. *International Journal of Fracture*, *234*, 235. https://doi.org/10.1007/s10704-021-00585-0

Gladman, T. (1997). *The physical metallurgy of microalloyed steels*. The Institute of Materials.

Guo, K., Yang, Z., Yu, C., & Buehler, M. J. (2020). Artificial intelligence and machine learning in design of mechanical materials. *Materials Horizons*, *8*(4), 1153. https://doi.org/10.1039/d0mh01451f

Honeycombe, R. W. K., & Bhadeshia, H. K. D. H. (2006). *Steels: Microstructure and properties* (3rd ed.). Elsevier Butterworth-Heinemann.

Huang, J., Ando, D., & Sutou, Y. (2024). Heat-resistant aluminum alloy design using explainable machine learning. *Materials & Design*, *243*, 113057. https://doi.org/10.1016/j.matdes.2024.113057

Javed, M. F., Fawad, M., Lodhi, R. H., Najeh, T., & Gamil, Y. (2024). Forecasting the strength of preplaced aggregate concrete using interpretable machine learning approaches. *Scientific Reports*, *14*(1), 8381. https://doi.org/10.1038/s41598-024-57896-0

Kaur, R., Kumar, R., & Aggarwal, H. (2025). Systematic review of artificial intelligence, machine learning, and deep learning in machining operations: Advancements, challenges, and future directions. *Archives of Computational Methods in Engineering*, *32*, 4983–5036. https://doi.org/10.1007/s11831-025-10290-z

Lee, J.-W., Park, C., Lee, B. D., Park, J., Goo, N. H., & Sohn, K. (2021). A machine-learning-based alloy design platform that enables both forward and inverse predictions for thermo-mechanically controlled processed (TMCP) steel alloys. *Scientific Reports*, *11*(1). https://doi.org/10.1038/s41598-021-90237-z

Leni, D., Earnestly, F., Sumiati, R., Adriansyah, A., & Kusuma, Y. P. (2023). Evaluasi sifat mekanik baja paduan rendah berdasarkan komposisi kimia dan suhu perlakuan panas menggunakan teknik exploratory data analysis (EDA). *Dinamika Teknik Mesin*, *13*(1), 74. https://doi.org/10.29303/dtm.v13i1.624

Li, Z., Wang, Z., Wang, Z., Qin, Z., Liu, F., Tan, L., Jin, X., Fan, X., & Huang, L. (2022). Quantifying solid solution strengthening in nickel-based superalloys via high-throughput experiment and machine learning. *Computer Modeling in Engineering & Sciences*, *135*(2), 1521. https://doi.org/10.32604/cmes.2022.021639

Ling, J., Hutchinson, M., Antono, E., DeCost, B., Holm, E. A., & Meredig, B. (2017). Building data-driven models with microstructural images: Generalization and interpretability. *Materials Discovery*, *10*, 19–27. https://doi.org/10.1016/j.md.2018.03.002

Mazini, J. P., Filho, A. I., Ávila, B. M. R., da Silva, R. V., & de Oliveira, P. G. B. (2022). Microstructure and mechanical properties of microalloyed steels containing molybdenum. *Materials Research*, 25. https://doi.org/10.1590/1980-5373-mr-2021-0608

Mohanty, T., Chandran, K. S. R., & Sparks, T. D. (2022). Machine learning guided optimal composition selection of niobium alloys for high temperature applications. *ChemRxiv*. https://doi.org/10.26434/chemrxiv-2022-1d9k0

Mudda, S., Hegde, A., Sharma, S., Gurumurthy, B. M., Shettar, M., & Shankar, M. C. G. (2025). Effect of various heat treatment methods and optimization of their parameters on mechanical properties of AISI 4140 steel. *Scientific Reports*, *15*(1), 31854. https://doi.org/10.1038/s41598-025-17299-1

Muhammad, W., Kang, J., Ibragimova, O., & Inal, K. (2022). Experimental investigation and development of a deep learning framework to predict process-induced surface roughness in additively manufactured aluminum alloys. *Welding in the World*, *67*(4), 897. https://doi.org/10.1007/s40194-022-01445-8

Pathan, M. V., Ponnusami, S. A., Pathan, J., Pitisongsawat, R., Erice, B., Petrinic, N., & Tagarielli, V. L. (2019). Predictions of the mechanical properties of unidirectional fibre composites by supervised machine learning. *Scientific Reports*, *9*(1). https://doi.org/10.1038/s41598-019-50144-w

Peng, J., Yamamoto, Y., Hawk, J. A., Lara-Curzio, E., & Shin, D. (2020). Coupling physics in machine learning to predict properties of high-temperature alloys. *npj Computational Materials*, *6*(1). https://doi.org/10.1038/s41524-020-00407-2

Romanov, V., & Hawk, J. A. (2019). *Data analytics for designing Fe-9Cr steels*. U.S. Department of Energy Office of Scientific and Technical Information. https://www.osti.gov/biblio/1569972

Sivakumar, E. R., Krishna, R., Senthilkumar, P., & Çolak, İ. (2022). Influence of mechanical properties of coating and substrate on wear performance of HDLC and TiN-coated AISI 5140 alloy steel. *Proceedings of the Institution of Mechanical Engineers, Part E: Journal of Process Mechanical Engineering*. https://doi.org/10.1177/09544089221132434

Tan, R. R., Li, Z., Zhao, S., & Birbilis, N. (2023). A primitive machine learning tool for the mechanical property prediction of multiple principal element alloys. *arXiv*. https://doi.org/10.48550/arxiv.2308.07649

Tiwari, S., Ahn, H. S., Reddy, M. H., Park, N., & Reddy, N. S. (2025). Mechanical property prediction of industrial low-carbon hot-rolled steels using artificial neural networks. *Materials*, *18*(13), 2966. https://doi.org/10.3390/ma18132966

Totten, G. E. (2006). *Steel heat treatment: Metallurgy and technologies*. CRC Press.

Trent, E. M., & Wright, P. K. (2000). *Metal cutting* (4th ed.). Butterworth-Heinemann.

Wang, C., Shen, C., Cui, Q., Zhang, C., & Xu, W. (2019). Tensile property prediction by feature engineering guided machine learning in reduced activation ferritic/martensitic steels. *Journal of Nuclear Materials*, *529*, 151823. https://doi.org/10.1016/j.jnucmat.2019.151823

Wang, K., Gupta, V., Lee, C. S., Mao, Y., Kilic, M. N. T., Li, Y., Huang, Z., Liao, W.-K., Choudhary, A., & Agrawal, A. (2024). XElemNet: Towards explainable AI for deep neural networks in materials science. *Scientific Reports*, *14*, 25178. https://doi.org/10.1038/s41598-024-76535-2

Wei, Q., Xiong, J., Sun, S., & Zhang, T. (2021). Multi-objective machine learning of four mechanical properties of steels. *Scientia Sinica Technologica*, *51*(6), 722. https://doi.org/10.1360/sst-2020-0475

Xiong, J., Zhang, T., & Shi, S. (2020). Machine learning of mechanical properties of steels. *Science China Technological Sciences*, *63*(7), 1247. https://doi.org/10.1007/s11431-020-1599-5

Yang, X., El-Fallah, G. M. A. M., Tao, Q., Fu, J., Leng, C., Shepherd, J., & Dong, H. (2022). Dimensionality reduction for machine learning using statistical methods: A case study on predicting mechanical properties of steels. *Materials Today Communications*, *34*, 105162. https://doi.org/10.1016/j.mtcomm.2022.105162

Yarasu, V., & Podgornik, B. (2025). An optimized machine-learning tool to predict heat treatment response of hot-work tool steels. *Results in Engineering*, *26*, 105260. https://doi.org/10.1016/j.rineng.2025.105260

Zhang, C., Gu, X., Bhandari, U., Lei, J., Guo, S., Kourouma, M., Karoui, A., & Yang, S. (2022). Machine learning prediction of the mechanical properties of refractory multicomponent alloys based on a dataset of phase and first principles simulation. *Frontiers in Metals and Alloys, 1*. https://doi.org/10.3389/ftmal.2022.1036656

Zhang, Y., Sun, C., Gao, L., Yue, Z., Shabbir, S., Xu, W., Wu, M., & Yu, J. (2020). Determination of minor metal elements in steel using laser-induced breakdown spectroscopy combined with machine learning algorithms. *Spectrochimica Acta Part B: Atomic Spectroscopy*, *166*, 105802. https://doi.org/10.1016/j.sab.2020.105802

Article

Study of Effect of Secondary Cooling on Titanium Nitride Precipitation During Continuous Casting of High-strength Steel Slab

Sustainable Manufacturing and
Foundry Practices
1(1) 80–87, 2026
© The Author(s) 2026
DOI: 10.1177/IIF.261439608
Journal.indianfoundry.org
THE INSTITUTE OF INDIAN FOUNDRYMEN

Ajay Kumar Pradhan[1], Pabitra Palai[1], Pramod Yadav[1] and M Manjunathan[1]

Abstract

The special type of advanced high-strength steels (AHSS) based on nano precipitation strengthening mechanism was studied in the current work. It is a typical molybdenum and titanium based micro-alloyed steel under AHSS offers up to 800 Mpa tensile strength and have preferred application in the automobile industry owing to its impact on overall vehicle weight reduction with improved safety and fuel efficiency, The focus of study in this grade were failure due to cracking during forming on account of coarse Titanium Nitride (TiN) precipitate in such high-strength level above 800 Mpa tensile strength. The main challenges in this grade are chemical composition and casting parameters control, which have a direct influence on the microstructure and final properties that are attributed to precipitate size. The study has been done for the precipitation of TiN in high-strength steel by varying secondary cooling during slab casting. The model enabled the prediction of the expected inclusion size of TiN of a specific HS800 heats before rolling to enable slab decision. The main goal of this work was to obtain the dependence relationship between inclusion size and slab solidification and cooling rate during continuous casting.

Keywords

Chemical composition, high-strength steel, precipitation strengthening, continuous slab casting

---

[1]Steel Making Shop, TATA Steel Limited, Jajpur, Odisha, India

Corresponding author:
Ajay Kumar Pradhan, Steel Making Shop, TATA Steel Limited, Kalinganagar, Jajpur, Odisha 755026, India.
E-mail: ajay.pradhan3@tatasteel.com

Introduction

The growing demand from the automotive sector for lightweight vehicles, aimed at improving fuel efficiency and reducing greenhouse gas emissions, has driven steel manufacturers to develop advanced high-strength steels (AHSS). In response to this need, Steel makers have initiated the development of a high-strength steel grade with a minimum tensile strength of 800 MPa. The cleanliness of this steel is critical for determining product acceptance in automotive applications. This steel, along with other grades used in automotive underbody components such as suspension systems, cross members, and chassis, is produced through the conventional BOF–slab casting–hot rolling route. The HS800 grade is a micro-alloyed steel containing elements such as Nb, Ti, and Mo, along with an elevated manganese content as mentioned in Table 1. The grade initially reported a brittle failure at the customer end, specifically at the bent area of the components. It appears the cracks likely started near a hole in this bent region (as shown in Figure 1), potentially due to stress concentration exacerbated by a shorter distance between holes on the cracked side compared to crack-free areas. Microscopic examination revealed a notable presence of Titanium Nitride (TiN) inclusions, approximately 13–14 µm in size, both where cracks occurred and where the material remained intact. These inclusions are suspected to have played a role in the crack's propagation once it initiated from the stress point around the hole. The chemistry of the HS800 grade is attached.

Que et al. (2023) examined the distribution of TiN inclusions in the cross-section of a titanium micro-alloyed steel slab and found that the number density of these inclusions sharply decreases from the surface to the center, while their average size increases in the same direction. Higher cooling rates lead to greater undercooling, which results in finer TiN precipitation. Micrographs indicated that TiN inclusions are mainly cuboidal in shape with well-defined edges, as shown in Figure 2.

Yang et al. (2017) reviewed the precipitation of Ti(C,N) by the influence of austenite growth. Figure 3 shows the relationship between equilibrium

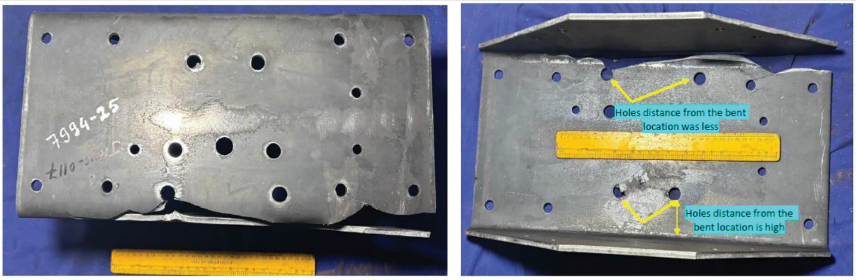

(a) (b)

Figure 1. Failure Sample Indicating Cracks During Forming (a) Front View (b) Rear View.

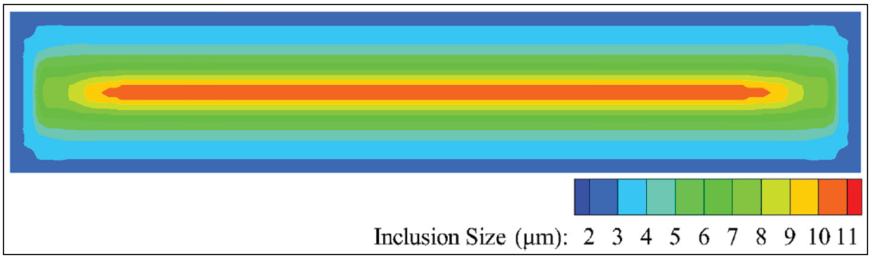

Figure 2. Size Distribution of TiN Inclusions in the Cross-sections.

Source: Que et al. (2023).

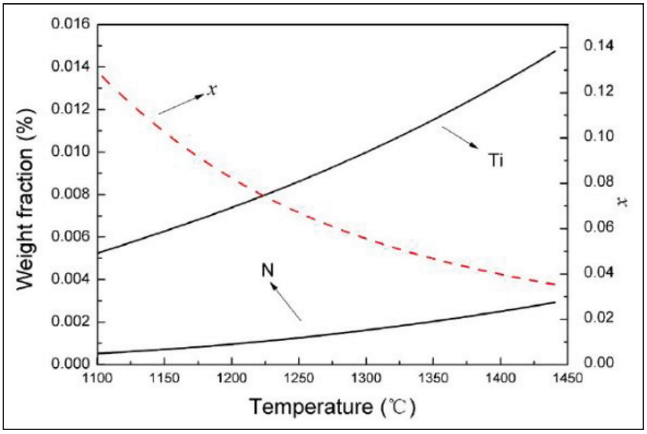

Figure 3. Equilibrium Concentration of Ti and N and Partition Coefficient *x* in Precipitates.

Source: Source: Yang et al. (2017).

concentration, the partition coefficient x of Ti(CxN1-x) precipitates, and temperature. As the temperature decreases, the equilibrium contents of Ti and N in austenite gradually decrease, while x gradually increases. The partition coefficient x is only about 0.04 when the temperature is between 1,350°C and 1,440°C, meaning the Ti(CxN1-x) precipitates at high temperatures are close to pure TiN. TiN possesses a lower equilibrium solubility than TiC; therefore, TiN demonstrates high stability in molten steel, austenite, and ferrite.

Yan et al. (2017) examined how TiN inclusions affect the tendency of low-carbon micro-alloyed steels to fracture under cleavage conditions. The role of TiN inclusions as potential crack initiation sites or pathways for crack propagation, influencing the material's toughness and overall mechanical performance. Nagata et al.'s (2002) paper explores how TiN forms in this slab-cast high-strength low-alloy steel. Specifically, it uses Transmission Electron Microscopy (TEM) to measure the size distribution of TiN particles and analyses how different cooling rates influence their precipitation.

Palai et al. (2013) precisely investigate how the constitutional segregation of alumina (Al_2O_3) in mold slag impacts the steel cleanliness during continuous slab casting. The solid inclusion precipitates from the slag and infiltrates the steel, ultimately compromising its quality and impact on the final product. Won and Thomas (2001) proposed a simple multicomponent steel micro-segregation model by extending the Clyne-Kurz framework. This model predicts phase fraction and solidus temperature and indicates that cooling rate effects on spacing and solute distribution can offset each other, keeping solidus temperature stable.

However, the cleanliness of HS800 grade depends on the operational condition, that is, the steel-making and casting process parameter. The oversize inclusion clearly affects the behavior of the material at a different location. The casting process parameter, that is, secondary cooling, temperature, casting speed, etc., unusual variation can enhance the size of the inclusion. To find the inclusion size of TiN for current practice in the industry at the slab stage, and explore the different secondary cooling strategies at the continuous slab caster to mitigate the oversize inclusion of TiN.

Experimental

To understand the relation between precipitation size and cooling rate in continuous casting, an experimental study has been done. To study the microstructure at the slab stage with respect to variation of secondary cooling rate (Trial 1 & Trial 2) and different locations of slab as depicted in Figure 4b. Figure 4a represents the schematic diagram of a slab. The two planes, plane A and plane B, correspond to standard metallographic orientations used to study solidification structure in a continuously cast slab. Both planes are perpendicular to the casting direction (across the thickness and width of the slab). The purpose of both planes is to understand directional growth of dendrites/columnar grains along heat flow as well as solidification structure through thickness. It helps to identify defects like centerline segregation (CLS), porosity and internal cracks across the section. Different samples were taken from the inner arc (edge region) and center region, as depicted in Figure 4b.

To investigate the material, 150 mm-long sulfur print samples were first taken from the length of the prime slab. After these cooled, smaller 10 cm square sections were cut using a gas torch.

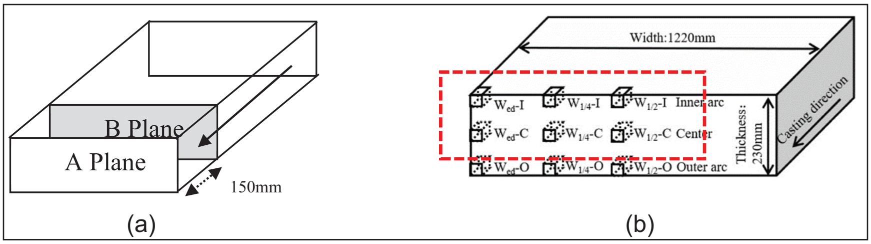

Figure 4. Diagram (a) Schematic Diagram of Slab (b) Schematic Diagram Slab Sample Location.

Table 1. Steel Chemistry of Cracked HS-800 Grade.

Element	C %	Mn %, Max	S %, Max	P %, Max	Al %	Ti %, Max	N (ppm), Max	Mo %
Range	0.05–0.07	1.7	0.005	0.014	0.04–0.06	0.12	70	0.24–0.27

Source: Chemistry ranges at plant.

Sampling was systematic:

- From the inner arc region: Three samples were collected—one from the edge (Wed-I), one from the quarter-width point (W1/4-I), and one from the center-width ($W_{1/2}$-I).
- From the center region: Another three samples were taken following the exact same width-wise pattern.

In total, 12 samples were prepared: 6 originating from the higher secondary cooling zone (Trial 1) and 6 from the lower secondary cooling zone (Trial 2). Following cutting, these samples underwent standard preparation procedures (like grinding and polishing) before their microstructures were analyzed in the metallography laboratory.

Results and Discussions

After sample cutting from the slab at different locations with respect to secondary cooling, the microstructure has been studied. It was found that the inclusion size of TiN is basically a cuboidal shape. Inclusion characterization was performed using energy dispersive spectroscopy (EDS), which confirmed that the observed precipitates are predominantly TiN, as indicated by the presence of strong Ti and N peaks along with minor Fe signals from the surrounding matrix. For statistical reliability, a total of 30 inclusions were measured at each sampling location (e.g., $W_{1/2}$-C) under consistent imaging conditions. The average inclusion size and corresponding standard deviation were calculated using standard statistical methods as depicted in Figure 5. The results show that for Trial 1 (higher cooling rate), the average inclusion size is 4.0 ± 0.68 μm, whereas for Trial 2 (lower cooling rate), it is 4.8 ± 0.81 μm at the $W_{1/4}$-C location. The observed increase in inclusion size with increasing cooling rate is attributed to enhanced precipitation kinetics and limited solute diffusion during rapid solidification. The relatively moderate standard deviation values indicate a reasonably consistent size distribution, although some variation is expected due to local thermal and compositional heterogeneities.

It was also noted that higher cooling rates tend to produce a greater population of these precipitated TiN inclusions. This effect was observed in the comparison between Trial 1 and Trial 2 secondary cooling zones for the TiN inclusions.

As the cooling rate varies at different segments of the caster due to different water flow. Water level flow per unit time for Trial 1 and Trial 2 is depicted in Table 2. Casting speed of this grade is maintained between 0.9 and 1.1 mtr/min. The cooling rate for both Trial 1 and Trial 2 was calculated based on water flow.

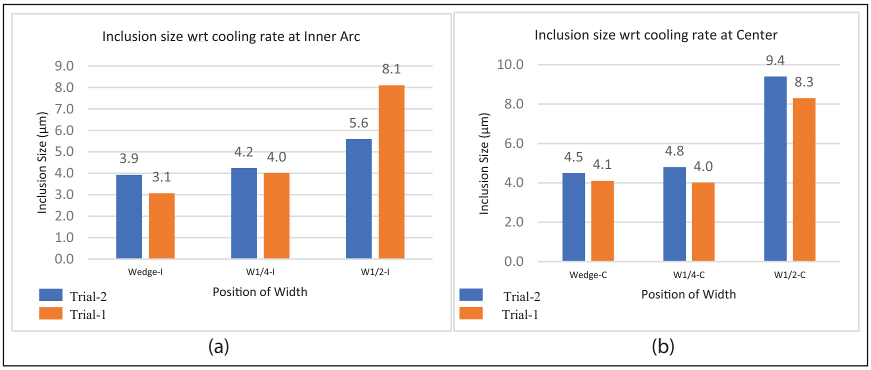

Figure 5. Size of a Precipitated Titanium Nitride (a) Inner Arc Region (b) Center Region.

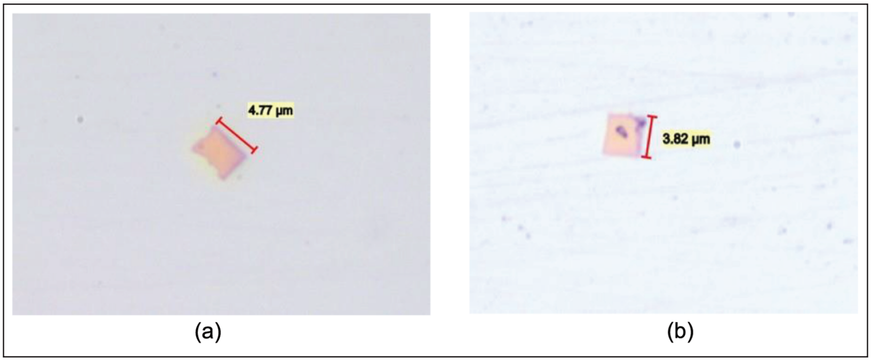

Figure 6. Inclusion Size of Precipitated TiN at the Same Location ($W_{1/2}$-C) in (a) Low Cooling Rate (b) High Cooling Rate.

Figure 5 represents the average inclusion size of precipitate TiN in variation location with varying of different of cooling rates (Trial 1 & Trial 2). In the Figure 5 orange and blue color represents the Trial 1 and Trial 2 respectively. In inner arc region, W_{edge}-I location average inclusion size finer for Trial 1 due to high cooling rate as compared to Trial 2. Whereas at the center location ($W_{1/2}$-I) the average size of precipitate TiN is coarser for Trial 2 due to low cooling rate.

The average inclusion size of precipitated TiN at center of width regions ($W_{1/2}$-C) in higher secondary cooling (Trial 1) and lower secondary cooling (Trial 2) is 8.3 ± 0.81 µm and 9.4 ± 0.89 µm, respectively.

The inclusion size of precipitated TiN in higher secondary cooling is more than in lower secondary cooling at the same location. The inclusion size of precipitated TiN at location ($W_{1/2}$-C) for Trial 2 and Trial 1 is 4.77µm and 3.82 µm, respectively, as depicted in Figure 6. This inclusion size is just for reference to understand the precipitate TiN shape and size.

Table 2. Cooling Profile of Both Trials.

Item	Trial 1 (Liter/Min)	Trial 2 (Liter/Min)
Spray ring nozzle	180–200	160–170
Narrow faces	35–40	30–32
Seg 1	160–190	140–150
Seg 2	100–120	80–100
Seg 3	300–330	220–250
Seg 4–5	180–200	130–150
Seg 6–7	160–190	130–150
Seg 8–9	70–100	50–70
Seg 10–12	140–150	140
Seg 13–16	150	150

Source: Cooling profile at plant.

Conclusion

Based on the systematic investigation involving composition control, continuous casting process parameters, secondary cooling effect, microstructural characterization, and reduction of the cracking effect of the typical AHSS steel strengthened with nano TiN precipitate, the main conclusions are summarized as follows. An experimental study on continuous slab casting of high manganese high-strength steel investigated, and the coarse precipitation of TiN inclusions was identified to cause cracking in the failed sample. By analyzing samples from various locations on the continuous casting slab, it was observed that increased secondary cooling rates lead to finer, more numerous TiN inclusions and these TiN inclusions were found to be cuboidal in shape. However, the highest average inclusion size has been found to be 9.4 ± 0.89 µm for center region of the slab at $W_{1/2}$-C owing to a slower rate of cooling practice at the slab caster. When nano-precipitates are subjected to high temperatures for longer times at slower cooling rates, they can coarsen and act as brittle phases. For instance, coarse TiN phases (>9 nm) on grain boundaries can trigger cleavage fracture rather than ductile deformation. In this study, a novel improved cooling rate practice has been successfully developed, resulting in cast steel with an excellent combination of strength and toughness. The formability and crack resistance significantly improved, offering a promising material solution for demanding applications in the automotive sector.

Declaration of Conflicting Interests

The authors declared no potential conflicts of interest with respect to the research, authorship, and/or publication of this article.

Funding

The authors received no financial support for the research, authorship, and/or publication of this article.

ORCID iD

Ajay Kumar Pradhan https://orcid.org/0009-0002-3021-1223

References

Nagata, M. T., Speer, J. G., & Matlock, D. K. (2002). Titanium nitride precipitation behavior in thin-slab cast high-strength low-alloy steels. *Metallurgical and Materials Transactions A*, *33*(10), 3099–3110. https://doi.org/10.1007/s11661-002-0294-z

Palai, P., Sahoo, P., Dey, A., Roy, T. K., & Mahashabde, V. (2013). Constitutional segregation of Al_2O_3 in slag and its impact on steel cleanliness during continuous casting. *Metallurgical and Materials Transactions B*, *44*(5), 1185.

Que, G., Song, S., Nyembwe, A., Xue, Z., Qi, J., & Deng, Z. (2023). TiN inclusions distribution in the composite cross section of titanium micro-alloyed steel slab: Thermochemical modeling and automatic statistic analysis. *Journal of Materials Research and Technology*, *26*, 5383–5392. https://doi.org/10.1016/j.jmrt.2023.08.247

Won, Y. M., & Thomas, B. G. (2001). Simple model of micro segregation during solidification of steels. *Metallurgical and Materials Transactions A*, *32*(7), 1755–1767.

Yan, W., Shan, Y., & Yang, K. (2007). Influence of TiN inclusions on the cleavage fracture behaviour of low-carbon micro alloyed steels. *Metallurgical and Materials Transactions A*, *38*(6), 1211–1222.

Yang, L., Li, Y., Xue, Z. L., & Cheng, C. G. (2017). Influence of Ti(C,N) precipitates on austenite growth of micro-alloyed steel during continuous casting. *China Foundry*, *14*(5), 421–428. https://doi.org/10.1007/s41230-017-7098-7

Sustainable Manufacturing and Foundry Practices: Guidelines for Authors

Manuscript submission

- The preferred format for your manuscript is MS Word.
- The journal does not consider a paper that has been published elsewhere or that is under submission to another publisher. Authors must attest to this at the time of submission. It is also author's responsibility to disclose any potential conflict of interests regarding their submitted papers.
- Authors will be provided with a copyright form once the contribution is accepted for publication. The submission will be considered as final only after the filled-in and signed copyright form is received.

Basic formatting of the manuscripts

The journal publishes the following article types:

- Research Articles. The paper length should not exceed 8000 words including tables, references and appendices. Abstract (of up to 250 words) and 3-5 keywords are mandatory for an original research paper.
- Review Articles
- Case Reports
- Interviews

Please refer to the Submission Guidelines on the journal website for details on formatting.

Spelling and numerical usages

- Consistent use of either British or American spelling is advised, but not both at the same time.
- Spell out numbers from one to nine, 10 and above to remain in figures. However, for exact measurements use only figures (e.g. 3 km, 9%). Please use '13th' instead of 'thirteenth century'; use '1960s' instead of 'nineteen sixties'.

Quotations, notes, tables and figures

- British English uses single quotation marks to indicate quotations or dialogue, double quotation marks for quotation inside quotation (nested quotation). American English flips that method and uses double quotation marks to indicate quotations or dialogue, and single quotation marks for nested quotations.
- Notes should be numbered serially and presented at the end of the article. Notes must contain more than a mere reference.
- Tables and figures must be cited in the text, and indicated by number separately (Table 1), not by placement (see Table below). Source details for figures and tables should be mentioned irrespective of whether or not they require permissions.
- All photographs and scanned images should have a resolution of minimum 300 dpi and 1500 pixels, and their format should be TIFF or JPEG. Due permissions should be taken for copyright-protected photographs/images.

References and their text citations

- References and their citations should be given in accordance with APA 7th edition.
- Please ensure that all references mentioned in the reference list are cited in the text and vice versa.

For detailed style guidelines, please visit https://journal.indianfoundry.org/

THE INSTITUTE
OF INDIAN
FOUNDRYMEN

Spectrum Journals | THE INSTITUTE
OF INDIAN
FOUNDRYMEN

Powered by Sage